Single-step Development of Plasmonic Nanosensors using Flame Spray Pyrolysis

Sokratis Soutzios

MASTER'S IN PHYSICS

SUPERVISOR: PROFESSOR YIANNIS DELIGIANNAKIS

UNIVERSITY OF IOANNINA

SCHOOL OF NATURAL SCIENCES

DEPARTMENT OF PHYSICS

July 2023

Ανάπτυξη Πλασμονικών Νανοαισθητήρων ενός βήματος με Χρήση Τεχνολογίας Ψεκασμού Πυρόλυσης Φλόγας

Σωκράτης Σούτζιος

Δ.Μ.Σ Φυσικής με Ειδίκευση στην Πειραματική Φυσική

Επιβλέπων: Καθηγητής Ιωάννης Δεληγιαννάκης

Πανεπιστήμιο Ιωαννίνων

Σχολή Θετικών Επιστημών

Τμήμα Φυσικής

Ιούλιος 2023

Abstract

In the present M.Sc. thesis, a method for fabricating plasmonic heterostructured nano-sensors was developed. Specifically, nanosilver particles (Ag) were combined with other oxides such as Titanium oxide (TiO_2) and Silica (SiO_2). Flame Spray Pyrolysis was used for nanoparticle fabrication and in-situ deposition on glass substrate was a crucial factor for the uniformity, reproducibility and stability of the substrate.

Local surface plasmon resonance (LSPR) in metallic nanostructures gives rise to a multitude of optical and electronic phenomena, including the phenomenon of surface-enhanced Raman scattering (SERS). These two phenomena are intricately connected, as LSPR amplifies the electromagnetic field in the vicinity of the nanostructures, resulting in enhanced Raman signals. This synergy between LSPR and SERS enables ultrasensitive detection and characterization of molecules, opening up avenues for various applications such as biosensing, molecular imaging, and chemical analysis.

By controlling the inteparticle distance between Ag particles with SiO_2 working as an dielectric spacer we manage to fabricate a nanosensor for organic molecules, the optimum percentage of SiO_2 is 10% wt. The enhancement factor of SERS calculated to be $EF_{Max} \sim 10^{11}$, meaning that the ultimate Single Molecule SERS limit was reached.

In our study, we used 4-Mercaptobenzoic Acid as Raman Reporter for most of the calibration, due to the fact that it has high adsorption. Also, Rhodamine 6G was used for further investigation.

Additionally, by different deposition times of the nanoparticles on the substrate it was possible to control the thickness of the film, in our case t_d of 60s seemed to be the most efficient. As an application we measured a pesticide named Thiram in concentrations of nM. In the second part of this thesis the Photo Induced Enhanced Raman was studied and more precisely the $AgTiO_2$ substrate was analyzed.

By illuminating the nanosensor, which contained a photo-activated semiconductor, with a UV light lamp we achieve an additional chemical enhancement to contribute in the SERS effect. The observed enhancement is attributed to the presence of surface oxygen vacancies (V_o), which are generated by pre-irradiation of the substrate. It was concluded PIERS enhancement of sequentially made nanofilms was significantly smaller compared to single nozzle made nanofilms. That phenomenon happened due to lattice distortions in the metal-semiconductor interphase.

Finally, the PIERS effect was used in order to increase the Limit of Detection (LOD) for the 4-MBA from 10^{-6} to 10^{-9} M.

i

Περίληψη

Στο παρόν Μεταπτυχιακό Δίπλωμα Ειδίκευσης, αναπτύχθηκε μια μεθοδολογία παρασκευής ετεροδομημένων πλασμονικών νάνο-αισθητήρων. Συγκεκριμένα, παράχθηκαν σωματίδια νανοάργυρου (Ag) σε συνδυασμό με άλλα οξείδια όπως TiO_2 και SiO_2. Η τεχνική που χρησιμοποιήθηκε για την παρασκευή των σωματιδίων είναι η τεχνολογία Ψεκασμού Πυρόλυσης Φλόγας και η εναπόθεση των νανοσωματιδίων έγινε in-situ πάνω σε ειδικά διαμορφωμένο υπόστρωμα ύαλου, ο παράγοντας αυτός είναι σημαντικός για την ομοιομορφία, επαναληψημότητα και σταθερότητα του νανοφίλμ.

Η συντονισμός τοπικού επιφανειακού πλασμονίου (LSPR) σε μεταλλικές νανοδομές δημιουργεί πληθώρα οπτικών και ηλεκτρονικών φαινομένων, συμπεριλαμβανομένου του φαινομένου της Επιφανειακής Ενίσχυσης Φασματοσκοπίας Raman (SERS). Αυτά τα δύο φαινόμενα είναι στενά συνδεδεμένα, καθώς η LSPR ενισχύει το ηλεκτρομαγνητικό πεδίο στην περιοχή των νανοδομών, με αποτέλεσμα την ενισχυμένη ανασπονδόσκοπηση Raman. Αυτή η συνεργία μεταξύ LSPR και SERS δίνει τη δυνατότητα για ανίχνευση και χαρακτηρισμό μορίων, ανοίγοντας τον δρόμο για διάφορες εφαρμογές, όπως βιοαισθητήρες, μοριακή απεικόνιση και χημική ανάλυση.

Με τον έλεγχο της απόστασης μεταξύ των σωματιδίων αργύρου μέσω της χρήση του SiO_2 ως διηλεκτρικό απομονωτή, καταφέραμε να κατασκευάσουμε ένα νανοαισθητήρα για οργανικά μόρια, με το βέλτιστο ποσοστό του SiO2 να είναι 10%. Ο παράγοντας ενίσχυσης της SERS υπολογίστηκε $EF_{Max} \approx 10^{11}$, γεγονός που σημαίνει ότι βρισκόμαστε στο όριο ανίχνευσης για Single Molecule SERS.

Στη μελέτη μας, χρησιμοποιήσαμε το 4-Mercaptobenzoic Acid ως μόριο ανίχνευσης για την βαθμονόμηση, λόγω του υψηλού βαθμού προσρόφησης του. Επιπλέον, με την αλλαγή του χρόνου εναπόθεσης των νανοσωματιδίων στο υπόστρωμα ύαλου, ήταν δυνατό να ελέγξουμε το πάχος του φιλμ, με το πάχος που αντιστοιχεί σε χρόνο $t_d = 60s$ να φαίνεται ως το πιο αποδοτικό. Ως εφαρμογή, μετρήσαμε έναν παρασιτοκτόνο με την ονομασία Thiram σε συγκεντρώσεις έως nM.

Στο δεύτερο μέρος αυτής της διατριβής μελετήθηκε *Φωτοεπαγόμενη Ενίσχυση Φασματοσκοπίας Raman (PIERS)* και ειδικότερα αναλύθηκε το υπόστρωμα $AgTiO_2$. Με φωτισμό του νανοαισθητήρα, ο οποίος περιείχε ως φώτο-ενεργοποιούμενο ημιαγωγό το διοξείδιο του τιτανίου, με υπέρυθρο φως επιτυγχάνουμε μια επιπλέον χημική ενίσχυση που συντελεί στο φαινόμενο SERS. Η παρατηρούμενη ενίσχυση αποδίδεται στην παρουσία επιφανειακών ατελειών οξυγόνου (VO_2), οι οποίες δημιουργούνται με τον φωτισμό του φιλμ. Η ενίσχυση PIERS των νανοφίλμ που είχαν παρασκευαστεί με διαδοχική εναπόθεση σωματιδίων ήταν σημαντικά μικρότερη σε σύγκριση με τα φιλμς που είχαν ταυτόχρονη εναπόθεση αργύρου και διοξειδίου του τιτανίου. Αυτό το φαινόμενο δημιουργείται εξαιτίας παραμορφώσεων του πλέγματος στην διεπιφάνεια μέταλλό-ημιαγωγός.

Τέλος, το φαινόμενο PIERS χρησιμοποιήθηκε με σκοπό να βελτιώσει το όριο ανίχνευσης στο 4-MBA από 10^{-6} M σε 10^{-9} M .

Acknowledgments

 I would like to take this opportunity to express my deepest gratitude and appreciation to all those who have supported me throughout my journey in completing this master thesis.

First and foremost, I am immensely thankful to my supervisor, Yiannis Deligiannakis. His expertise, patience, and constant support have been instrumental in shaping this research project. His insightful feedback, constructive criticism, and dedication to my academic development have significantly contributed to the success of this thesis. I am truly grateful for his mentorship and the valuable lessons I have learned under his guidance.

I would also like to extend my heartfelt appreciation to Dr. Constantinos Moularas , whose assistance and collaboration have been indispensable during the course of this research. His invaluable insights, technical expertise, and willingness to share his knowledge have greatly enriched my understanding of the subject matter. I am deeply grateful for his unwavering support, encouragement and the countless hours he has devoted to helping me overcome challenges.

Furthermore, I would like to express my sincere gratitude to the other members of the lab who have provided a stimulating academic environment and fostered an atmosphere of collaboration. Their valuable discussions, feedback, and camaraderie have played a crucial role in shaping my research journey. I am thankful for their encouragement, patience, and the knowledge exchange that has greatly contributed to my personal and professional growth.

In the final paragraph, I would like to acknowledge the unwavering support of my family and loved ones. I am deeply grateful to my girlfriend for her unwavering love and support. To my sisters, thank you for your constant encouragement and belief in my abilities. Lastly, I am eternally thankful to my parents for their unconditional love, sacrifices, and unwavering support throughout my academic journey. Your unwavering support and encouragement have given me the strength to overcome challenges and strive for excellence.

Contents

Chapter 1

Introduction

1.1   Nanoplasmonics

Nanomaterials have revolutionized various fields of science and technology by exploiting unique properties at the nanoscale [1]. One fascinating area of study is nano plasmonic, which explores the behavior of plasmons- collective oscillations of electrons- in nanoscale metallic structures. These structures can manipulate and control light at the nanoscale, enabling a myriad of applications [2]. Nano plasmonics finds its utility in enhancing light-matter interactions, enabling ultra-sensitive biosensing, advancing data storage and communication technologies, and even revolutionizing solar energy harvesting[2]. By harnessing the precise control over light at the nanoscale, nano plasmonics offers an exciting avenue for designing novel devices with unprecedented functionality and performance[3]. The interdisciplinary nature of this field brings together physics, materials science, chemistry, and engineering to push the boundaries of our understanding and technological capabilities at the nanoscale[4].

1.1.1 Local Surface Plasmonic Resonance (LSPR)

Metallic nanostructures possess remarkable optical properties derived from their nanoscale characteristics. Throughout history, silver (Ag) and gold (Au) colloids have been widely utilized for their captivating color hues[5], exemplified in stained glass and the renowned Lycurgus cup, as illustrated in Figure 1.1.

The observed color shift depends on the incident light type: when light passes through the glass, it exhibits a red hue, while surface scattering renders it an opaque green appearance. This behavior in metals arises from the collective oscillation of free electrons stimulated by incident electromagnetic waves[4]. In the electrodynamic perspective, external electric fields induce Coulomb forces, while positive ions in the metallic lattice generate restoring forces that drive the oscillation of electrons.

1.1.1 Local Surface Plasmonic Resonance (LSPR)

Figure 1.1 Lycurgus cup displaying differences in the transmitted (green) and reflected (red) light.

The observed phenomenon is attributed to surface plasmon resonance (SPR)[6,7]. In this context, the oscillating electric field of light can resonantly stimulate the free electrons within the metal through the generation of interfacial charges. This coherent exchange of energy between the electrons and the electromagnetic field occurs during SPR. When metallic nanoparticles are engineered to possess dimensions smaller than the wavelength of the incident electromagnetic wave, resulting in the confinement of surface plasmons at the nanoscale, the excitation is referred to as localized surface plasmon resonance (LSPR)[8] and is demonstrated in Figure 1.2. To provide a comprehensive understanding of the extraordinary optical properties displayed by metallic nanoparticles through localized surface plasmon resonance (LSPR), it is necessary to delve into the fundamental physics underlying each LSPR-induced phenomenon. Additionally when we are referring to a Plasmonic NanoParticle we are
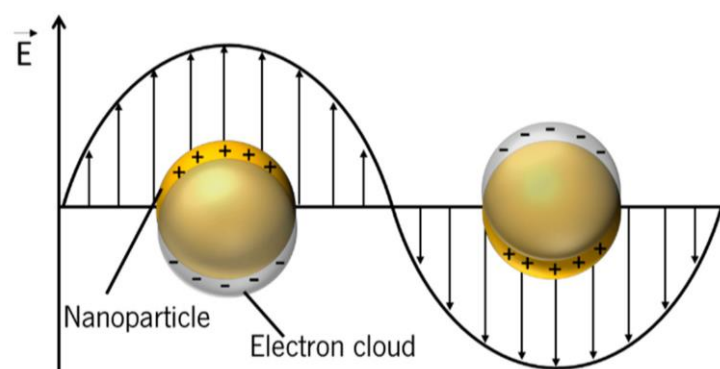

Figure 1.2 Schematic illustration of LSPR for a plasmonic nanosphere. LSPR represents localized surface plasmon resonance.

referring to a particle that is size is smaller than the mean free path of the material

2

Among various theories, Mie theory [9] has emerged as the most successful approach for describing the photoexcitation and response of plasmons in a single metallic nanosphere. Mie theory enables a detailed analysis of how light interacts with the metallic nanoparticle, taking into account factors such as size, shape, and composition,
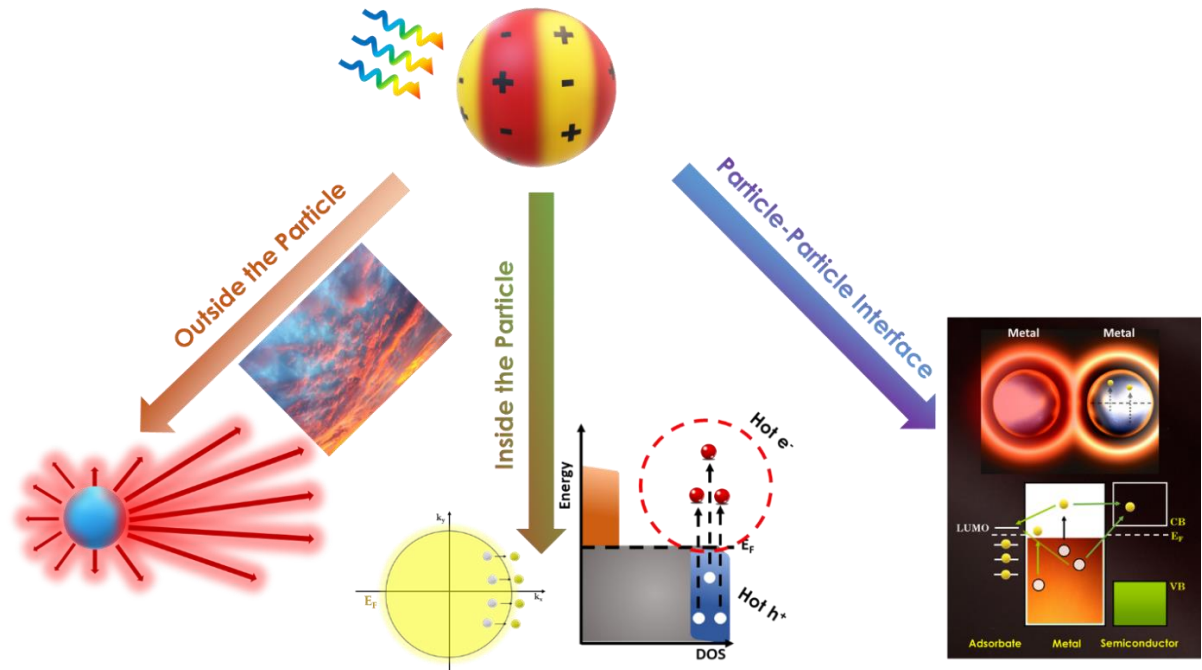

Figure 1.3 A diagram illustrating the ways in which plasmons drive various processes, depending on their scale. The energy produced by LSPR (Localized Surface Plasmon Resonance) is reduced through two different mechanisms: radiative effects that occur outside the particle and non-radiative effects that take place inside the particle. Additionally, on the interface between particles, other phenomena.

and provides valuable insights into the optical behavior observed in LSPR phenomena. In the next theoretical approach, the different plasmon driven phenomena will be examined in three different scales: **outside the particle**, **inside the particle** and in the **interface between particles** (a schematic representation is displayed in Figure 1.3)

1.1.2 Phenomena Outside the Particle

Metals play a crucial role in the field of plasmonics because of the abundance of "free" electrons in their valence bands. The way they interact with incoming electromagnetic waves can be explained using the dielectric function. In the case of bulk metals, the Drude model approximates the optical response by considering the effect of an external electromagnetic stimulus on a single free electron and then scaling it up by the total number of electrons present. By applying the Drude's model and basic physics laws the dielectric function can be written as[10]:

$$\varepsilon(\omega) = \varepsilon(re) + i\varepsilon(im) = 1 - \frac{\omega_p^2}{\omega^2 + i\gamma_0\omega} \qquad (1.1)$$

where $\omega_p^2 = ne^2/\varepsilon_0 m_e$ is the plasma frequency of the electrons inside the metal structure, n is the free electron density, e is the electron charge, ε_0 is the vacuum permittivity, me is the electron effective mass and γ_0 is the damping constant.

The imaginary part of the damping term in the dielectric function (Equation 1.2) is responsible for interband transitions and scattering losses .These losses primarily occur due to crystal impurities and relaxation events.

To determine the plasmonic response, it is necessary to analyze the phenomena of light scattering when the dielectric constants of a specific particle and its surrounding environment are known. First the Gustav Mie successfully solved the Maxwell equations, considering the appropriate boundary conditions, for a single and uniform dielectric sphere. This achievement, known as Mie theory, enables the calculation of scattering and absorption cross-sections that depend on the size of the sphere. Mie theory finds applications in various fields due to its ability to provide valuable insights into these phenomena. Analytical representation of Mie equations is out this thesis scope but the extinction, scattering and absorption cross sections have the following form:

$$\sigma_{ext} = \frac{2\pi}{k^2} \sum_{n=1}^{\infty} (2n+1)\Re e(a_n + b_n) \qquad (1.2)$$

$$\sigma_{sca} = \frac{2\pi}{k^2} \sum_{n=1}^{\infty} (2n+1)(|a_n|^2 + |b_n|^2) \qquad (1.3)$$

$$\sigma_{abs} = \sigma_{ext} - \sigma_{sca} \qquad (1.4)$$

the a_n and b_n are the scattering coefficients.

When the size of particles is significantly smaller than the wavelength of the incoming light, it is assumed that the electric field remains constant and the effects of retardation are disregarded. In such cases, the particle is considered as an electric

dipole, and its ability to become polarized (polarizability) is proportional to the diameter (d) of the particle. Within the dipole approximation, the absorption cross-section (σ_{abs}) and extinction cross-section (σ_{ext}) are both proportional to the intensity of
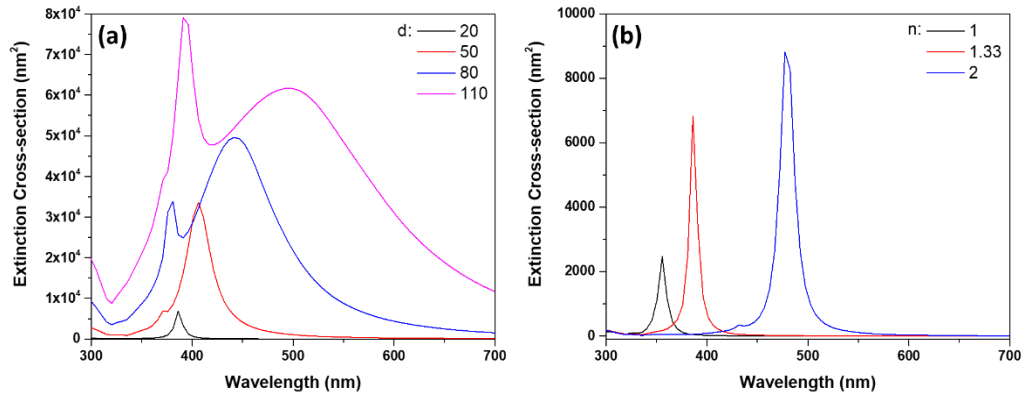

Figure 1.4 (a) The extinction cross sections of silver particles change as their diameter varies.(b) The extinction cross sections of silver particles change depending on the refractive index of the surrounding medium.

the incident light (I) and a function (a) that depends on the frequency (ω) of the light. In this approximation, scattering events are insignificant due to the small size of the particle.

Due to variations in the phase of the electric field across the volume of a particle, the distribution of charges on the particle's surface becomes non-uniform, necessitating the consideration of retardation effects. In addition to the resonance red-shift[11], Figure 1.4 demonstrates that increasing the size of the particle leads to the emergence of additional plasmon bands due to the occurrence of higher-order multipolar modes, specifically the dipolar and quadrupolar modes[12].
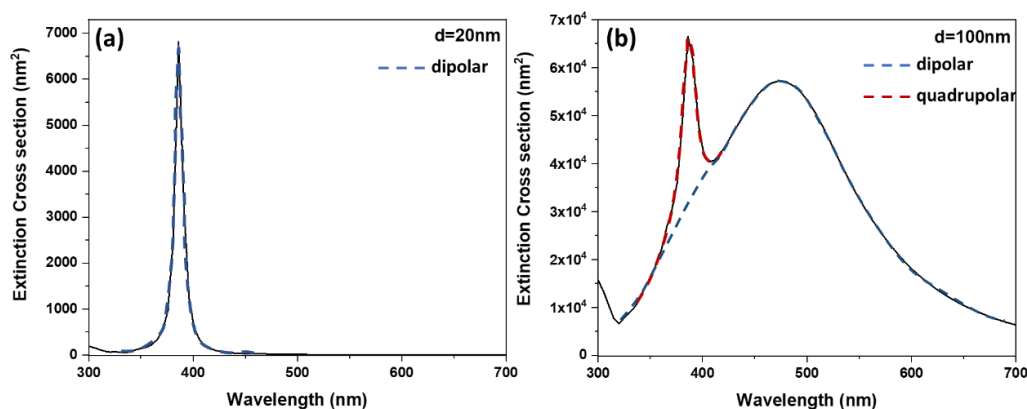

Figure 1.5 (a) The extinction cross section of a single silver nanoparticle with a diameter of 20 nm. b) The extinction cross section of a single silver nanoparticle with a diameter of 100 nm. The spectrum is deconvoluted to distinguish between dipolar and quadrupolar modes.

5

The electric field's phase variations across a particle's volume result in non-uniform charge distribution on the particle's surface, requiring consideration of retardation effects. Increasing the particle size leads to additional plasmon bands, specifically dipolar and quadrupolar modes[13], as presented in Figure 1.5. For small particles, the dominant term is the dipole term, which represents the directional component of the electric field. As the particle size approaches the wavelength of light, the quadrupole term becomes more significant, representing the intensity variation with direction. The dominance of each term depends on the particle's size, shape, and polarizability.

1.1.3 Phenomena Inside the Particle

The presence of Localized Surface Plasmon Resonance (LSPR) in metal nanostructures gives rise to a range of optical and electronic phenomena. These processes occur during the excitation and subsequent damping of the plasmon energy stored within the oscillating electron cloud. Plasmonic effects can be categorized into radiative and non-radiative effects[14].

In the case of radiative effects, LSPR relaxes and re-emits light into the far-field. Metal nanostructures can also act as secondary light sources or antennas, concentrating light on their surfaces and enhancing local electric fields in close proximity.

Figure 1.6 A diagram illustrating the permissible electronic transitions in silver (Ag).

In the case of non-radiative effects, plasmon dephasing leads to the absorption of photons, depositing electronic energy and generating highly energetic electrons with energy above the Fermi level. These energetic electrons are referred to as "hot" electrons[15,16]. The most important pathways of these hot carriers and the routes of plasmon-energy dissipation will be discussed in subsequent sections.

Firstly, Figure 1.6 illustrates carrier dynamics and plasmon decay pathways when an external electric field interacts with a plasmonic nanoparticle (PNP), which follows a Fermi-Dirac distribution. To understand the plasmon-driven mechanisms and multi-step non-radiative LSPR decay, a detailed explanation of the plasmon energy transfer
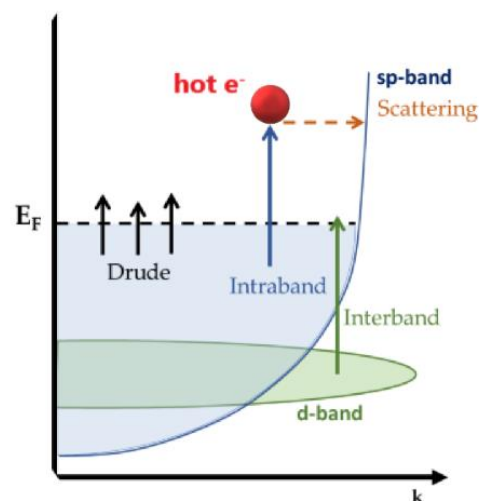
is essential. In the classical picture, charge displacement results in coherent electron cloud oscillation, following the Drude model. However, in the quantum mechanical perspective, the quantization of the electric field must also be considered. In this scenario, PNPs are illuminated by discrete photons with energy $\hbar\omega$. Photon absorption in this light-matter interaction is impossible without additional momentum through inelastic scattering (e.g., with a defect or a phonon) or occurring in a confined system with boundaries (back-scattering events)[17,18].
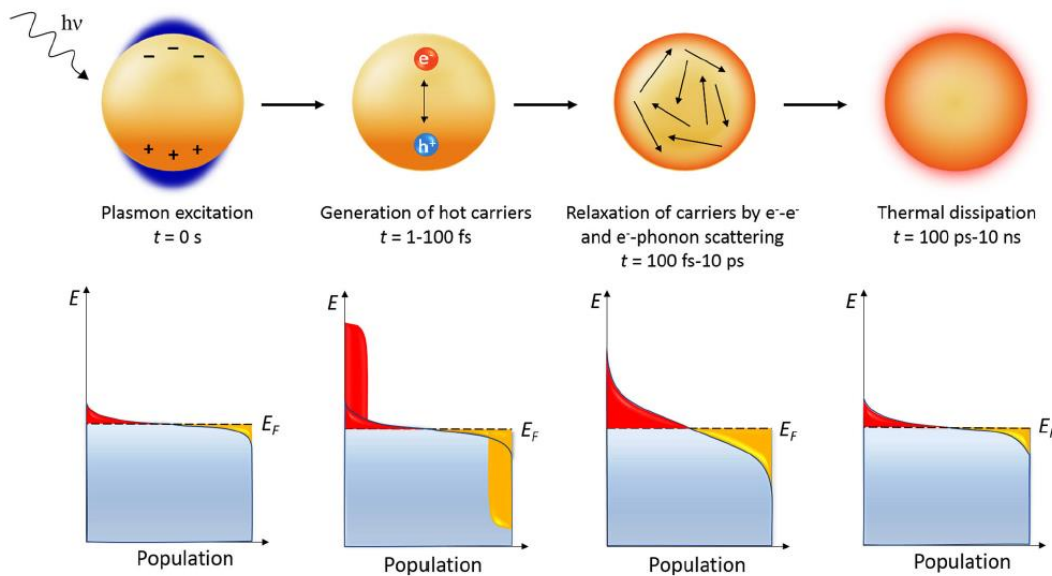

Figure 1.7 Sequence of events during hot carrier relaxation. (From left to right): Light photons are absorbed, transferring energy to the electronic distribution and creating electron-hole pairs above the Fermi level. The hot carriers then undergo relaxation and equilibrate their temperature with the lattice vibrations within a few picoseconds. The relaxation of the heated lattice occurs through interactions between phonons, where the energy stored in the vibrational modes is dissipated from the nanoparticle to the surrounding medium as heat, resulting in an increase in temperature.

Quantum confinement in small particles affects charge carrier dynamics in metals. As particle size decreases, quantum effects at the surfaces become more significant, leading to plasmon dephasing. This is observed through broadening of the plasmonic peak and an increased plasmon decay rate, inversely scaling with particle size. Classically, surface-induced damping occurs due to electron collisions with the particle boundaries. In the quantum realm, the boundary discretizes electronic states, enabling surface-assisted plasmon decay or Landau damping[19,20]. This anelastic scattering allows the excitation of nonthermal hot electrons within a specific energy range. Modifying the size and shape of metallic particles controls the generation of hot carriers[21]. The presence of intense electric fields in proximity to the particle's boundary, known as hot

spots, further enhances the population of nonthermal carriers[22,23]. The excitation of hot carriers in metallic nanoparticles is influenced by the lossy nature of the LSPR process and its non-radiative decay mechanisms. If the plasmon energy is not transferred through any of the mentioned pathways, subsequent relaxation processes will decrease the plasmon resonance until the energy is released as heat (Figure 1.7).

1.1.4 Phenomena in the Interparticle Interface

As mentioned previously, when metallic nanoparticles are stimulated by an incident electromagnetic wave, their conduction electrons collectively form a coherent electronic cloud. This charge displacement induced by Coulomb forces leads to the polarization of the particle, resulting in the accumulation of charges at opposite ends of its structure. This oscillating behavior reaches its maximum at resonance, leading to a near-field amplification near the charged region, specifically the particle's surface. The ability of plasmonic nanoparticles (PNPs) to effectively concentrate light is crucial for generating these localized high electric fields in close proximity to the particle[24].
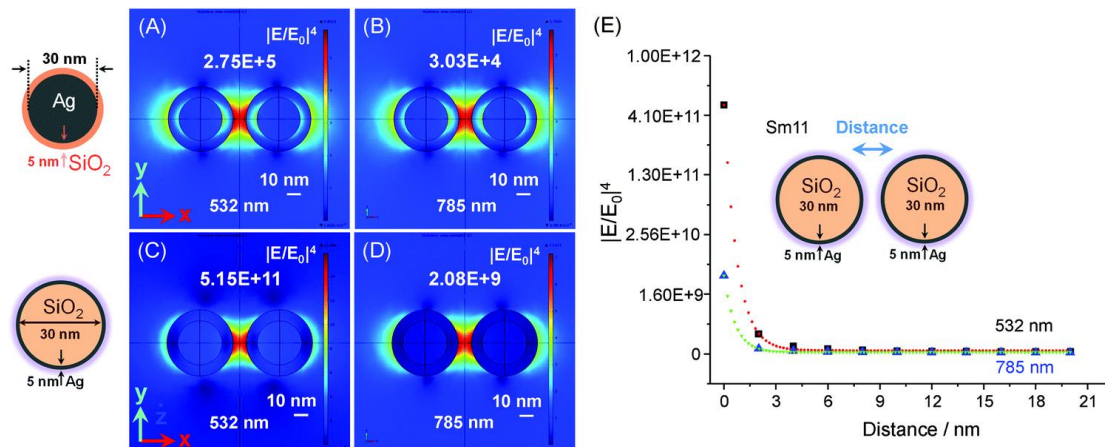
Figure 1.8 A-D) The distribution of the electromagnetic field is shown for two types of plasmonic nanoparticles with a spherical shape: (i) silica-core (30 nm) with a thin silver layer (5 nm) and (ii) silver-core (30 nm) with a thin silica layer (5 nm). The field distribution is depicted for two excitation wavelengths, 532 nm and 785 nm. The incident electromagnetic plane wave is aligned along the z-axis with polarization along the y-axis, while the x-axis is perpendicular to the zy-plane. E) The calculated distribution of the Surface-Enhanced Raman Scattering (SERS) enhancement factor (EF) is presented for the wavelength range from 400 nm to 1100 nm.

The near-field enhancement, which is a direct consequence of Localized Surface Plasmon Resonance (LSPR), is highly dependent on the morphology of the nanoparticles and their plasmonic coupling. Complex-shaped nanoparticles, such as

nanostars, exhibit significantly enhanced local fields around their sharp features. This enhancement is attributed to the increased surface charge density resulting from the curvature of these features. The nanogaps between coupled particles, known as "hot spots," also play a crucial role in generating substantial increases in near-field enhancement[25]. Plasmonics has emerged as a distinct field of study, focusing on the design and modification of nanoparticle shapes to achieve targeted field augmentation at specific locations, employing the principle of plasmon hybridization.

In the realm of plasmonic nanoensembles, the initial experimental evidence of enhanced fields was observed when Raman scattering was greatly amplified in the presence of a metallic substrate. This phenomenon was later attributed to LSPR, giving rise to Surface-Enhanced Raman Scattering (SERS)[26,27]. For spherical particles, an analytical solution exists for determining the magnitude of the electric field outside the particle, as described by the following equation.

$$E_{out}(x, y, z) = E_0 \hat{z} - \alpha E_0 [\frac{\hat{z}}{r^3} - \frac{3z}{r^5}(x\hat{x} + y\hat{y} + z\hat{z})] \qquad (1.5)$$

Where a is the polarizability. In the context of Raman scattering, the incident field causes a molecule on the surface to undergo an oscillating dipole moment. During the process of radiating this dipole, there is a likelihood of a vibrational transition taking place, leading to the emission of light at a different frequency. The absorption of the initial photon is directly related to the intensity of the electric field in the vicinity. LSPR-induced enhanced local fields can greatly amplify this process. Subsequently, the SERS enhancement is relative to the initial intensity of the incident wave. The SERS phenomena will be thoroughly analyzed in upcoming section.

Finally, another phenomena in the plasmonic interphase is thermoplasmonics. Before the early 2000s, photothermal effects were considered unwanted side effects in the field of plasmonics. However, the groundbreaking research conducted by the Halas group on photothermal cancer therapy demonstrated the beneficial role of thermal effects as a plasmon-induced mechanism[28,29]. When electrons are excited on resonance, the unscattered portion of plasmon energy is dissipated through Landau damping, leading to a significant temperature increase in the vicinity of the particles. This phenomenon enables precise control of heat at the nanoscale. Despite being in resonance, metals are not ideal optical conductors, and their lossy nature results in resistive heat generation

through photon-electron interactions, which is then dissipated through lattice oscillations via electron-phonon interactions. This discovery paved the way for the sub-field of Thermoplasmonics, with Guillaume Baffou[30] making significant contributions to understanding its fundamental physics.

1.2   Surface Enhanced Raman Spectroscopy (SERS)

Raman spectroscopy is known for its ability to detect small amounts of solid material, making it sensitive in certain cases. However, its sensitivity is limited in applications involving analysis in solution. Therefore, a Raman technique that can significantly enhance sensitivity would be highly valuable. Surface-enhanced Raman scattering (SERS) offers a remarkable improvement in scattering efficiency[31], with an enhancement of up to about 10^{15} compared to normal Raman scattering. Despite its potential, SERS has faced challenges due to its complexity and the difficulties in understanding its underlying theory[32].

Other techniques, such as resonance Raman scattering, provide improved sensitivity but come with their own limitations. Resonance Raman scattering is effective only for specific colored molecules, and issues like fluorescence interference and sample degradation further restrict its utility. In contrast, SERS exhibits effectiveness with a broader range of molecules and offers a more substantial enhancement in sensitivity. These characteristics make SERS a promising technique to consider for specific targets.

In 1974, Fleischman et al. made the initial observation of surface-enhanced Raman scattering (SERS)[33]. Their study involved pyridine molecules adsorbed onto a silver electrode that had been roughened through oxidation-reduction cycles. The researchers initially attributed the strong Raman scattering to the significant increase in the surface area of the electrode caused by the roughening process, which allowed for more pyridine molecules to be absorbed.

However, subsequent studies by Jeanmarie and Van Duyne[8], as well as Albrecht and Creighton[34], challenged this explanation. They demonstrated that the observed intensity enhancement in SERS was not solely attributable to the increase in surface area. According to their findings, the expected increase in intensity from surface roughening would have been less than a factor of 10. However, the actual enhancement achieved in SERS experiments was on the order of 10^6, indicating that there were additional factors at play beyond the surface area increase.

In conventional Raman spectroscopy, the overall intensity of Raman signals from a molecule is directly related to the power density of the laser and the Raman cross-section of the molecule. This principle can also be extended to surface-enhanced Raman scattering (SERS). Essentially, the intensity of SERS signals for a specific vibrational mode of an analyte is expected to be proportional to the laser intensity and the normal Raman cross-section but influenced by an enhancement factor.

An important consideration in SERS is the concept of "real" enhancement factors. These factors represent the actual enhancement achieved in comparison to what would be observed under non-SERS conditions for the same molecule. It ensures that the enhancement is accurately characterized and measured in relation to the baseline intensity without SERS effects.

As for the enhancement factor, SERS involves a dual mechanism[35], encompassing both electromagnetic (EM) and chemical contributions, which contribute to the enhancement of Raman scattering. In conventional SERS, the electromagnetic component primarily drives the enhancement, while the chemical contribution has a relatively lesser impact[36].

1.2.1 Electromagnetic Factor

The primary factor contributing to the enhancement in surface-enhanced Raman scattering (SERS) is believed to be the electromagnetic enhancement, as presented in **Figure 1.9**. This mechanism relies on enhancing the EM field through resonance excitations of localized conduction-electron oscillations at the surface of metallic nanostructures, known as surface plasmons (SPs)[37]. This resonance, referred to as dipolar localized surface plasmon resonance (LSPR)[38], can be determined from the extinction spectrum, which involves the absorption and elastic scattering of the metallic nanostructure, known as surface plasmon extinction (SPE). The resonance frequency ω_{MAX} of plasmons in the metallic nanostructure depends on various factors, including the dielectric functions[39] of the metal ($\varepsilon_{metal}(\omega)$) and the surrounding medium ($\varepsilon_M(\omega)$). The EM field in the immediate vicinity of the roughened metal surface is significantly intensified due to the coupling between the photon and LSPs. Consequently, molecules adsorbed on the surface experience a much stronger local electric field (E_{local}). Additionally, the molecule's dipole radiation occurs in close proximity to the metal,

rather than in free space. The Stokes Raman scattering (RS) radiation, shifted in frequency at $\omega_S = \omega_{inc} - \omega_{Vib}$ (corresponding to a specific vibrational mode), can itself excite the LSPR of the metallic nanostructure. Both local field enhancement and Raman radiation enhancement stem from the coupling of the EM field with the LSPR of the metallic substrate. While the coupling may not be identical, the resonances should
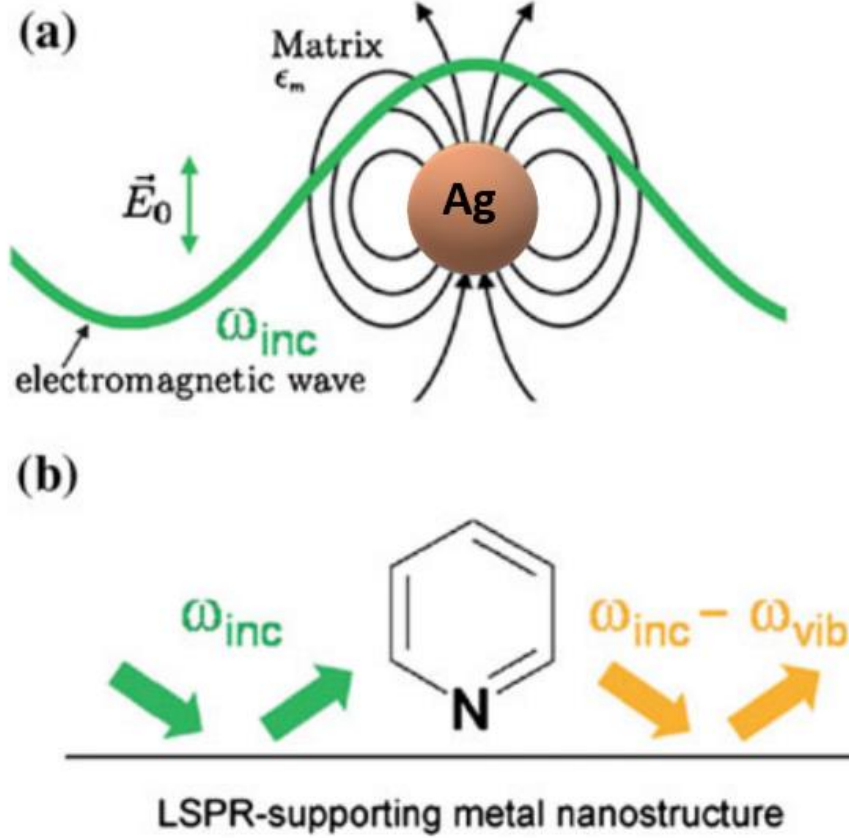

Figure 1.9: EM enhancement in SERS a) A silver NP acts as a nanoantenna by excitation of a dipolar localized surface plasmon resonance (LSPR) b) Both the "incoming" field (ω_{inc}) and the "outgoing" field ($\omega_{inc} - \omega_{vib}$) are enhanced by elastic light scattering off the LSPR-supporting metallic nanostructure.

exhibit at least qualitative similarity for both enhancement mechanisms.

The overall SERS intensity depends on both the "incoming" ω_{Inc} and the "outgoing" $\omega_S = \omega_{inc} - \omega_{Vib}$ field[40]:

$$I_{SERS} = I_{inc}(\omega_{inc}) - I(\omega_S) = |E_{inc}(\omega_{inc})|^2 - |E_S(\omega_S)|^2 \tag{1.6}$$

To achieve optimal Surface-Enhanced Raman Spectroscopy (SERS) enhancement, it is essential for both the incident radiation at ω_{inc} and the Stokes Raman shifted radiation at $\omega_S = \omega_{inc} - \omega_{Vib}$ to be in resonance with the localized surface plasmon resonance (LSPR) peak of the metallic nanostructure. Typically, nanostructures with dimensions around 30-100 nm are required to fulfill the conditions for LSPR resonance with visible light. The LSPR effect strongly relies on the size and shape of the nanostructures and can be significantly influenced by closely spaced nanostructures due to the presence of coupling, primarily arising from interactions between individual nanostructures.

In simpler cases, the intensity of SERS can be reduced to the $|E(\omega_{inc})|^4$ factor. A moderate increase in the ratio of the local electric field (E_{loc}) / (E_{inc}) results in substantial enhancements of Raman scattering, leading to the Surface-Enhanced Raman Spectroscopy enhancement factor (EF).

The electromagnetic (EM) enhancement is also influenced by the properties of the metal and the distance between the molecule and the metal surface. The electromagnetic $EF_{em}(\omega_s)$ can be described in case of a small metallic sphere ($r < \lambda/20$) as:

$$EF_{em}(\omega_S) \cong \left| \frac{\varepsilon(\omega_{inc}) - \varepsilon_0}{\varepsilon(\omega_{inc}) + 2\varepsilon_0} \right|^2 \left| \frac{\varepsilon(\omega_S) - \varepsilon_0}{\varepsilon(\omega_S) + 2\varepsilon_0} \right|^2 \left(\frac{r}{r+d} \right)^{12} \qquad (1.7)$$

where $\varepsilon(\omega)$ is the complex frequency-dependent dielectric function of the metal, ε_0 is the dielectric constant of the bulk medium and d is the distance of the molecule from the surface. It is important to note that the molecule being analyzed does not need to be in direct contact with the metal surface. The intensity of SERS depends on the distance (d) between the molecule and the surface, following a proportional decrease of approximately $1/d^{12}$. It has been demonstrated that the Raman enhancing effect is detectable for distances up to 5-10 nm[32].

1.2.2 Chemical Factor

Numerous research studies have demonstrated the significant role of plasmon resonances in the observed enhancement of Raman signals. However, relying solely on the well-accepted plasmon theory does not provide a complete explanation for the

diverse range of molecules and substrates observed in SERS. It has been observed that molecules capable of being chemically adsorbed onto metal surfaces exhibit the largest enhancements, even among molecules with similar Raman cross-sections. The charge transfer (CT) mechanism[41,42] is proposed to explain these phenomena.

According to the CT theory, the conduction band orbitals of the metal lie between the highest occupied molecular orbital (HOMO) and the lowest unoccupied molecular orbital (LUMO) of the adsorbed molecule[43]. CT can occur in two ways: from a metal cluster to molecules or from molecules to a metal cluster, depending on the relative energies of the metal Fermi level and the HOMO/LUMO levels of the adsorbed molecule. In the case of semiconductors, which have an energy gap between a fully occupied valence band and an empty conduction band, the CT between semiconductor nanomaterials and molecules depends on factors such as vibronic coupling, conduction band properties, and the excited state and ground state of the molecule[44].

Briefly, the CT in a semiconductor-molecule[45,46] system can occur through the following five pathways[43], as shown in **Figure 1.10:**

a) Molecule HOMO-to-CB: The incident light directly excites the electron occupying the ground state of the molecule from the HOMO to an energy level in the conduction band of the semiconductor. The excited electron quickly returns to a specific ground vibrational energy level of the molecule, and a Raman photon is subsequently emitted.

b) CT complex-to-CB: The chemical bonding between the molecule and semiconductor reduces the formation of a charge-transfer complex, leading to an enhancement in the polarizability and resulting Raman signals of the original adsorbed molecules.

c) VB-to-molecule LUMO: The electron present in the valence band of the semiconductor is excited to the higher energy level LUMO in the molecule. It then rapidly transitions back to the valence band, resulting in the emission of a Raman photon.
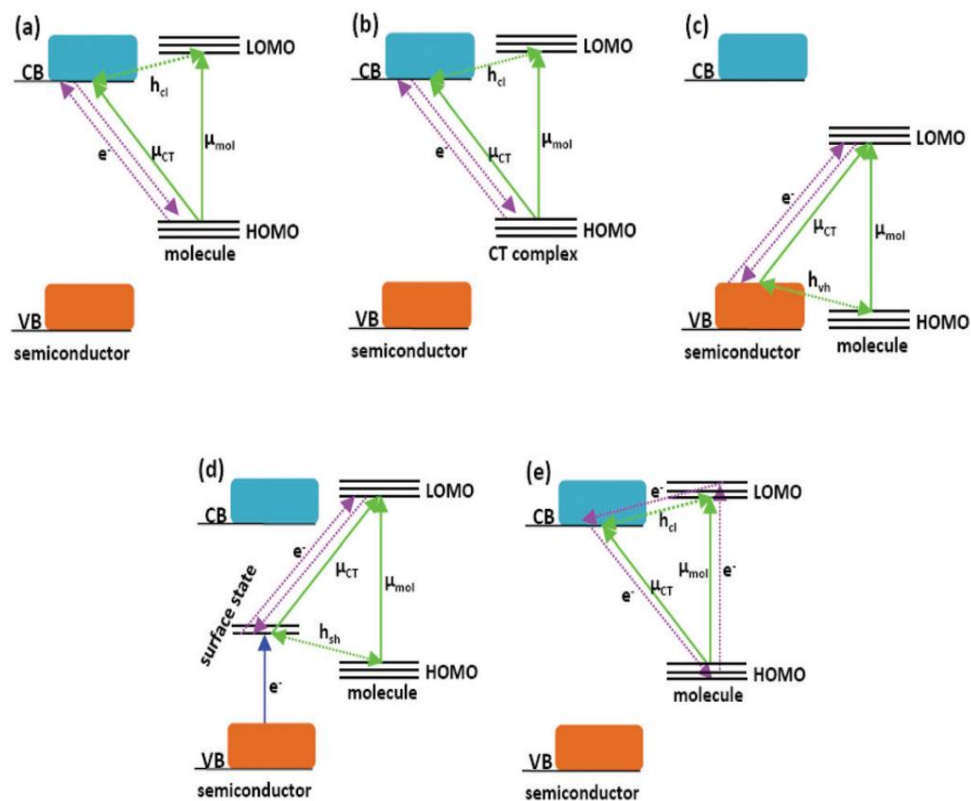
Figure 1.10: *Charge transfer ways in a semiconductor-molecule system.*

d)   Surface state-to-molecule LUMO: The electron is initially excited from the valence band of the semiconductor to the surface defect, leading to the formation of a surface state. Subsequently, the electron undergoes further excitation from the surface state to the LUMO of the molecule. Upon returning to the surface state, a Raman photon is released.

e)   CB-to-molecule HOMO: Certain dye molecules can be easily excited by visible light to a higher energy level LUMO. The electron is then injected into a matching energy level in the conduction band of the semiconductor through resonant tunneling. Finally, the electron transitions back to a ground vibrational energy level of the molecule, resulting in the emission of a Raman photon.

1.2.3 Selection Rules

Interpreting SERS spectra is not a straightforward task[26,47]. New peaks may emerge in SERS that are not present in normal Raman scattering, while some peaks that are strong in normal Raman scattering can become weak or completely disappear in SERS. Furthermore, the intensity changes observed at different concentrations can be nonlinear[48]. A notable example of this is observed with pyridine. At low concentrations, the pyridine spectrum is faint, but it becomes significantly stronger as monolayer coverage is approached. This change in intensity is attributed to the orientation of the pyridine ring on the metal surface. Initially, the molecules lie parallel to the surface, but as the concentration increases, the pyridine rings are forced into a perpendicular orientation to allow for denser packing, resulting in a rapid rise in SERS intensity. The reason for this intensity alteration relates to the requirement for scattering, which necessitates a polarizability component perpendicular to the surface. When light interacts with the surface, it induces two electric dipole components: one parallel and one perpendicular to the surface. The molecular polarizability caused by the perpendicular component is responsible for scattering from the rough surface. In the case of pyridine, the plane of the ring yields the most significant polarizability changes. Thus, when the molecule lies parallel to the surface, the polarizability change primarily occurs parallel to the surface and does not contribute to scattering. Conversely, when the plane is perpendicular to the surface, the scattering process becomes efficient.

The appearance of new spectral bands further complicates the assignment of SERS spectra. This often occurs when a molecule possesses a center of symmetry, and adsorption onto a metal surface breaks this symmetry. As a result, the mutual exclusion rule, which governs normal Raman scattering, no longer applies, allowing some infrared-active bands to appear in the SERS spectrum. However, the situation is more intricate. Certain types of bands naturally exhibit higher intensity in SERS compared to normal Raman scattering. Selection rules primarily referring to electromagnetic enhancement, have proven useful in many cases, although the exact nature of the species formed between the adsorbate and the surface remains undefined in chemical enhancement. In practice, considering the molecule as a distinct entity and disregarding the impact of metal atoms, except for their influence on molecular symmetry, tends to be effective in most cases.

Although these selection rules have facilitated the determination of molecule orientation on the surface and provided explanations for discrepancies between SERS and normal Raman spectra, there is still much to learn about the factors influencing the intensities of SERS-active bands. The presence of selection rules presents a challenge in SERS as the appearance of new bands and the disappearance of existing ones make it difficult to establish a direct correlation between spectra obtained from the surface and those obtained from normal Raman scattering. Additionally, due to the immense sensitivity of SERS compared to normal Raman scattering (a factor of 106), dominant features in the spectrum can arise from surface-bound contaminants. These challenges make definitive assignments challenging. Overcoming these difficulties is one of the key advantages of surface-enhanced resonance Raman scattering (SERRS). However, before delving into the advantages and disadvantages of SERRS, it is essential to discuss a few applications of SERS.

1.2.4 Factors Influencing SERS

The enhancement factor in SERS, as well as the SERS process itself, relies on various parameters[49], which include:

- Laser excitation characteristics: This encompasses the properties of the laser used, such as its wavelength, polarization, angle of incidence (in the case of a planar substrate), and other relevant factors.
- Detection setup: The configuration of the detection system plays a role, including factors like the scattering geometry (e.g., backscattering), the solid angle for collection, and whether the detection is polarized or unpolarized.
- SERS substrate: The properties of the substrate used in SERS are significant, including the material employed (typically silver or gold), its geometry, orientation with respect to the incident beam direction and polarization, and the refractive index of the surrounding environment (nM). The dimensionality of the substrate, such as whether it is a 2D planar substrate or 3D particles in a solution, is also an important parameter as it necessitates different sample preparation procedures.

- Intrinsic properties of the analyte: This pertains to the inherent characteristics of the analyte itself, particularly the Raman polarizability tensors of its modes or intrinsic Raman cross-sections.

- Analyte adsorption properties: The efficiency of analyte adsorption, the concentration of the analyte on the surface (surface coverage), the distance from the surface, the orientation of adsorption (fixed or random), and any modification of the intrinsic Raman polarizability induced by adsorption are important factors to consider. The chemical contribution to SERS is related to the modification of the intrinsic Raman polarizability, while the background and surface selection rules originate from the previous factors.

1.3 Photo-Induced Enhanced Raman Spectroscopy (PIERS)

In recent years, the application of light-based treatments has gained significant attention in the fields of medicine and nanoscience. This approach offers not only potential medical benefits, such as virus elimination and patient treatment, but also serves as a catalyst for structural transformations, improvements in spectral and electromagnetic properties, and enhanced functional performance of nanomaterials. Light irradiation, as a non-destructive method, has the ability to stimulate surface plasmons in noble metal nanoparticles and induce charge transfer in semiconductors at
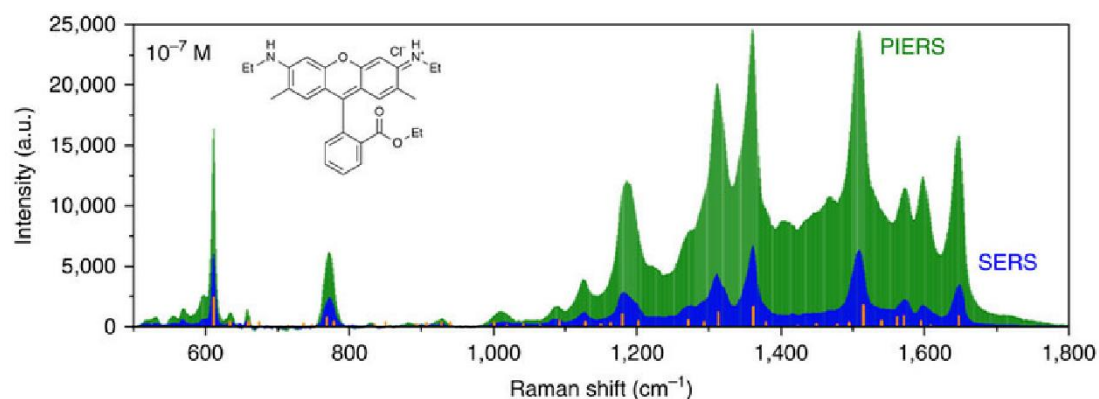

Figure 1.11: PIERS (green) and SERS (blue) spectra of Rhodamine 6G (10^{-7} M).

the nanoscale. These phenomena have made it a widely used technique in surface-enhanced Raman spectroscopy (SERS), a powerful analytical tool. However, due to the limitations imposed by the intensity and energy of the Raman laser, the excitation of electron-hole pairs in semiconductors is often insufficient, resulting in minimal or no enhancement of SERS signals.

In May 2016, a significant discovery was made by Parkin's group[50], demonstrating that the Raman signal of target molecules on a substrate consisting of Ag (and Au) nanoparticles on TiO_2 was greatly enhanced when the substrate was pre-irradiated with ultraviolet (UV) light for a specific duration. This phenomenon, as shown in **Figure 1.11** , was termed "photo-induced enhanced Raman spectroscopy" (PIERS). PIERS technique involves the simple step of light irradiation without any additional manipulation, making it a convenient and non-invasive approach. The amplification achieved through PIERS can be several times to dozens greater than traditional surface-enhanced Raman spectroscopy (SERS). While these values may not appear substantial, even a doubling of the enhancement factor can significantly improve sensitivity, which holds significance for applications in life sciences, environmental protection, and biological analysis. Extensive efforts have been made to develop various substrates and significant progress has been made in their application in PIERS. Currently, there are three operational procedures for PIERS. The first involves irradiating the substrate with light for a certain period, followed by analyte deposition and subsequent Raman analysis. The second procedure entails depositing the analyte on the substrate, followed by light irradiation and Raman analysis. Both these methods are performed ex situ, with analyte deposition and Raman detection occurring at separate locations. The third procedure allows for in situ operation, where the substrate is irradiated with incident light while performing Raman detection. Light-emitting diodes (LEDs) can be used as the light source, placed in proximity to the Raman laser, and operated simultaneously during Raman detection. PIERS offers several advantages over SERS, including broader detection capabilities for explosives, pollutants, biomolecules, and organic dyes at trace levels. It also exhibits a wider detection range for small molecules with low Raman cross-sections.

The application of light in photo-induced enhanced Raman spectroscopy (PIERS) extends beyond the deep UV range, as blue light and visible light have also been used as light sources. Furthermore, the active substrate for PIERS is not limited to the Ag (and Au) NPs-TiO_2 nanofilm; noble metal nanoparticles decorated on various semiconductor substrates, such as transition metal oxides, transition metal dichalcogenides, niobates, organic semiconductors, heterostructures, and even insulator substrates, have shown significant enhancement in PIERS. This technology has the

potential to complement SERS analysis effectively. However, as a novel technique, there is ample room for further development in PIERS, including substrate preparation, light selection, bioanalysis specificity, and more.

1.3.2 Mechanism of PIERS

The chemical mechanism (CM) in surface-enhanced Raman spectroscopy (SERS) typically results in enhancement factors (EF) of less than 10^3, which is lower compared to the electromagnetic mechanism (EM). However, recent studies utilizing semiconducting nanomaterials have demonstrated comparable enhancements in CM and EM. As a result, a combination of both mechanisms using metallic nanoparticles and semiconducting nanomaterials is commonly employed to enhance the sensitivity of SERS, enabling the detection of single molecules. The enhancement mechanisms of photo-induced enhanced Raman spectroscopy (PIERS) are still a subject of debate, with various models (Figure 1.12) proposed depending on the specific system being studied. Parkin's group suggested that the PIERS phenomenon originates from surface oxygen vacancy states in noble metal-metal oxide substrates[50–52]. Under pre-irradiation with UV light, oxygen vacancies are generated on the metal-oxide semiconductor surface through photoreactions with adsorbed O_2 and H_2O[53,54]. The number of vacancies increases with irradiation time, creating electron donor states below the conduction band edge. When the Raman laser is turned on, electrons can be injected from the oxygen vacancy states into the energy levels of the metal nanoparticles (NPs), leading to a shift in the NP's Fermi level and an increase in their electromagnetic field. This enhanced field significantly amplifies Raman scattering from molecules positioned in these "hot spots." In hybrid substrates, the plasmonic properties of the NPs provide additional electromagnetic enhancement. Additionally, the metal-semiconductor interface stabilizes the formation of oxygen vacancies, lowers the vacancy formation energy, extends carrier lifetimes, and enhances the photocatalytic potential of the metal-oxide semiconductor. The creation of oxygen vacancies is a common explanation for PIERS in the literature. However, in certain semiconductors like organic semiconductor diphenylalanine peptide and lithium niobate, where expelling oxygen atoms with UV photons is challenging, PIERS may arise from charge separation and migration within the semiconductors. Upon UV light irradiation with energy equal to or greater than the semiconductor's bandgap, free electrons are excited from the valence band to the

conduction band and subsequently transferred to the Ag NPs located at the semiconductor surface, leading to further enhancement of the Raman scattering signal from the analyte in contact with the NPs.

In a study conducted by Maalej et al., photo-induced enhanced Raman spectroscopy (PIERS) was observed in hybrid Au/WS_2 nanosheets. Contrary to previous models, the extra enhancement in this system was attributed to charge transfer (CT) from the Au nanoparticles (NPs) to the WS2 nanosheets. Under UV light irradiation, the localized
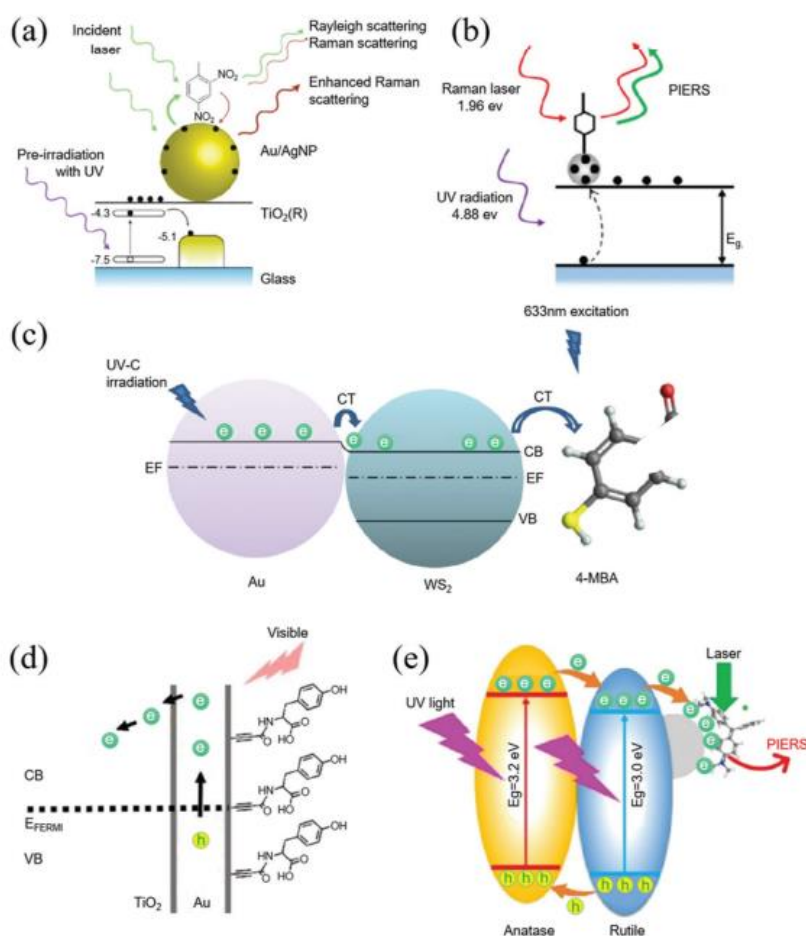
Figure 1.12 Schematic illustration of the proposed mechanisms for PIERS: (a) photo-induced oxygen vacancy in the semiconductor by UV light and charge transfer in the metal–semiconductor contact (reproduced with permission from ref. 17. copyright 2017, Springer Nature Publishing); (b) photogenerated carriers at the semiconductor surface by UV light transferring to the metal NPs (reproduced with permission from the author of ref. 46); (c) photoexcited electrons at the metal surface by UV light transferring to the semiconductor (reproduced with permission from ref. 19. Copyright 2020, ACS publishing); (d) photogenerated carriers at the semiconductor heterostructure by UV light transferring to the metal NPs (reproduced with permission from ref. 24. Copyright 2020, ACS publishing); (e) photoexcited electrons at the metal surface by visible light transferring to the semiconductor

surface plasmon resonance (LSPR) of the Au NPs creates hot spots and induces CT

from the Au NPs to the WS2, resulting in additional electrons being injected into molecules adsorbed on the WS2 surface through its conduction band. This photo-induced CT increases the molecular polarizability tensor and amplifies the Raman signals through the Herzberg-Teller coupling. Similar principles apply to radiation by visible light or even the Raman laser.

In another case, Liu's group observed the PIERS effect with a larger enhancement factor in heterogeneous TiO_2-Ag hybrid nanowire arrays. The heterojunction interface effectively separates electrons and holes in space. Upon UV light irradiation, electrons in the valence band of both anatase and rutile TiO2 are excited to the conduction band. Due to the lower conduction band of rutile TiO2 compared to anatase TiO2, rutile TiO2 acts as an electron acceptor, resulting in a significantly increased electron density on its surface and potentially leading to additional PIERS enhancement in the mixed-phase TiO_2-metal hybrid.

These different models indicate that the enhancement in PIERS involves two components: chemical enhancement (CM) from CT between the semiconductor and metal NPs, and electromagnetic enhancement (EM) from electron aggregation or release in the NPs. The CT interaction between the semiconductor and metal NPs is crucial for the enhancement, regardless of the direction of CT (from semiconductor to metal or vice versa). Physicochemical parameters, such as the absorption and extinction spectra, can be used to analyze the changes in electron density on the particles after light irradiation. Other indicators, such as photoluminescence intensity and photocurrent, can also demonstrate the effects of increased charge carriers under light radiation.

1.3.3 Substrate Dependance

The selection of an appropriate substrate[55] is crucial for achieving effective photo-induced enhanced Raman spectroscopy (PIERS) because it determines the contributions of chemical enhancement (CM) and electromagnetic enhancement (EM) under fixed wavelength and duration of photo-irradiation. These substrates are not limited to simple hybrid nanomaterials consisting of noble metal nanoparticles (NPs) and metal-oxide semiconductors. They can also include transition metal dichalcogenides, niobates, organic semiconductors, heterostructural metal-oxide

semiconductors, and insulators. To maximize the enhancement factor (EF), substrates are typically designed with specific nanostructures that offer a large surface area and facilitate efficient charge transfer pathways.

A summary of the maximum enhancements achieved for various substrates in PIERS studies conducted thus far, can be classified into three groups based on their constituents. The first group comprises hybrid noble metal-semiconductors, where gold (Au) and silver (Ag) are the primary noble metals utilized due to their surface plasmon resonance (SPR) properties in the visible wavelength range[56]. Metal/TiO_2 substrates exhibit distinct PIERS effects under different incident light wavelengths, with shorter wavelengths and longer irradiation periods generally resulting in larger EFs (further elaborated in the following section).

Heterostructured anatase/rutile TiO_2-Ag, achieved an enhancement factor (EF) of 27.8. Although the EF value was lower than that of rutile TiO_2-Au, this heterogeneous substrate exhibited stronger enhancement compared to others when detecting the same molecules under similar conditions. For instance, the EF for R6G was 4.19 in rutile TiO_2-Au, whereas it reached 14.9 in anatase/rutile TiO2-Ag. The significant Raman enhancement can be attributed to highly efficient charge transfer from anatase to rutile and then to Ag, driven by the heterojunction between anatase and rutile. Similarly, in a single-element semiconductor coated with Ag NPs, the Raman signal was enhanced by 2.5 times compared to regular SERS.

Hence, the selection of a photo-active substrate is critical for the PIERS effect, and the Raman enhancement of a substrate depends on several factors, including the incident light wavelength, irradiation duration, experimental procedures, analyte molecules, and the choice of the active Raman scattering band.

The second group of substrates consists of hybrid noble metal-insulators. In an Au NPs-SiO_2 thin film, a 2-fold enhancement was reported when irradiated with 254 nm UV light for 4 hours. This enhancement may be attributed to the incident light's ability to create oxygen vacancies on the SiO_2 surface, even though the photon energy is lower than the insulator's bandgap. Subsequently, the Raman laser expels electrons from the vacancies and injects them into the energy levels of the Au NPs, thereby improving the Raman signal. However, Rice et al. observed no change in the Raman spectrum of an Ag NPs-SiO2 thin film when irradiated with 365 nm UV light. This lack of

enhancement may be due to the lower energy of the incident photons, which cannot create oxygen vacancies or facilitate charge expulsion from vacancies to the conduction band.

The last group consists of single semiconductors. In a lithium niobate thin film, the Raman signal intensity doubled under sample irradiation. This implies that even without coating noble metal NPs, the Raman signal can still undergo chemical enhancement. However, in a TiO2 thin film[57], no enhancement was observed under substrate irradiation. This difference can be attributed to the lifetime of photoexcited carriers, which is picoseconds-to-microseconds in TiO2 and hundreds of milliseconds to tens of seconds in lithium niobate. Therefore, it is advantageous to enhance the PIERS effect by prolonging the lifetime of electron-hole pairs. This can be achieved through the use of pure semiconducting nanomaterials with long carrier lifetimes, heterojunctions, or combinations of metals and semiconductors. Moreover, besides substrate composition, the PIERS effect is influenced by the substrate's morphology and structure. For example, periodically poled lithium niobate exhibits different Raman scattering intensities for transverse and longitudinal optical phonons, which are influenced by mechanical stresses and partially screened depolarization fields. Anisotropic substrates like periodically poled lithium niobate can create specific plasmon-active nanoparticle patterns, as achieved through ferroelectric lithography-based methods. These patterns can induce different PIERS enhancements for different analyte bands and locations. Similarly, TiO2 crystals exist in three different structures: rutile, anatase, and brookite. Each structure possesses distinct refractive indices, surface energies, band structures, total density of states, and other properties, which implies that they may respond differently to light irradiation.

1.3.4 Irradiation Dependance

The effects on PIERS vary depending on the wavelength of the incident light due to differences in photon energies. Typically, the energy of the incident photons must be equal to or greater than the bandgap energy of the semiconductor substrate. This allows for the separation of electron-hole pairs and the expulsion of electrons to states of oxygen vacancies or the conduction band. In such cases, the Raman signal is enhanced with increasing irradiation time. However, if the photon energy is lower than the bandgap energy of the semiconductor substrate or if the substrate is photo-inactive, the

Raman signal remains stable under light irradiation. It is also important to limit the intensity of the light source to avoid degradation of the analyte molecules.

The Raman enhancement does not simply increase continuously with prolonged irradiation for photo-active substrates. In the Ag@TiO2 heterostructure, for example, the Raman signal is initially intensified but then weakened after a critical irradiation time (Tirr). The Tirr for maximum enhancement differs for different chemical substrates, nanostructures, and analyte molecules. Additionally, the behavior of the Raman signal varies depending on the substrate. For instance, on the Au@TiO2 substrate, the Raman signal initially decreases for about 3 minutes, then steadily increases for about 12 minutes to reach a maximum enhancement value and remains stable with continuous irradiation. On the Au@WO$_3$ substrate, the Raman signal steadily increases initially but then rapidly increases after around 20 minutes. On the Au@ZnO substrate, apart from an initial decrease due to laser-induced degradation of the analyte molecules, the profile is similar to that of the Ag@TiO$_2$ heterostructure, but the variation occurs over a shorter time. The distinct changes observed may be related to the microstructure, crystallinity, charge state, and Zn-O bond energy of the ZnO thin film. In the case of the Ag@LiNbO$_3$ substrate, the Raman signal experiences a sudden increase upon initial irradiation, followed by an abrupt drop after Tirr. According to a model proposed by Parkin's group, the time-dependent changes in the measured Raman signal primarily depend on oxygen vacancy formation, vacancy healing, and laser-induced bleaching of the analyte molecules. The maximum enhancement under photo-irradiation suggests an equilibrium between enhancing and decay mechanisms, indicating a balance among these factors. The increasing enhancement before Tirr is a result of vacancy formation overwhelming, vacancy healing and analyte bleaching, while the decreasing enhancement is the opposite.

1.4 SERS Plasmonic Nanosensors

In recent years, the remarkable advancements in Surface-Enhanced Raman Scattering (SERS) technology have propelled the development of highly sensitive and selective sensing platforms. Among these, SERS plasmonic nanosensors[58] have emerged as a groundbreaking approach, integrating plasmonic nanomaterials into the realm of nanoscale detection. By harnessing the unique properties of noble metal nanoparticles, such as gold and silver, these nanosensors exhibit unprecedented

amplification of Raman signals, enabling the detection and characterization of minute quantities of analytes.
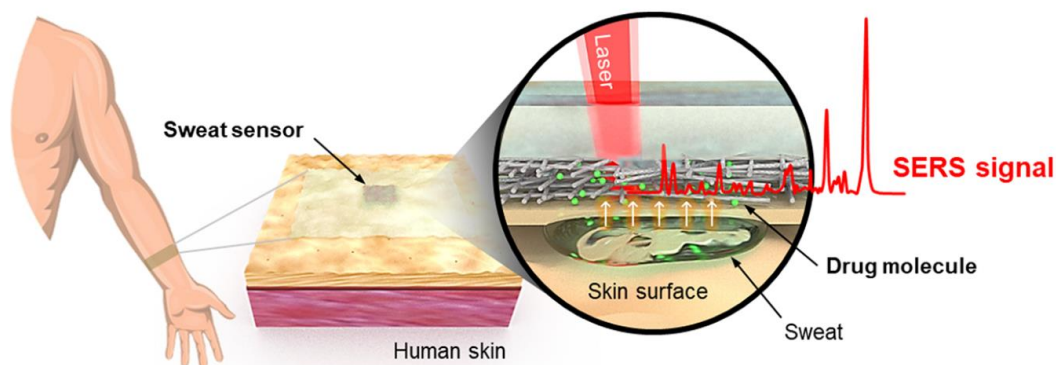

Figure 1.13: Schematic illustration of a wearable SERS patch sensor describing a label-free SERS detection of drug molecules in sweat.

1.4.1 Chemical Sensors

A chemical sensor typically consists of a molecular recognition unit, a receptor, and a transducer that can convert a measurable signal into a binding recognition event. Surface-enhanced Raman scattering (SERS) is an exciting analytical tool that provides molecular-specific data with high sensitivity, allowing the study of single analytes or multiple species simultaneously. SERS stands out among other analytical techniques due to its ability to provide rich vibrational spectroscopic information. It finds applications in various fields such as electrochemistry, catalysis, biology, medicine, art conservation, and materials science.

Chemosensors, also known as molecular sensors, are analytical devices used for detecting analytes. They typically consist of a signaling moiety and a recognition moiety that generates a visible signal or signal shift in the presence of the analyte. Surface-enhanced Raman scattering-based chemosensors utilize plasmonic nanoparticles or nanostructures functionalized as receptors with binding ligands, enabling selective identification of the target analyte. The interaction between the analyte and ligand either eliminates or generates a new SERS signal. This approach offers highly selective sensors and allows for quantitative analysis using the chemosensor as a standard. The high sensitivity and narrow bandwidth of the molecular fingerprint in SERS chemosensors enable differentiation of molecules with similar structures.

Chemical contaminants found in various environments include organic herbicides, insecticides, phthalates, polychlorinated biphenyls (PCBs), polycyclic aromatic hydrocarbons (PAHs), dioxins, and others. Direct SERS analysis in normal and polluted waters can be challenging due to nonspecific adsorption of other substances in the solution, which hampers the detection of the target analyte and reduces assay sensitivity. To overcome these issues, a SERS substrate based on a microporous silica capsule with gold nanoparticles has been developed. The microporous structure acts as a molecular sieve, preventing large biomolecules and cells from accessing the plasmonic portion while maintaining colloidal stability. This substrate has been used to detect pesticide contaminants in river water. Additionally, a bimetallic Au/Ag ternary film-packaged chip with polymer films has been manufactured to create more robust and functional SERS sensors for on-site detection of specific pollutants.

To detect polyatomic anions (e.g., perchlorate, nitrate, nitrite ions) and heavy transition metal cations (e.g., copper, arsenic, chromium, lead, mercury, cadmium, copper), which are major environmental pollutants, innovative and enhanced methods with high sensitivity and selectivity are required for trace-level detection. These pollutants are typically present in low concentrations, and environmental screening aims to detect their trace quantities.

1.4.2 Biological Sensors

A biomolecule refers to a molecule derived from living organisms, consisting of low molecular weight substances such as amino acids, nucleotides, fatty acids, monosaccharides, and vitamins, which serve as the building blocks of life. These compounds primarily contain carbon, oxygen, hydrogen, sulfur, nitrogen, and phosphorus. Additionally, macromolecules such as nucleic acids, proteins, lipids, and carbohydrates are formed from these biopolymer monomers and hold significant biological importance.

Biosensors are utilized for qualitative and quantitative analysis of biomolecules[59,60]. Their primary function is to monitor biological processes within the body[61] and diagnose diseases. Biological reactions often occur in complex water environments, and both in-vivo and in-vitro methods are commonly employed for analysis. In-vitro methods allow for the study of the temporal evolution of biochemical reactions, while

in-vivo methods enable the examination of detailed mechanisms and dynamic reactions.

Surface-enhanced Raman spectroscopy (SERS) has gained considerable attention as a powerful analytical technique for studying biological samples[62]. It provides detailed information about living cells and biological reactions, facilitating the understanding of drug or toxic agent interactions, diseases, and cell death. Resonant Raman spectroscopy and coherent anti-Stokes Raman spectroscopy, in addition to traditional nonresonant Raman spectroscopy, are increasingly contributing to the study of living cells. SERS finds wide applications in biomedical and bioengineering fields due to its high sensitivity and selectivity resulting from the optical properties of plasmonic nanostructures. It has become a valuable analytical tool for examining molecular-level reaction phenomena, particularly enzyme-catalyzed reactions. However, a common challenge is preserving the structure of biomolecules, such as protein denaturation on the bare metal surface, which can reduce bioactivity and function. SERS enhances Raman signals by orders of magnitude compared to traditional Raman spectroscopy, achieved through the use of suitable SERS substrates. Consequently, SERS has been extensively employed in biological research alongside other analytical tools.

In the biological field, SERS is divided into two main areas: fundamental, where it is used to investigate biomolecule structures, conformations, and charge transfer; and biomedical diagnostics, which can be direct or indirect. SERS-based biosensors offer several advantages:

a) They capture the fundamental molecular information and exhibit high sensitivity to examine individual molecules.

b) Compared to fluorescence spectroscopy, SERS produces sharp peaks and demonstrates good resistance to photo-degradation and photo-bleaching.

c) Multiple choices of signal enhancement substrates with various sizes and shapes make it suitable for diverse applications.

d) SERS allows for deep laser penetration, enabling its application in in-vivo and in-vitro diagnostics and imaging.

1.5   M. Sc. Thesis Scope

The main aim of the present Masters Thesis is to develop a method of fabricating SERS active substrates via one-step Flame Spray Pyrolysis technology. The Nanosensors that will be fabricated are divided in two categories: **AgSiO$_2$**, and **AgTiO$_2$**.

For **AgSiO$_2$** nanofilm the following FSP parameters will be changed each time in order to find the optimum sensing factors:

- Three deposition times of NPs in the substrate will be followed, 100s, 60s and 40s.
- Three cases of silica percentage will be used, 6%, 10% and 20% wt.

Subsequently, 9 different nanofilms will be fabricated for AgSiO$_2$ behalf.

For **AgTiO$_2$** nanofilm the deposition time will again vary from 100s to 40s and additionally two TiO$_2$ molarities will be followed, 0.6M and 0.3M. Also, sequentially deposited substrates will be fabricated. Totally, 8 nanofilms will be fabricated on behalf of **AgTiO$_2$.**

Next goal is to characterize the already fabricated nanofilms based on their SERS efficiency. The Raman Reporters that will be used for the forementioned characterization are 4-MBA, which thanks to its high adsorption will me used for the main analysis, and Rhodamine 6G will be also used for further characterization. The Enhancement Factor will determine how effective our substrate is compared with other from bibliography.

As an application SERS detection in the pesticide Thiram will be managed to be achieved in order to determine the EF for a real case sensing scenario.

Consequently, in the already SERS active substrates will be illuminated with UV radiation in order to study the PIERS effect. The AgTiO$_2$ substrate will be used since contains a photoactive semiconductor. The formation of oxygen vacancies is necessary for the effect and it will be studied as well as their interaction with air.

Finally, PIERS effect will be used in order to exceed the Limit of Detection in the case of AgTiO$_2$ nanofilm.

Chapter 2

Experimental Methods

2.1   Flame Spray Pyrolysis

Particle generation through the combustion process, particularly the production of soot and carbon black, has been a part of human history. It can be traced back to prehistoric drawings on cave walls and artistic creations by ancient civilizations such as the Greeks, Egyptians, Indians, and Chinese [63]. In modern times, aerosol reactors have been developed to synthesize fine nanoparticles[64]. By rapidly heating and cooling materials during combustion, unique structures, morphologies, high purity, and compositions can be achieved, leading to the creation of particles or films. The flame process has been utilized for several years to manufacture pigmentary titania (TiO_2) and fumed silica (SiO_2) powders in the market .

In recent decades, significant progress has been made in understanding the quantitative aspects of aerosol formation during combustion. These advancements have brought about revolutionary changes, allowing for the production of flame-made materials with controlled characteristics, enabling thorough examination of their effectiveness[63]. Ulrich G. D. (1984) anticipated that future developments in flame technology would yield new materials for catalysis, composites, and various applications[65]. Undoubtedly, his predictions have been surpassed, and numerous materials have since been tested for catalytic purposes[66] , sensors[67] , fuel[68,69], electronics, biomaterials[70] , and medical applications[71] . Flame spray pyrolysis (FSP) is a one-step flame process that enables the production of multifunctional nanostructures with tailor-made properties. Expertise in FSP encompasses knowledge in chemistry, materials science, mechanical engineering, thermodynamics, and particle dynamics during flight.

2.1.1 Basic Principles

A typical flame spray pyrolysis (FSP) reactor consists of three main components: an atomizer, a burner, and a collecting system[72] . In Figure 2.1, it is illustrated that the liquid precursor needs to be atomized into droplets of micron size. Various techniques can be employed for atomization, such as ultrasonic, electrostatic, or air blasts. The size, velocity, and rate of atomization of the droplets play a crucial role in the entire FSP process. The atomized droplets are sprayed into the flame environment at the burner.
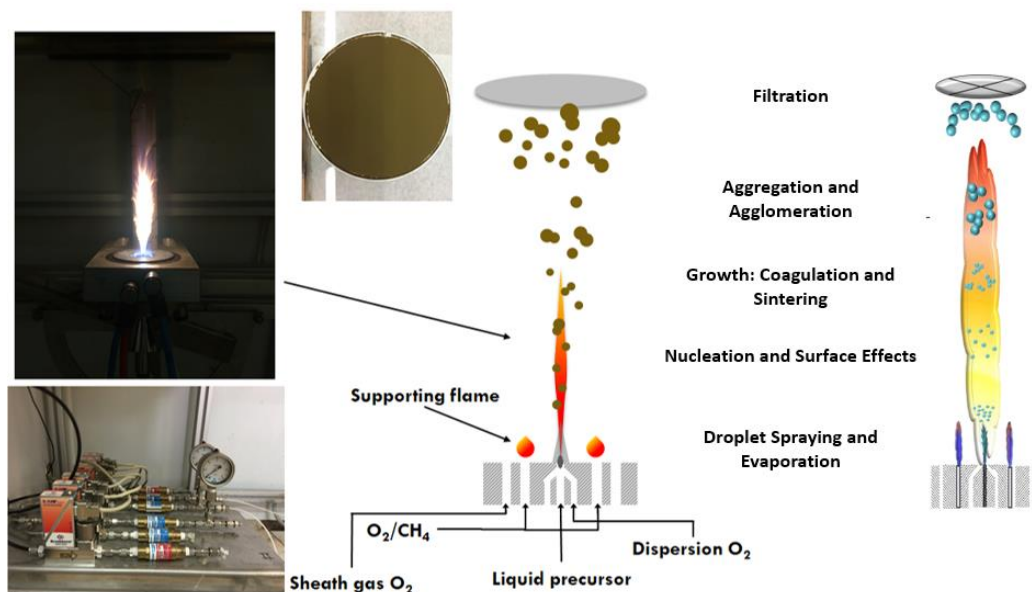
Figure 2.1 Flame Spray Pyrolysis (FSP) apparatus, Dept. of Physics, UOI

The burner can be classified into two types: diffusion burner and premixed burner. In a diffusion burner, the fuel (CH_4) and the oxidant (O_2) are not mixed until they enter the flame zone. On the other hand, a premixed burner involves mixing the oxidant (O_2) and fuel (CH4) prior to entering the flame zone. The premixed fuel and oxidant form the pilot flame, where the dispersing gas (O_2) determines the angle at which the droplets are nebulized. Additionally, the dispersing gas aids in converting the precursor into micron-sized droplets and acts as an extra oxidant in the flame environment.

To protect the flame environment and assist in the collection of nanoparticles, an additional flow of O_2 gas called sheath O_2 is introduced to create an upward stream. The liquid precursor is injected into the flame environment in the form of droplets.

These droplets undergo combustion, and the resulting particles are subsequently collected on a glass fiber filter.

2.1.2 Particle Formation

In the field of Flame Spray Pyrolysis (FSP), there are two main pathways through which particles are formed (Figure 2.2): droplet-to-particle and gas-to-particle[73]. It is important to note that particle formation does not solely occur through the droplet-to-particle pathway, despite the precursor being sprayed in micron-sized droplets into the flame environment.
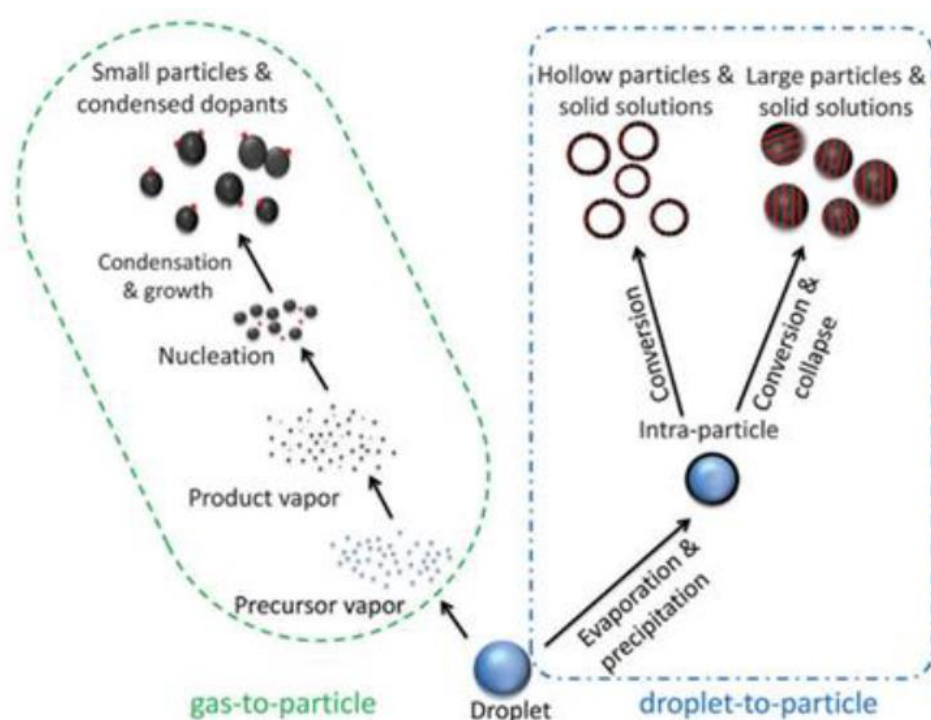
Figure 2.2 The two main pathways through which particles are formed: droplet-to-particle and gas-to-particle.

In the particle formation process, there are two key factors that influence the final product[74]: the combustion enthalpy density and the fraction T_{bp} /$T_{d,mp}$. T_{bp} represents the boiling point of the solvent, while $T_{d,mp}$ refers to the decomposition point of the metal precursor. It has been observed that high combustion enthalpies (>4.7 kJ/ggas) and T_{bp} / $T_{d,mp}$ ratios greater than 1.05 result in the production of homogeneous powders. The liquid precursors typically used are metalorganic compounds, which contribute only a small fraction of the total combustion enthalpy. The majority of the combustion enthalpy is derived from the solvents, particularly high enthalpy solvents like xylene.

In the gas-to-particle route, the Tbp / Td,mp ratio exceeds 1.05, causing the precursor to decompose before the solvent evaporates. When the precursor spray ignites and reacts exothermically, the precursor decomposes, generating metal vapor in the hot flame environment (approximately 2400°C). Under these conditions, molecular nanoclusters form through nucleation. These nanoclusters, driven by Brownian motion and differences in their velocities, collide with each other, leading to coagulation. Coagulation is the primary mechanism for growth. During this growth process, particles collide and adhere to one another, either maintaining their individual shapes or fusing together to form spherical particles. This sintering process, known as coalescence, determines the final particle morphology. The temperature profile (cooling rate) and primary particle size play a significant role, and the resulting particles can be classified as single particles, aggregates (with primary particles connected by strong sinter necks), or agglomerates (with primary particles held together by weak van der Waals bonds). When sintering occurs faster than coagulation, single particles are formed. If sintering and coagulation rates are comparable, aggregates are formed. When sintering is negligible, agglomerates are formed.

In the droplet-to-particle route, the Tbp / Td,mp ratio is less than 1.05, causing the solvent to evaporate before the precursor decomposes. As a result, the precursor is left in the high-temperature zone. The size of the nanoparticle depends on the size of the droplet. The precursor accumulates on the outer layer of the droplet, preventing further vaporization of the solvent. In this scenario, precipitation occurs, and if it happens rapidly, a shell forms outside the droplet, leading to the formation of shell-like particles through a process known as micron-explosion. Other products include micron-sized particles.

Figure 2.1 illustrates additionally outlines the step-by-step process of particle formation and growth, starting from the spraying of the precursor into the flame zone and resulting in the production of powder. When following the droplet-to-particle pathway, the particle formation mechanism involves the following steps:

- Aerosol pyrolysis occurs, where the precursor dissolves in solvents, is atomized into micron-sized droplets, and is sprayed into the high-temperature zone, which is the flame.

- The precursor spray ignites, releasing energy in an exothermic manner. This leads to the decomposition and evaporation of the precursor, producing metal vapor.

- Exothermic combustion reactions between the precursor and organic solvents create extreme conditions for the formation of molecules and clusters (monomers) through nucleation or direct inception. These monomers then grow into nanoparticles through coagulation, as depicted in Figure 3.1. Coagulation happens when there is a high concentration of particles in the aerosol, resulting in particle collisions driven by Brownian motion and leading to strong adhesive forces or chemical bonds.

- The coalescence or fusion process contributes to the formation of single particles from multiple nanoparticles. This occurs due to intensive aggregation in the high-temperature region of the flame, facilitated by sintering effects.

- As the aerosol stream exits the high-temperature zone and enters the reactor, coalescence is completed as the temperature decreases. Particle growth continues through coagulation, forming aggregates of primary particles with strong chemical bonds and agglomerates of primary particles held together by weak physical bonds, such as Van der Waals forces.

The collected powder product consists of aggregated nanoparticles. The degree of aggregation, which refers to the morphology of the particles, impacts their final properties and determines their applications. Typically, aggregated systems contain a varying number of primary particles, ranging from a few to hundreds, with sizes ranging from 1 to 500 nm. Residence time and process temperature play crucial roles in determining the extent of aggregation. Aggregated nanoparticle systems are formed through coagulation and coalescence, with aggregates being produced when the collision rate is higher than the sintering rate.

In flame aerosol processes, metal oxides are thermodynamically favored products. However, controlling suitable parameters for metal synthesis is challenging due to the oxygen-rich environment inside the FSP reactor. One advantage of flame technology is its scalability. By enclosing the FSP flame in a tube, the entry of ambient air is prevented while maintaining the convection heat inside the reactor. This enclosure restricts the presence of oxygen (except for controlled sources like dispersion) and

reduces oxidative conditions, enabling the production of fine metallic nanoparticles. The enclosed system promotes longer residence time and higher flame temperature.

In conclusion, residence time and high temperatures are key factors driving particle formation and growth, purity and crystallinity, and the dominance and extent of coagulation/coalescence, which ultimately affect the properties and characteristics of the final powder product. However, monitoring these factors is complex as they are influenced by various FSP parameters, ranging from precursor solution concentration to the effects of external air.

2.1.3 FSP Powder Set-Up

The FSP (Flame Spray Pyrolysis) equipment utilized in this study is set up in the Nanomaterials' Lab, located in the Physics Department of the University of Ioannina. This arrangement is depicted in Figure 2.3. Also, a detailed image of the FSP burner configuration.
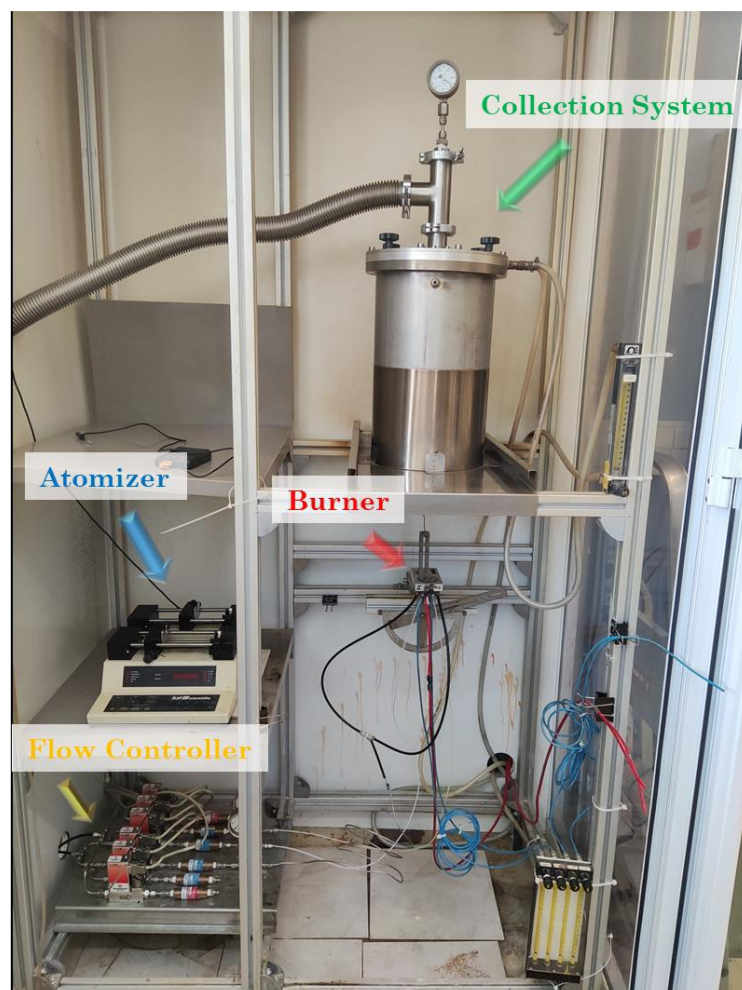
Figure 2.3 FSP reactor with its components .

The FSP reactor consists of several components, as follows[75,76]:

- Burner: This part of the FSP reactor, which is displayed in Figure 2.4, includes a gas-assisted nozzle, which is a capillary tube with specific dimensions (outer diameter of 0.5 mm and inner diameter of 0.6 mm). It is positioned within an opening of 0.8 mm, creating an annular gap. The burner is responsible for igniting the flame using oxygen (O_2) and methane (CH_4) gases. The supporting gases and

Figure 2.4 FSP burner demonstration.

precursor dissolved in solvents flow through the capillary tube, while the dispersion gas flows through the annular gap. The optimal dispersion/spray angle is determined by the height of the capillary above the nozzle opening.

- Atomizer: The atomizer (Figure 2.6) is a crucial part of the FSP reactor that converts the liquid precursor into micron-sized droplets. Atomization occurs before spraying and plays a significant role in increasing the surface area of the droplets, leading to higher combustion and vaporization rates. The droplets are then transferred to the burner for spraying using a syringe pump. The size of the droplets is controlled by adjusting the liquid-to-gas mass ratio.
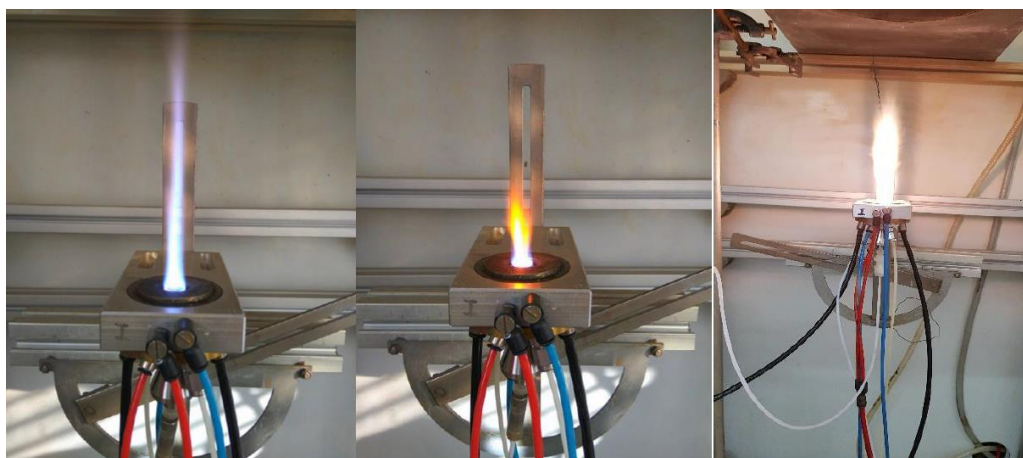
Figure 2.5 (Left): Pilot flame. (Middle): Dispersion. (Right): Precursor combustion

Figure 2.6 On the left the FSP atomizer, on the right the glass fiber filter in collection process.

- Collector: After the spray pyrolysis process, the resulting particles are collected as powder. This collection is facilitated by a thin fiber filter, which captures the particles, and a vacuum pump, which aids in the collection process (Figure 2.6).

2.1.4 FSP Nano-Film Fabrication

The advantages of the FSP (Flame Spray Pyrolysis) method have sparked extensive research into developing FSP reactors and understanding the influence of precursor chemistry on the morphology and structure of the final products. Furthermore, FSP has been adapted to fabricate nano films composed of nanoparticles with adjustable porosity, exhibiting exceptional performance in chemical sensors, photodetectors, and solar cells[77,78] . FSP-made powders can also be used to create films by casting or dropping, but these films tend to be relatively dense with uneven coverage resulting from the wetting processes and solvent evaporation, lacking a three-dimensional hierarchy.

In this thesis we have successfully directly fabricate robust transition metal oxide films on solid substrates using FSP. These films exhibit promising performance as active SERS sensors, detecting pesticides with high efficiency.

Figure 2.7 illustrates a schematic of the FSP (Flame Spray Pyrolysis) setup utilized for the one-step production of transition metal oxide films. The equipment is the same with
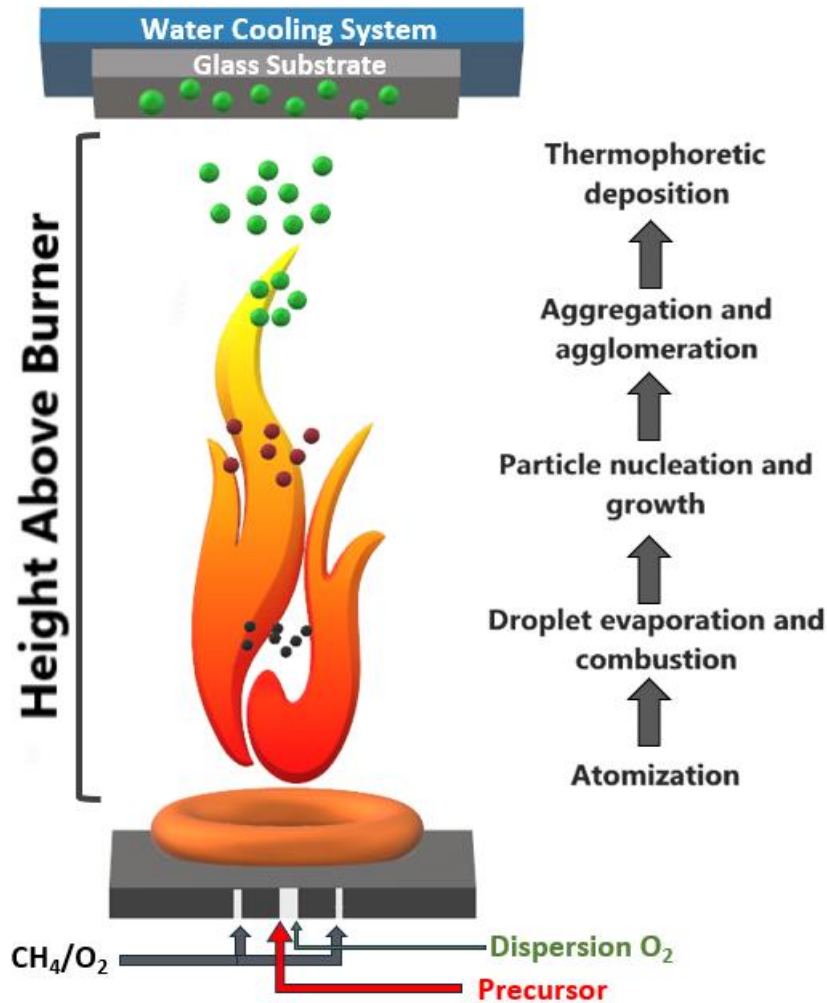
Figure 2.7 Schematic diagram of the experimental procedure to fabricate SERS sensing films in one-step.

the powder FSP set up with the addition of a water-cooled holder for the substrate which ensures the a large thermophoretic deposition rate.

The process involved the feeding of a solution containing precursors into a capillary, followed by the atomization of the solution into small droplets using pure oxygen. These fine droplets were then ignited by a pilot flame, leading to the formation of a spray flame. Within this flame, a series of complex reactions occurred, including droplet evaporation and combustion, particle nucleation, growth through coalescence and sintering, as well as aggregation and agglomeration[79]. As a result of these processes, nanoparticles were generated. To achieve direct deposition of these freshly formed nanoparticles onto a glass substrate, thermophoresis was employed.

In the context of nanoparticle deposition, thermophoresis is used to direct the motion of nanoparticles towards a cooler substrate[45]. The temperature difference between the flame and the substrate creates a thermal gradient, and the nanoparticles, being hotter in the flame, move towards the cooler substrate due to thermophoretic forces. This selective migration allows for the direct deposition of nanoparticles onto the substrate, enabling the formation of thin films or coatings.

The extent of thermophoretic deposition depends on various factors, including the temperature gradient, particle size, particle-fluid interactions, and the properties of the fluid medium. By controlling these factors, it is possible to manipulate the deposition process and achieve desired film characteristics, such as thickness and nanoparticle distribution.

 Due to the highly exothermic nature of FSP liquid precursor combustion, the flame temperature can reach temperatures of up to 1000°C. Therefore, to create FSP-made porous films, an optimal height above the burner (HAB) is chosen to induce a certain degree of nanoparticle sintering, and the substrate is water-cooled to prevent damage. Under these experimental conditions, the porosity of the FSP-made films can be adjusted. Films fabricated at HAB values of 10 cm and above exhibit high porosity and large surface areas but suffer from poor mechanical adhesion to the underlying substrate[80]. Although post-thermal treatments have been employed to mitigate this issue, these films still struggle with enduring repeated measurements during gas evolution reactions on their surface, as well as strong capillary forces acting on the pores formed between the nanograin boundaries[80] .

   However, the high porosity of the deposited films poses a significant challenge as it limits their mechanical stability, thereby restricting the use of FSP-fabricated films in liquid environments. To address this issue, Kühne et al. and Tricoli et al. integrated FSP with recent advancements in microtechnology[81], leading to the development of a new generation of micromachined, smart, single-chip gas sensors. The FSP unit was combined with a water-cooled substrate for synthesis, and a shadow mask was employed for the direct deposition of thick layers of nanoparticles. The nanoparticles were also deposited through the pores of the shadow mask onto micro-hotplates that were micromachined on wafers. These micro-hotplates consisted of a sensitive area measuring 300×300 µm², Pt-interdigitated electrodes, an embedded heater, and three

temperature sensors. During deposition, the substrate was maintained at approximately 150 °C to ensure a high thermophoretic deposition rate. Subsequently, the layers were annealed in situ by directing a particle-free xylene spray flame onto the shadow mask for a duration of 30-60 seconds to achieve mechanically stable layers[82].. It is important to note that the particle deposition in the initial step is characterized by a distinct "in-flame-agglomeration" control regime due to the low substrate temperature. However, during the subsequent in situ annealing, an "on-substrate-sintering" regime takes place at high flame temperatures[83]. This transition causes the lace-like layers to transform into compact cauliflower-like structures, resulting in a significant reduction in specific surface area (SSA). The separation of these two regimes at different stages of the FSP fabrication process enables the production of novel micro-patterned stable functional inorganic nanomaterial layers[84].

2.1.5 FSP Film Set-Up

The Flame Spray Pyrolysis (FSP) Film Set-Up employed in this research is installed within the Nanomaterials' Laboratory, situated in the Department of Physics at the
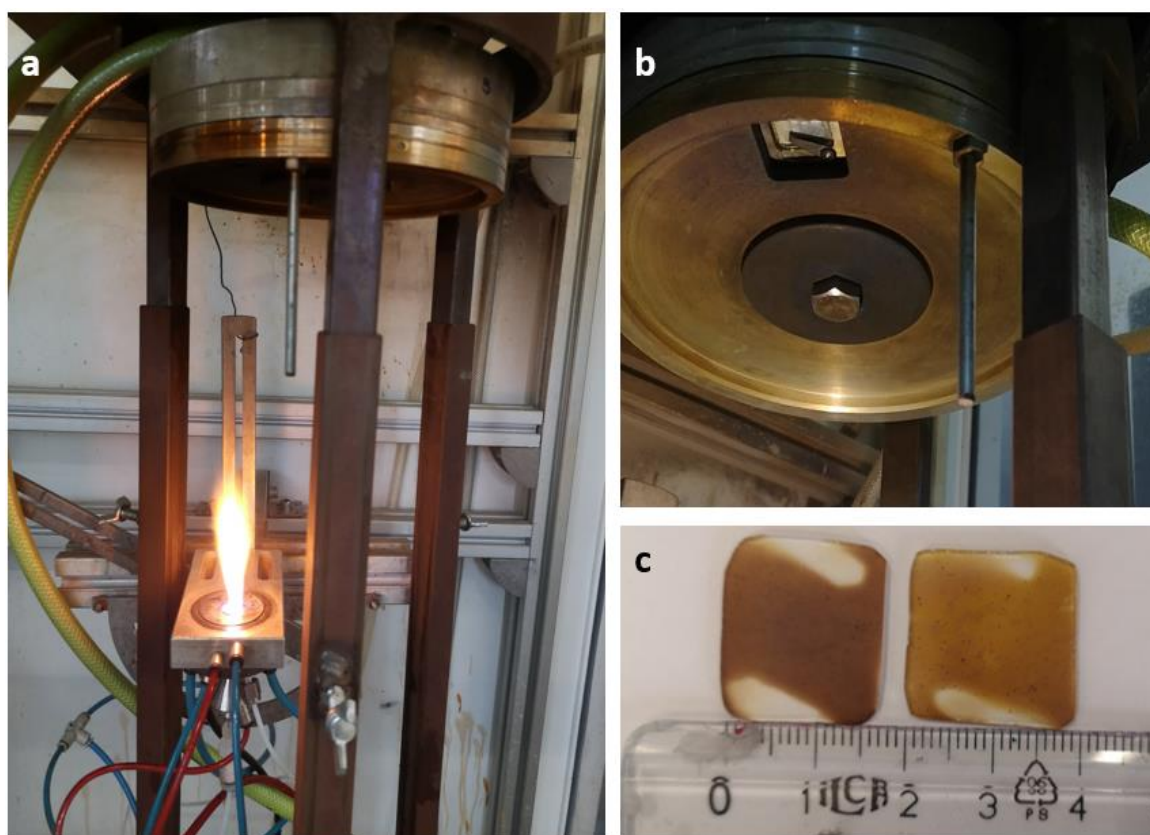
Figure 2.8 a) FSP Film Set-Up, b) Watercooled holder while FSP process in on-going, c) demonstration of successful Film deposition

University of Ioannina. The schematic representation of this setup can be observed in Figure 2.6. Additionally, a more detailed illustration of the water-cooled holder is demonstrated in Figure 2.9, the metallic

Figure 2.9 Watercooled holder of FSP-FILM Set-Up with 10 spots available.

2.2   Raman Spectroscopy

More than 80 years have passed since the discovery of the Raman effect[85], and Raman spectroscopy has emerged as a crucial method in various analytical and structural determination techniques. The advent of lasers in 1960 has revolutionized Raman spectroscopy and introduced valuable new techniques. Among these, surface-enhanced Raman scattering (SERS), discovered in 1977, stands out as a highly significant and intriguing finding. Under specific conditions, molecules adsorbed onto metal surfaces exhibit an unusually large interaction cross section for the Raman effect. Despite its long history, the field of SERS continues to flourish with recent advancements that have significantly increased the sensitivity of measurements and unveiled new phenomena with practical applications. SERS measurements are expected to play an increasingly vital role in chemistry, biochemistry, and biophysics[86].

Laser Raman spectroscopy involves the measurement of radiation scattered from various types of samples, including solids, liquids, and gases. While any light source

can be used, the low intensity of Raman scattered radiation typically necessitates the use of laser radiation for excitation.

The Raman effect refers to the inelastic scattering of light by matter. When a molecule interacts with a photon of visible light that lacks sufficient energy to induce electronic transitions, the photon can be scattered in three ways. It can be elastically scattered, retaining its incident energy (known as Rayleigh scattering), or it can undergo inelastic scattering by either transferring energy to or gaining energy from the molecule. Inelastic loss of energy by photons results in Stokes scattering, while inelastic gain of energy leads to anti-Stokes scattering (as depicted in Figure 2.10).

Electromagnetic radiation exhibits characteristics of both particles and waves. Therefore, Raman scattering can be described from two perspectives: the classical interpretation based on wave theory and the quantum interpretation based on electromagnetic radiation as energetic particles[87].

2.2.1 Classical Description

In the classical interpretation of light scattering, it is assumed that a molecule behaves as a vibrating dipole. When the molecule is subjected to an electric field, the electrons and nuclei within it experience displacements, resulting in the development of an electric dipole moment[88]. This induced dipole moment is directly proportional to the applied electric field,

$$\mu = \alpha E \tag{2.1}$$

as represented by Equation 2.1 The polarizability of the molecule, denoted by 'a,' quantifies how easily the molecular orbitals can deform in response to an external electric field.

The electric field (E) can be expressed as:

$$E = E_0 \cos(2\pi\nu_0 t) \tag{2.2}$$

where E_0 represents the amplitude of the electric component, ν_0 is the frequency of the wave, and t denotes time. By substituting Equation 2.1 into Equation 2.2,

$$\mu = \alpha E_0 \cos(2\pi\nu_0 t) \tag{2.3}$$

we obtain Equation 2.3, indicating that the induced dipole moment varies based on the wave frequency. As a result, the molecule becomes a source of radiation at that specific frequency, leading to Rayleigh scattering, which would be the sole form of scattering if the molecule lacked its own internal vibrations.

During vibration, the molecule undergoes changes in size, shape, and consequently, its polarizability (as represented by the polarizability ellipsoid). If the polarizability varies throughout the vibration, every component of the polarizability tensor (α_{ij}) will be expressed as Equation 2.4,

$$\alpha_{ij} = \left(\alpha_{ij}\right)_0 + \left(\frac{\partial \alpha_{ij}}{\partial Q}\right)_0 Q \tag{2.4}$$

where $\left(\frac{\partial \alpha_{ij}}{\partial Q}\right)_0$ signifies the change in the α_{ij} component during the specific vibration characterized by the normal coordinate Q. The normal coordinate describes the displacement of all the atom nuclei within the molecule from their equilibrium positions, while $\left(\alpha_{ij}\right)_0$ represents the value of α_{ij} at the equilibrium position of the nuclei.

The normal coordinate behaves in a periodic way:

$$Q_v = A_v \cos\left(2\pi v t\right) \tag{2.5}$$

with A_v the amplitude of the of the specific vibration occurring in the molecule. Substituting the previous equations in the matrix form of polarization tensor we get:

$$\alpha = \alpha_0 + \left(\frac{\partial \alpha}{\partial Q}\right)_0 A_v \cos\left(2\pi v t\right) \tag{2.6}$$

By utilizing equation 2.3 we can rephrase the equation that represents the magnitude of the induced moment in a molecule undergoing a vibration with frequency v when interacting with an electromagnetic wave of frequency v_0. Additionally, a trigonometric identity is used to get the following equation.

$$\mu = \alpha_0 E_0 \cos\left(2\pi v_0 t\right) + \frac{1}{2} A_v E_0 \left(\frac{\partial \alpha}{\partial Q}\right)_0 \{\cos[2\pi(v_0 - v)t] \quad (2.7)$$
$$+ \cos[2\pi(v_0 + v)t]$$

Consequently, the vibrating molecule can emit scattered radiation at three distinct frequencies. The first term, with a frequency v_0 that remains unchanged compared to the incident radiation, corresponds to Rayleigh scattering. The second term, with a frequency $(v_0 - v)$, corresponds to Stokes scattering. Lastly, the third term, with a frequency (v0 + v), corresponds to Raman anti-Stokes scattering. Additionally, it is concluded that in Raman scattering it is for the polarizability of the molecule to undergo modifications during the vibration[89].

2.2.2 Quantum Description

Energy particles are commonly referred to as quanta, and when it comes to electromagnetic radiation, they are known as photons[90]. The quantum theory perspective of Raman scattering acknowledges that the energy associated with molecular vibrations is quantized based on the principles defined by Planck's relationship $E_v = hv$, with v being the frequency and h the Planck's constant.

When a photon interacts with a molecule, three phenomena can occur. First, absorption takes place if the energy of the photon matches the energy difference between two stationary energy levels of the molecule. Second, emission occurs when the excited molecule releases a photon, and the energy of the emitted photon corresponds to the energy difference between two energy levels of the molecule. Finally, scattering happens when the photon energy does not correspond to any energy difference between two levels of the molecule.
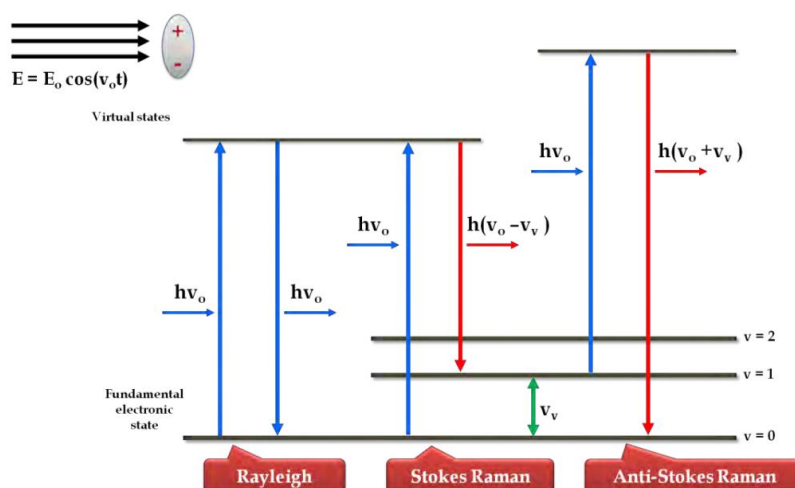
Figure 2.10 Diagram of scattering during illumination of the sample with monochromatic light (v: vibrational levels).

Scattering is a two-photon process and cannot be separated into individual steps of absorption and emission. When identical molecules are exposed to monochromatic light, three types of scattering are observed, as they are described in Figure 2.10. Rayleigh scattering occurs when transitions start and end at the same vibrational energy level. Stokes Raman scattering involves transitions starting from the ground state vibrational level and ending at consecutive higher vibrational energy levels. Conversely, anti-Stokes Raman scattering involves transitions from higher to lower vibrational levels.

The frequency differences between the incident photon and the inelastically scattered photons are equal to the molecular vibration frequency. These phenomena occur almost instantaneously, within a very short timeframe of about 10^{-14} seconds.

2.2.3 Raman Spectrum

In Raman spectroscopy, the energy of the scattered photons is characterized using wavenumbers in cm^{-1}. The Raman shift, which represents the energy difference between the incident radiation and the scattered radiation, is used to describe the Raman signals. The Raman shift can be calculated using the equation:

$$\Delta E = \left(\frac{1}{\lambda_{in}}\right) - \left(\frac{1}{\lambda_{sc}}\right) \tag{2.8}$$

The Raman vibrational fingerprint can be divided into approximate regions. The 0 to 500 cm^{-1} range predominantly includes vibrations involving heavy atoms. The range from 500 to 1800 cm^{-1} is of interest for biological systems, while the 1800 to 2800 cm^{-1} range mainly involves alkyne vibrations and fewer vibrations and overtones. In the range of 2800 to 3500 cm^{-1}, lighter molecules like CH_2 can be detected.

When characterizing a Raman spectrum, several factors should be considered. The peak position depends on the environment and energy level of the vibrating molecules. The full width at half maximum (FWHM) provides information about the dynamics and motion of the molecule. The Raman intensity is influenced by various factors such as the number of molecules and the intensity and wavelength of the laser. To compare peaks between different spectra, the "relative intensity" is often used instead of the "absolute intensity." The relative intensity compares the peaks within the same spectrum rather than relying on the actual intensity counts.

In non-conventional Raman techniques, a strong Raman background may be present, which depends on the specific technique and sample used. Background correction methods vary, and sometimes the background contains valuable information and is not subtracted. Further details on the Raman background can be found in the article by Pilz and Kriegsmann.

Conventional Raman techniques may struggle to detect the Raman signal from low amounts of adsorbed molecules, such as (sub)-monolayers. To enhance the Raman signal, techniques have been developed based on the electromagnetic enhancement of localized surface plasmons, which will be discussed in the next chapter.

2.2.4 Measurement Set-Up
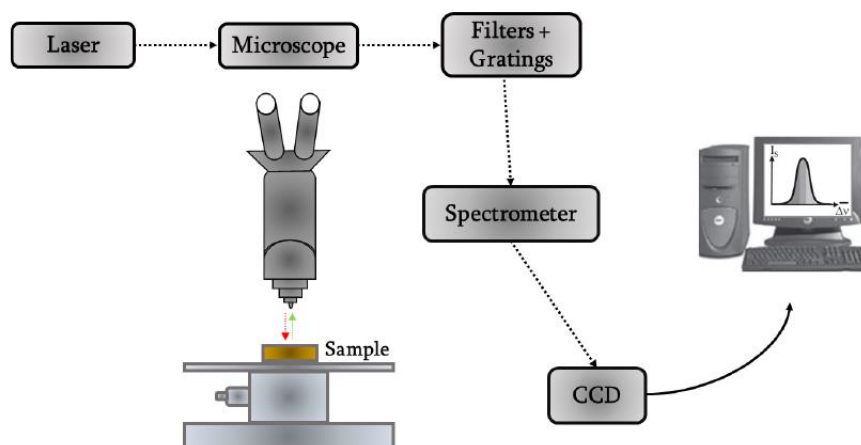
Figure 2.11 Illustration of Raman instrument assembly.

The basic configuration of a Raman spectrometer consists of three main components: a radiation source, typically a laser with a specific wavelength; a spectrometer that disperses the scattered light; and a detector that captures the scattered light. The choice of laser wavelength depends on the intended application, ranging from UV to visible and near-infrared. Commonly used lasers include the 514.5 nm Ar^+ ion laser, the 532 nm Nd:YAG laser, and the 785 nm laser, which offers a good balance between scattering efficiency, fluorescence influence, and detector efficiency. The longer the laser wavelength, the greater the laser intensity that can be used. Figure 2.11 illustrates the overall setup and principle of a Raman microscope spectrometer, where the laser beam interacts with the sample, and the scattered light passes through a filter to select the Raman scattering light of different wavelengths. The dispersed light is then captured by a CCD detector, which converts the photo current into an electric current to generate the spectrum.

A Raman spectrum contains valuable information, with two main parameters influencing its characteristics. Parameters related to vibration-induced charge transfers determine the Raman scattering intensity, while parameters associated with bond "dynamics" determine the peak positions. Peak position serving as a unique "fingerprint" for each molecule or material. The bandwidth indicates the order of the bonds, while shifts in peak positions can be attributed to external perturbations.

2.2.5 SERS Enhancement Factor Calculation

Another critical parameter that defined the Enhancement Factor (EF) on SERS is Raman Spot. In other words, the area that the lens is taking a measurement from. In our case, we used 10x lens with Numerical Aperture (NA) of 0.25 and the Raman spot radius calculated from eq. is 1.9μm. So for a circular area we conclude that **A$_{Raman}$= 11.3μm ^{2}**.

$$R_{Raman} = \frac{1.22\lambda}{2NA} \tag{2.9}$$

Additionally, the depth that Raman can reach in a sample is given by (2.10) and is estimated to be **D$_{Raman}$=4.3μm**.

$$D_{Raman} = \frac{1.4\lambda}{NA} \tag{2.10}$$

Calculation of the enhancement factor[91]:

$$EF = \left(\frac{I_{SERS}}{N_{SERS}}\right) / \left(\frac{I_{Bulk}}{N_{Bulk}}\right) \tag{2.11}$$

the term I_{sers} refers to the Raman scattering intensities observed from the Raman reporter molecules attached to the nanoparticle films. On the other hand, I_{bulk} represents the Raman intensities obtained from the powdered form of Raman Reporters. The variable N_{bulk} represents the average number of probe molecules present in the bulk solid sample (Equation 2.12), while $Nsers$ represents the average number of probe molecules that are bonded to the surface of the nanoparticle film (Equation 2.13).

$$N_{BULK} = \frac{A_{Raman}\,\rho h\,N_A}{M_r} \tag{2.12}$$

M$_r$ is the molecular weight (for 4-MBA is 154.19 g/mol), ρ is the Raman reporter density (for 4-MBA 1.405 g/cm^3), N$_A$ is the Avogadro Number, h the Raman depth and A$_{Raman}$ the spot Raman takes data from per measurement.

$$N_{SERS} = \frac{A_{Raman}\,VM}{A_{Film}N_A} \tag{2.13}$$

With V we refer to the Volume of the organic molecule that was dropcasted in the nanofilm, M is the Molarity and A$_{Film}$ the nanofilm full area (3.24 cm^2).

2.2.6 Experimental Set-Up

Raman spectroscopy measurements were taken using a Horiba XploRA Plus Raman microscope coupled to an Olympus BX41 microscope and using a 785 nm laser as an excitation source. The microscope is coupled to a CCD which helped using low laser intensities of 1% in samples that were experiencing phase changes due to heating. Spectrum were recorded and processed with Lab Spec software. An important parameter is that in all measurements the 10x lens was used.
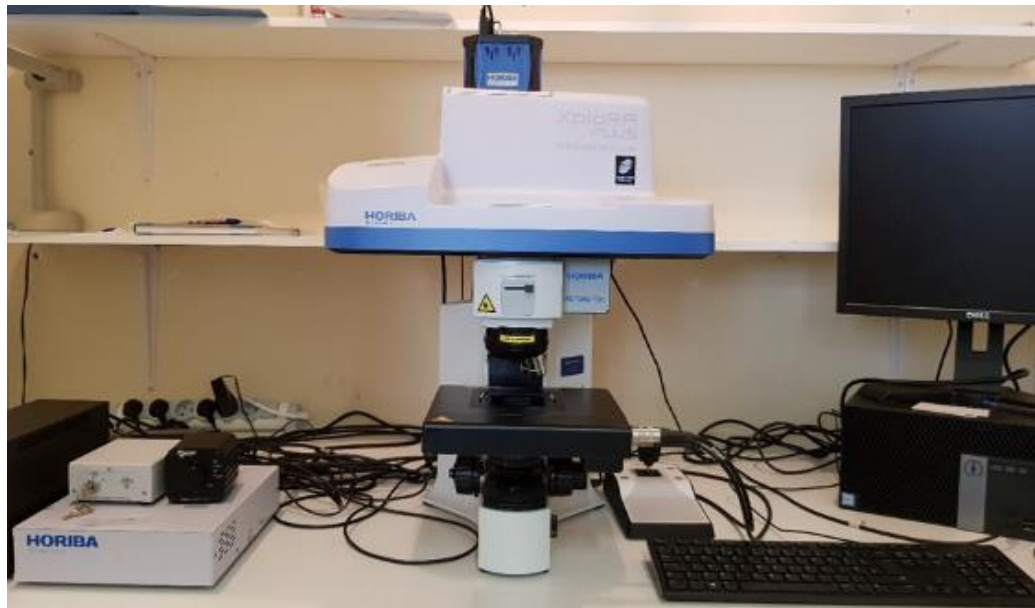
Figure 2.12 Horiba XploRA PLUS Raman microscope.

2.3   X-Ray Diffraction

X-ray powder diffraction (XRD) is a fundamental technique in materials characterization, used to determine the crystal structure of powdered samples. By exposing the sample to X-ray radiation, the XRD technique generates a diffraction pattern that contains valuable information about the arrangement of atoms in the material. Through careful analysis of the diffraction pattern, it can be determined crystal symmetry, lattice parameters, phase composition, and the presence of defects or impurities. XRD is widely employed in fields like materials science, chemistry, geology, and pharmaceuticals, enabling a deep understanding of the structural

properties and behavior of diverse materials, crucial for various applications and research advancements.

2.3.1 Basic Principles

The above technique has it foundations in some basic principles[92]. First and foremost, X-rays, are just like other electromagnetic waves, exhibit both wave and particle properties. X-rays can be treated as a stream of photons, which have energy proportional to their frequency. The wave nature of X-rays enables them to undergo diffraction when they interact with a crystalline solid. When X-rays encounter a crystal, they interact with the atomic planes and experience constructive and destructive interference. This phenomenon is known as diffraction. The regular arrangement of atoms in a crystal lattice acts as a three-dimensional diffraction grating, causing X-rays to scatter in specific directions according to Bragg's law, formulated by Sir William Henry Bragg and his son Sir William Lawrence Bragg in 1913, relates the angles at which constructive interference occurs to the wavelength of X-rays and the spacing between atomic planes in a crystal . Mathematically, it is expressed as

$$n\lambda = 2d \ \sin\theta \qquad\qquad (2.14)$$

where n is the order of diffraction, λ is the wavelength of X-rays, d is the interplanar spacing, and θ is the angle of incidence.

Finally, the interaction of X-rays with a crystal produces a diffraction pattern consisting of a series of bright spots on a detector. Each spot corresponds to a specific set of crystal planes that satisfy the conditions of Bragg's law. By measuring the angles and intensities of these spots, valuable information about the crystal structure can be obtained.
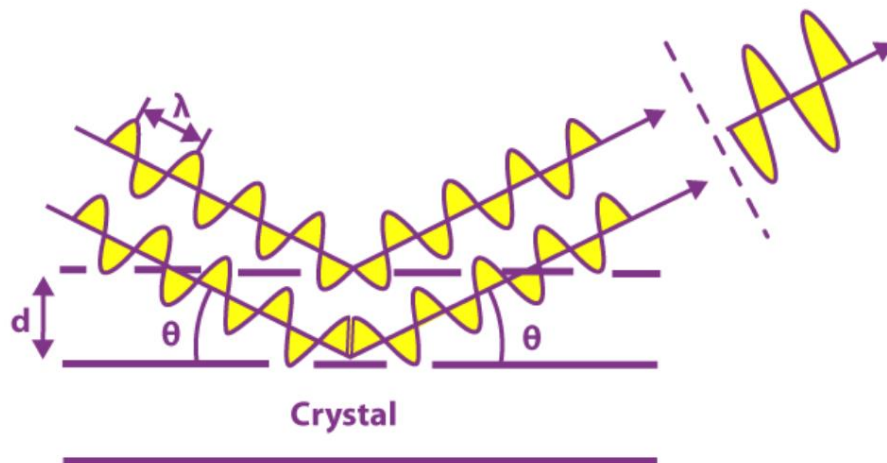
Figure 2.13 Illustration of Braggs Law.

2.3.2 Scherrer Equation

The Bragg peaks present in X-ray diffraction patterns hold valuable information about the material being studied, including phase identification, crystallinity, and size broadening effects. The width of a Bragg peak is associated with the size of the particles within the sample. The relationship between the size of sub-micrometer particles and the broadening of the peaks is described by the Scherrer equation. This equation provides a mathematical expression for estimating the particle size based on the observed broadening of the peaks. The equation nn has the following form:

$$d_{XRD} = \frac{K \lambda}{\beta \cos \theta} \qquad (2.15)$$

the parameter "d" represents the average crystal size of the sample, a dimensionless constant "K" (typically 0.9) and the width of the Bragg peak at half of its maximum intensity (FWHM) expressed in radians as "β," is used to estimate the crystal size. It should be noted that the Scherrer equation is applicable primarily to nanoscale particles and has limitations. It is not suitable for analyzing grains larger than approximately 0.1 micrometers, as the accuracy of the equation diminishes. This is due to the fact that crystal lattice imperfections and strains contribute to the broadening of the FWHM.

2.3.3 Experimental Set-Up

XRD Diffraction Patterns of the nanofilms were obtained with a D8 Advance Bruker Diffractometer (Fig. 2.4) using (40kV, 40mA) λ=0.154 nm Cu Kα radiation with a Lynxeye detector. The sample is placed in a silicon holder. All the parameters,

Figure 2.14 D8 Advance Bruker Diffractometer

including angles wide, angle step, residence time of sample holder, are defined by a Bruker software.

2.4 Ultraviolet-Visible Spectroscopy

UV-Vis spectroscopy is a powerful analytical technique widely employed in various scientific fields, including chemistry, materials science, and physics. It involves the measurement of the absorption or transmission of ultraviolet (UV) and visible (Vis) light by a sample, providing valuable information about its electronic structure and molecular composition. UV-Vis spectroscopy offers insights into fundamental properties such as electronic transitions, concentration analysis, and kinetics of reactions. By analyzing the absorption spectrum it can be identified the functional groups, determine compound purity, and quantify analyte concentrations in a non-destructive way.

2.4.1 Basic Principles

UV-Vis spectroscopy is based on the fundamental principles of the interaction of light with matter[93]. When a sample is subjected to ultraviolet (UV) and visible (Vis)

light, it absorbs photons of specific energies corresponding to electronic transitions within its molecular structure. UV-Vis spectrophotometry concerns the UV range covering of 200–380 nm and the VIS range covering 380–770 nm.

Typically, in the UV-Vis spectra, the electrons involved in absorbing photons are π-electrons or non-bonding (n) electrons in molecules. When these electrons absorb energy from photons, they transition to higher energy anti-bonding orbitals. In the case of semiconductors, if the energy of the incident photons is comparable to the bandgap energy, the light will be absorbed, resulting in the observation of a peak in the spectrum. The bandgap energy represents the energy difference between the valence band (lower energy) and the conduction band (higher energy) in semiconductors. When photons with energies matching the bandgap are absorbed, electrons in the valence band are excited to the conduction band, contributing to the observed absorption peak.

The absorption of light by the sample is governed by two basic principles. Firstly, the Beer-Lambert Law[94], which states that the absorbance (A) is directly proportional to the concentration (c) of the absorbing species and the path length (l) through which the light travels. Mathematically, it can be expressed as:

$$A = \varepsilon cl \tag{2.16}$$

where ε is the molar absorptivity or extinction coefficient.

Secondly, Lambert's Law establishes that the absorption of incident light by a transparent medium is unaffected by the light's intensity. As a result, consecutive layers of uniform thickness will transmit an equal proportion of the initial energy. This principle can be expressed through the following equation:

$$\% \, T = \frac{I}{I_0} \times 100 \tag{2.17}$$

where I represents the intensity of the transmitted light, I_0 signifies the intensity of the incident light, and T denotes the transmittance. It is customary to express transmittance as a percentage relative to the incident light.

Combining the above, we finally conclude in the equation that has the form:

$$A = \log \frac{I}{I_0} = -\log \left(\frac{\% T}{100\%} \right) = \varepsilon C \ell \tag{2.18}$$

where A is the absorbance, which is unitless, ε is the molar attenuation coefficient of the medium ($M^{-1} cm^{-1}$), C is the molar concentration (M), and l is the pathlength (cm). It is important to note that the molar attenuation coefficient is a function of wavelength, therefore Beer-Lambert's law is only true at a single wavelength.

The absorption spectrum obtained from UV-Vis spectroscopy provides information about the energy levels and electronic transitions within the sample. It typically consists of a plot of absorbance versus wavelength or frequency, showing characteristic peaks and valleys.

2.4.2 Experimental Set-Up

The PerkinElmer Lambda 35 Spectrometer (Figure 2.15) was used to collect UV-Vis spectra. The particles were dispersed in aqueous solvents and placed in quartz cuvettes.. The monochromator employed a holographic grating and the optical system is illustrated schematically in Figure 2.17.

The holographic concave grating in the monochromator had 1053 lines/mm at its center. The spectrometer utilized two radiation sources, namely a deuterium lamp and a halogen lamp, which covered the desired wavelength range. The two lamps used in the setup emit light at 380nm, which introduces

Figure 2.15 PerkinElmer Lambda 35

background noise into the spectra in the neighboring wavelengths. The combination of mirrors and filters (in the system ensures that only a monochromatic beam of photons is directed towards the sample surface. By measuring the intensity difference between the incident light produced by the lamps and the reflected light detected by the detector, a spectrum is generated.

For UV-Vis experiments, rectangular quartz-glass cuvettes with a fixed width of 1cm are commonly used. The light passes through the material along this path. The cuvettes

are made of quartz glass because it is transparent in the UV to near-infrared range, ensuring that the container itself does not contribute to the signal.
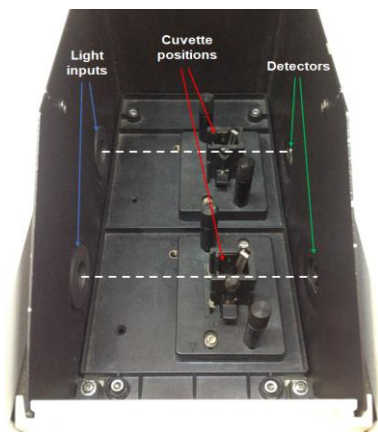
Figure 2.16 Top view of UV/Vis holder

In our experiment we use a double beam UV/Vis, meaning that one beam has to pass through the reference sample, while simultaneously the other beam has to pass the material in question. The beam that passes the reference is considered the I0 of the system.

In this particular experiment, ethanol will serve as the reference sample. The sample, on the other hand, will consist of a fixed concentration of ethanol, and the nanoparticles.
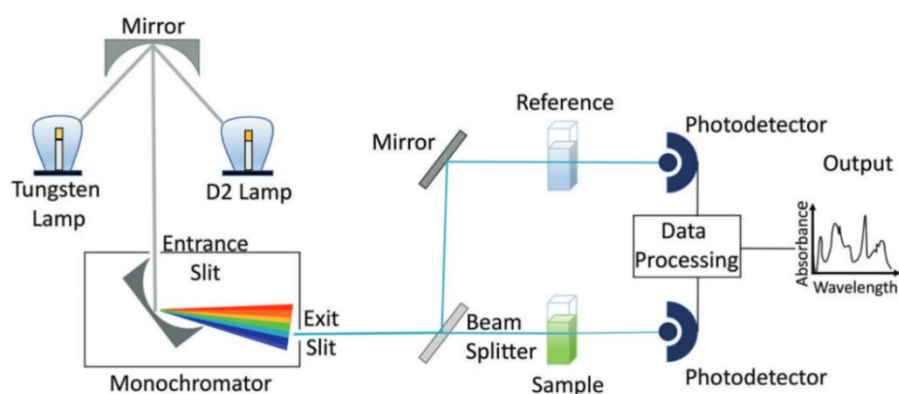
Figure 2.17 Schematic view of optical path for PerkinElmer Lambda 35 Spectrophotometer.

2.5   Light Irradiance Set-up

Studying the Photo-Induced Enhanced Raman Spectroscopy (PIERS) a UV light source was needed in order to create the oxygen vacancies in the semiconductor.

In our case we used the experimental set-up demonstrated in FI and consisted of an Arc Xenon Lamp (model: Oriel 6293, 1000 W) that radiates through a pipe, and a beam turning mirror holder (Figure 2.18) which bends the beam by 90 degrees, absorbing most of the radiation.

Figure 2.19 Oriel Lamp irradiance spectrum

For our experiments, we will adjust the power of the arc xenon lamp to 450 W. The lamp's male flange end is compatible with the output of an Oriel Lamp Housing condenser (as shown in Figure 3.32a). The majority of infrared (IR) light passes through the dichroic mirror, while the mirror housing absorbs it and a heat sink dissipates the generated heat. The optimal distance between the lamp's surface and the lens is approximately 0.5 m. In Figure 2.19, the spectral irradiance of the lamp is displayed with the wavelength (λ) as the spectral variable. By integrating the area from 390 to 700 nm, the total irradiance within the visible spectrum can be determined in units of W/m².

Figure 2.18 Experimental illumination set-up,, consisting of the arc xenon lamp and the beam turning mirror holder.

2.6   **Spin Coater**

In order to disperse the solution of the organic raman reporter in the nano-film we used the 6800 Spin Coater by Speciality Coating Systems. The film was placed in a special holder and stayed in its place while spinning due to the air pump that was connected to the set-up. All the parameters were set by a software of SCS, in our

Figure 2.20 Spin Coater 6800

experiment we used maximum of 2000rpm in all samples.

Chapter 3

Results - Discussion

3.1   Substrate Synthesis

In this Chapter taking advantage of the Flame Spray Pyrolysis technique that was described in Chapter 2, we manage to synthesize the Plasmonic Nanofilms that will be analyzed in the sections that will follow. For the purpose of this master thesis two king of substrates were synthesized, $AgSiO_2$ and $AgTiO_2$. The FSP set-up that was used, as it is already analyzed, is the one with the water cooled film holder. Since the films are for one use only, totally 80 nanofilms were made but the ones with different variables in the fabrication process will be analyzed and characterized.
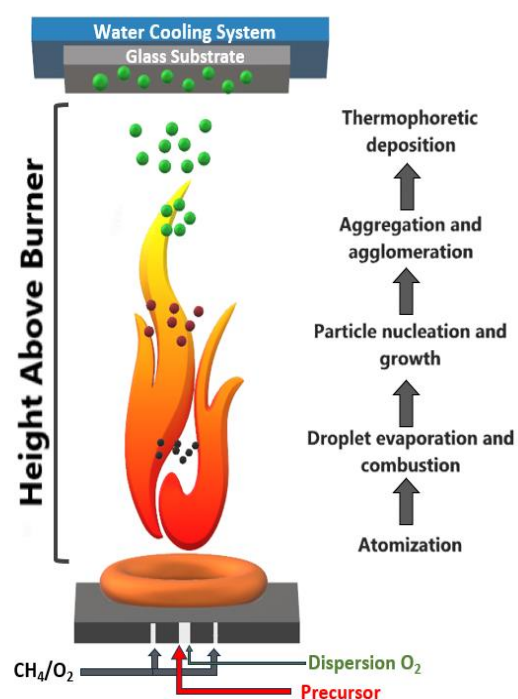
Figure 3.1: *Schematic diagram of the experimental procedure to fabricate SERS sensing films in one-step.*

3.1.1 AgSiO₂ Synthesis

Firstly, in Table 3.1 are presented the FSP parameters of the $AgSiO_2$ nanofilms. The precursor solution was prepared by dissolving silver acetate (Sigma-Aldrich, purity > 99%) and Hexamethyldisiloxane (HMDSO, Aldrich, purity 98%) in 2-ethylhexanoic acid (EHA) and acetonitrile (ACN) (both Sigma-Aldrich, purity > 97%), at volume ratio 1:1.

FSP Parameter	
Precursor	Silver Acetate/ HMDSO
Solvents	2-Ethylhexanoic acid/ Acetonitrile
Precursor Feed rate (mL min^{-1}) / Dispersion (L min^{-1})	5/5
Pilot Flame O2/CH4 (L min^{-1})	3/1.5
Seath O$_2$(L min^{-1})	15
Molarity (M)	0.4
Pressure (barr)	1.8
Hight From Burner (HAB) (cm)	25 cm
Substrate Temperature (ºC)	60

Table 3.1: FSP parameters for AgSiO$_2$ substrate fabrication.

The quantity of HMDSO in the mixture of the liquid precursors defined the wt% content of SiO$_2$ in the final product, in other words it influences the average distance that the silver particles have between them and acts as dielectric spacer.

In this study we fabricated Ag@SiO$_2$ substrates with 6%, 10% and 20% of SiO$_2$ wt%. The next important parameter that defines the thickness of the film is the deposition time (t_d) of the nanoparticles in the glass substrates. Three deposition times were followed, 100s, 60s and 40s.

Deposited nanoparticle mass increased linearly with t_d but the glass substrate had a brake limit around 120s for HAB 25cm. On the other hand, $t_d<40s$ was under the limit for sufficient quantity of deposited nanoparticles on the substrate. For $t_d = 100s$ the average mass of the deposited nanoparticles is 0.95mg, for 60s is 0.55mg and for 40s is 0.35mg. The film samples that will be characterized on behalf of Ag@SiO$_2$ substrates are summarized in Table 3.2.

Additionally, a sample was prepared without the addition of HMDSO resulting in a substrate of Ag NPs.

3.1.1 AgSiO2 Synthesis
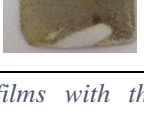
Sample Number	SiO$_2$ wt%	Deposition Time (s)	Mass (mg)	Picture
Film 46	6	100	0.95	
Film 47	6	60	0.52	
Film 48	6	40	0.34	
Film 49	10	100	0.91	
Film 50	10	60	0.55	
Film 51	10	40	0.31	
Film 52	20	100	0.95	
Film 53	20	60	0.53	
Film 54	20	40	0.32	
Film 58	0	100	0.85	

Table 3.2: List of FSP experimental parameters for all synthesized nanofilms with the corresponding pictures.

.

3.1.2 AgTiO$_2$ Synthesis

Ag/TiO2 nanofilms have been prepared by flame spray pyrolysis using a single nozzle configuration shown in Figure @@. Precursor molarity, precursor fuel feed rate to dispersion gas rate (P/D ratio) and the hight from burner distance was adjusted accordingly and are presented in the Table 3@@. Specifically, titanium iso-propoxide (TTIP, Sigma Aldrich) and silver acetate (sigma aldrich, >99%) were dissolved in ethylhexanoic acid/acetonitrile (1:1). A O2/CH4 premixed gas (3.2/1.5 L min-1, Linde >99.9%) provided the supporting flame and the initial ignition.

Two kinds of nanofilm batches were constructed, one with TTIP of molarity 0.6M and another one of 0.3M. In both cases Ag content was 50% wt. Three deposition times were followed 100s, 60s and 40s, giving accordingly nanofilms with mass of 0.95mg , 0.5mg and 0.32mg.

FSP Parameter	
Precursors	Silver Acetate/ Titanium(IV) isopropoxide
Solvents	2-Ethylhexanoic acid/ Acetonitrile
Precursor Feed rate (mL min^{-1}) / Dispersion (L min^{-1})	7/5
Pilot Flame O2/CH4 (L min^{-1})	3.5/1.5
Seath O$_2$(L min^{-1})	15
Molarity (M)	0.3/0.6
Ag Content wt %	50
Pressure (barr)	1.8
Hight From Burner (HAB) (cm)	25 cm
Substrate Temperature (ºC)	60

Table 3.3: FSP parameters for AgTiO$_2$ substrate fabrication

Additionally, we fabricated a film with sequential deposition, meaning that the Ag precursor was fed to the flame after the already formed, the molarity of TTIP precursor was 0.6M and then deposited the Silver nanoparticles. The Ag particles deposition takes place in cooler temperature gradients outside the hotter flame zone. The same

3.1.2 AgTiO2 Synthesis

parameters of FSP were used again in order for the single nozzle substrate and sequential substrate to be compared.
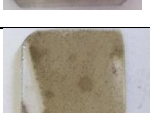
Sample Number	Molarity (M)	Deposition Time (s)	Mass (mg)	Picture
Film 66	0.6	100	0.95	
Film 67	0.6	60	0.52	
Film 68	0.6	40	0.34	
Film 69	0.3	100	0.91	
Film 70	0.3	60	0.55	
Film 71	0.3	40	0.31	
Film 72	0.6	100	0.95	
Film 73	0.6	60	0.55	

Table 3.4: List of FSP experimental parameters for all synthesized nanofilms with the corresponding pictures.

3.2   Substrate Characterization

3.2.1 X-Ray Diffraction Results

X-Ray Diffraction (XRD) was used to study the crystal structure of the Nanosensors. XRD patterns were measured directly from the glass substrate that was placed in a special holder.

In the AgSiO$_2$ substrates the XRD patterns are presented in **Figure 3.2** and **Figure 3.4**.

The XRD peaks at 2-theta of 38.1°, 44.2°, 64.5° and 77.4°, corresponding to (111),
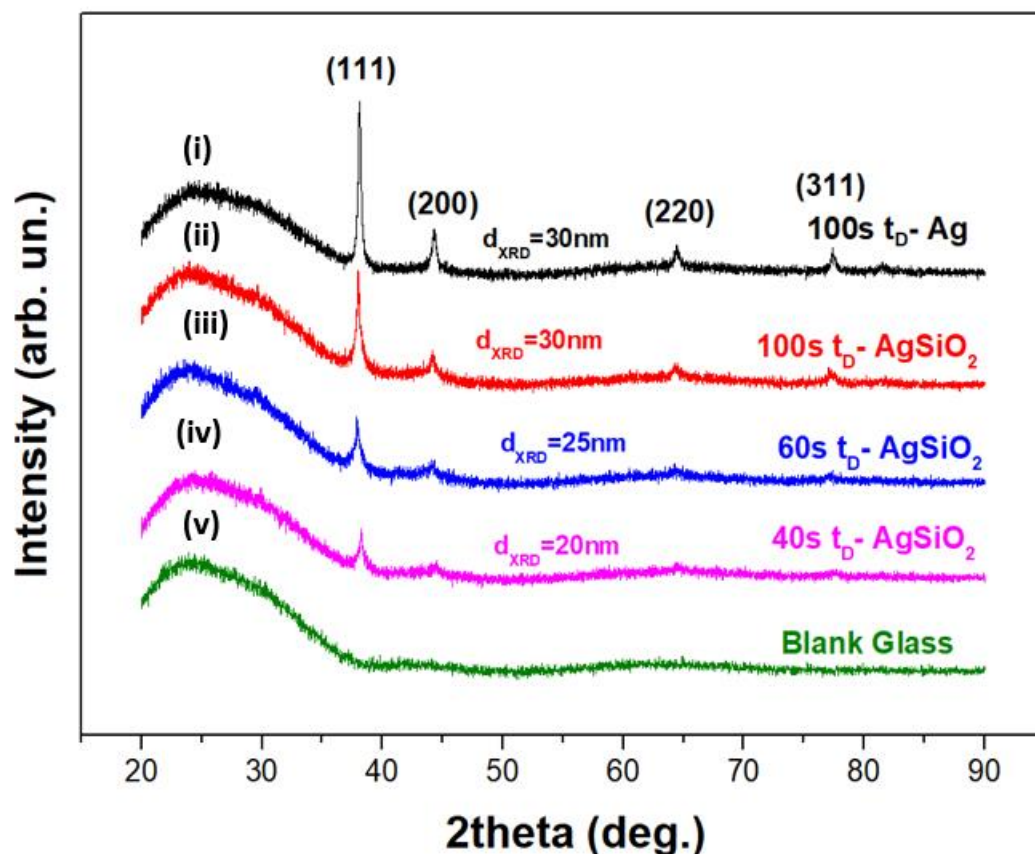
Figure 3.2: XRD patterns of flame-made nanofilms. The black line corresponds to (i) Ag-NPs of 100s t$_D$. The red, blue and purple lines correspond to AgSiO$_2$ 6% wt SiO2 of t$_D$ (ii) 100s (iii) 60s (iv) 40s, and (v)of blank glass.

(200), (220), and (311) crystallographic planes of cubic silver crystals. As the deposition time decreases, so as the thickness of the film, the peaks are less clear and that occurs due to the insufficient quantity of NPs in the film. The broad peak that appears at 2-theta of 24.4° is attributed to the borosilicate composition of the substrate glass.
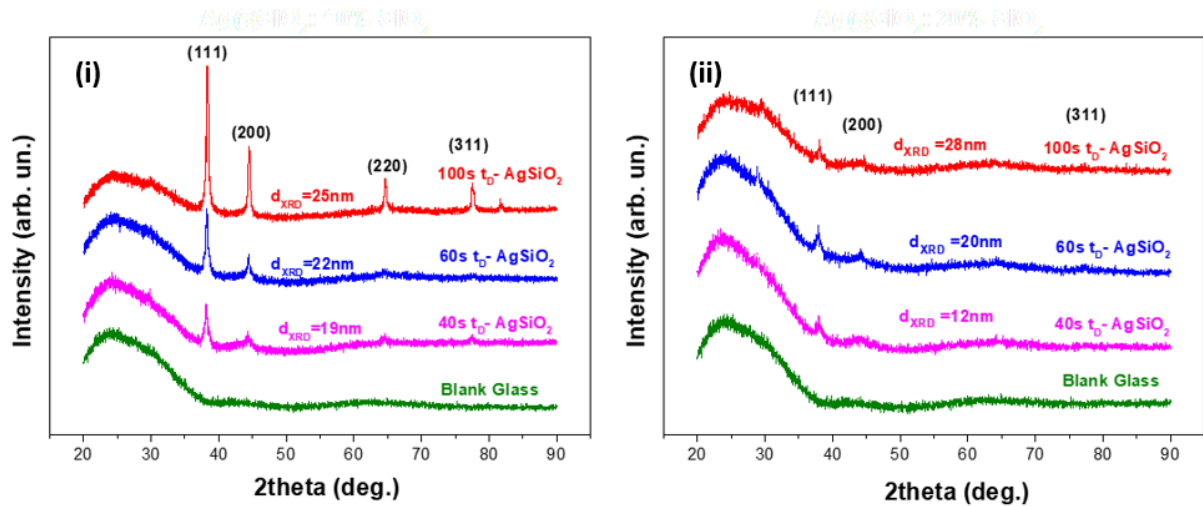
Figure 3.4: *XRD patterns of flame-made nanofilms. The (i) correspond to AgSiO₂ 10% wt SiO₂ with the t_D increasing from bottom to the top, the (ii) corresponds to 20% wt SiO₂ with the t_D increasing from bottom to the top and with green color is the blank glass XRD pattern.*

The size of the NPs in the nanofilms varied depending on the deposition time. The higher the t_d the more growth the NPs can have in the glass substrate . In our case, the AgSiO₂ NPs sizes varied from 30nm to 19nm.
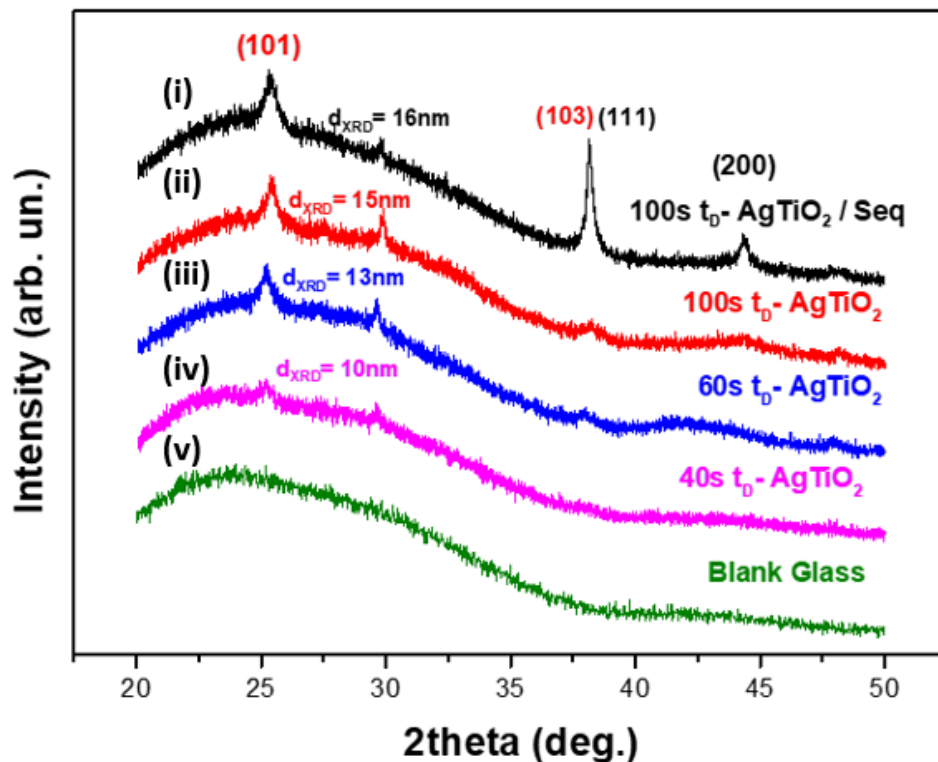

Figure 3.3 *XRD patterns of flame-made nanofilms. The black line corresponds to (i) AgTiO₂ sequential deposition of 100s t_D. The red, blue and purple lines correspond to sungle nozzle AgTiO₂, 0.6M TiO₂ and 50% wt Ag of t_D (ii) 100s (iii) 60s (iv) 40s, and (v)of blank*

3.2.1 X-Ray Diffraction Results

As we increased the SiO$_2$ % the Ag NPs had more distance between them and the XRD peaks don't appear clear enough, especially in 20% SiO$_2$ as shown in **Figure 3.4** (ii).

In the AgTiO$_2$ substrates the XRD paterns are shown in **Figure 3.3** and **Figure 3.5** for TiO$_2$ molarities of 0.6 M and 0.3M respectively. The XRD peak matching to that of anatase is at 2-theta 25.3° corresponding to (101) crystallographic plane, the peak in 38.1° corresponds to (103) crystallographic plane of TiO$_2$ but is convoluted with (101) Ag
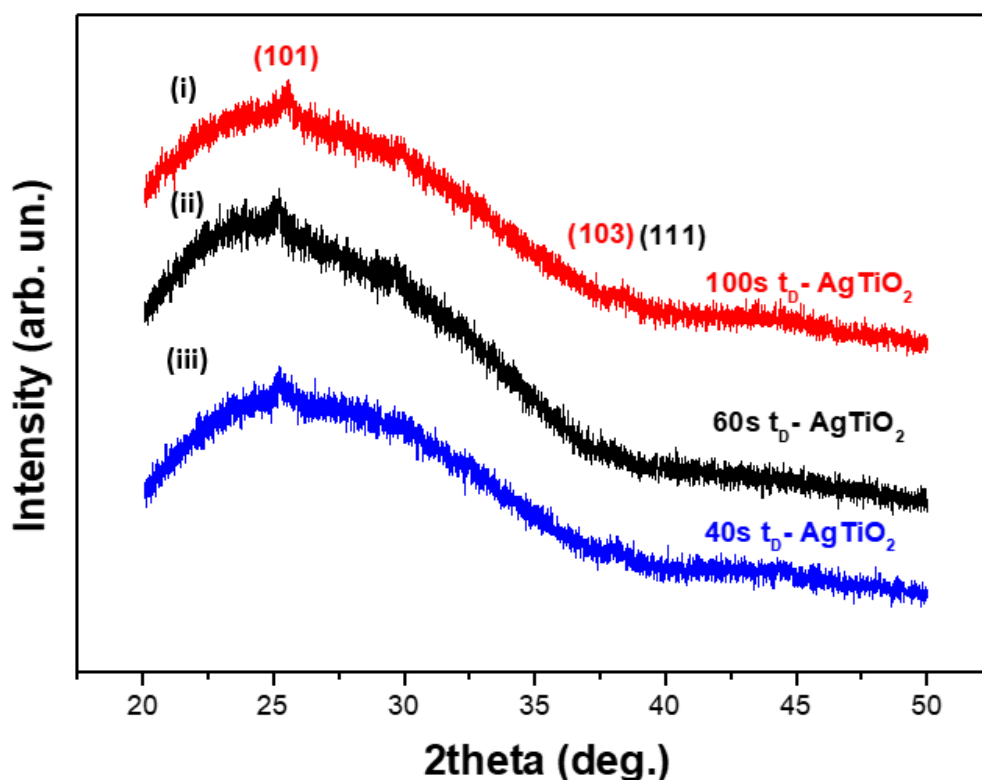
Figure 3.5: Figure 3.6 XRD patterns of flame-made nanofilms. The red, black and blue lines correspond to AgTiO$_2$ 0.3M TiO$_2$ and 50% wt Ag of t$_D$ (i) 100s (ii) 60s (iii) 40s respectively..

diffraction plane. For silver NPs the crystallographic planes (111) and (200) appear again in 38.1° and 44.2° respectively. It is observed that the resolution of the peaks drops as the molarity of TiO$_2$ decreases.

The size of the TiO$_2$ NPs in the 0.6M case fluctuates from 16nm to 10nm (**Figure 3.3**) depending on the deposition time as discussed earlier. Unfortunately, for the molarity of 0.3M the XRD patterns don't have the needed resolution for determining the size of TiO$_2$ through Sherrer equation but in estimation the sizes are smaller and the amorphicuty greater. Also, for the Ag NPs the only case in which the size can be

calculated with XRD is the sequential deposition and is about 28nm, in agreement with the AgSiO$_2$ substrates of t$_d$ 100s.

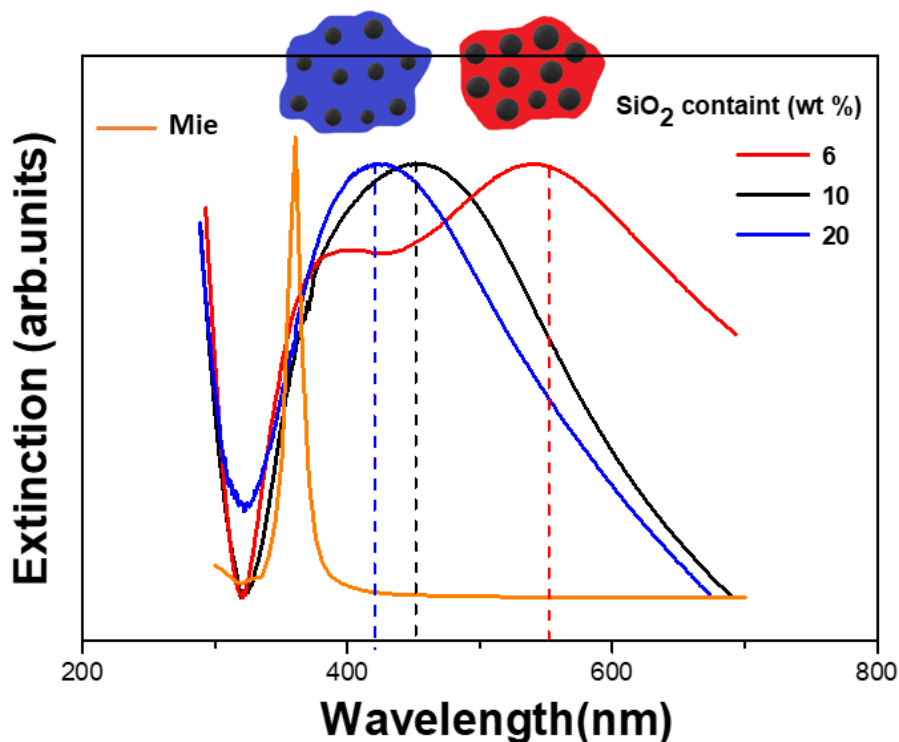## 3.2.2 Ultraviolet-Visible Spectroscopy Results

Figure 3.7: UV-VIS spectra of AgSiO$_2$ of 100s deposition time, with red is the 6% wt SiO$_2$, with black the 10%, with blue the 20% and with orange the theoretical Mie prediction..

The UV-Vis spectra for suspensions of Ag SiO$_2$ nanofilms in ethanol are depicted in **Figure 3.7**.

 While the plasmonic resonance of individual Ag^0 nanoparticles usually takes place at a specific wavelength of 390 nm, the resonance peak for the AgSiO$_2$ 20% wt is red-shifted towards 420nm, due to the increased dielectric presence of the SiO$_2$. The AgSiO$_2$ 10% wt samples had greater shift as the peak was located in 456nm as the distance between the Ag NPs was decreased. In the case of 6% wt SiO$_2$ the plasmonic peak was detected in 543nm that additional enhanced red-shift of LSPR peak was due to plasmonic coupling, where multipolar mode arise. In non-monodisperse ensembles, the multiple LSPR peaks and band broadenings reflect the extent of particle

aggregation. This is conclusively proven for the $AgSiO_2$ 6% samples where a strong plasmonic coupling is detected, allowed by the smollest inteparticle distance beetwen Ag NPs. In contrast, the 20% wt SiO_2 displays a single plasmon resonance, approaching the case of isolated Ag particles, as predicted by Mie theory.

This observation was further confirmed through TEM images of powder samples, as presented in **Figure 3.8**, which revealed the presence of an amorphous nanostructured SiO_2 dielectric spacer. This spacer served to separate the spherical silver nanoparticles within each aggregate and effectively hindered their proximity.

The amorphous SiO_2 performs a dual role:

- maintaining the cohesion of individual silver nanospheres within each nanoaggregate
- functioning as a dielectric spacer to precisely adjust the interparticle distance in a controlled manner.
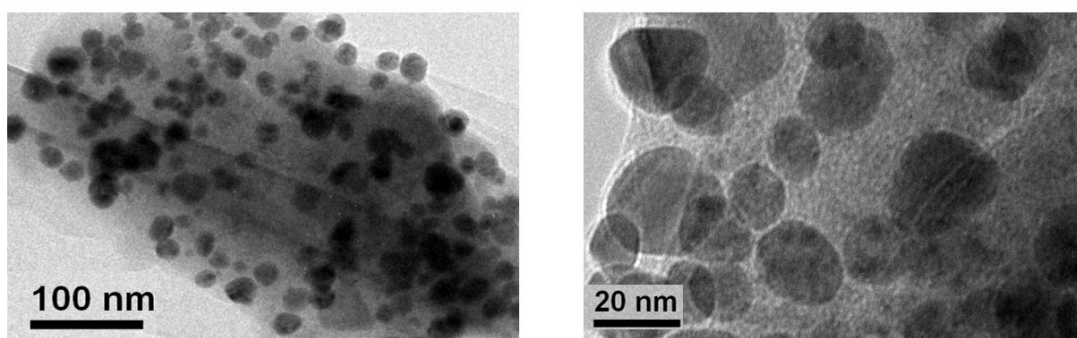
Figure 3.8: *TEM images of single nozzle AgSiO₂ NPs with different wt% SiO₂ containts, left with 20% and right with 6%.*

Additionally, different amounts of SiO_2 content did not result in any noticeable alteration in the size distribution of the colloidal suspensions something that agrees with the XRD size results.
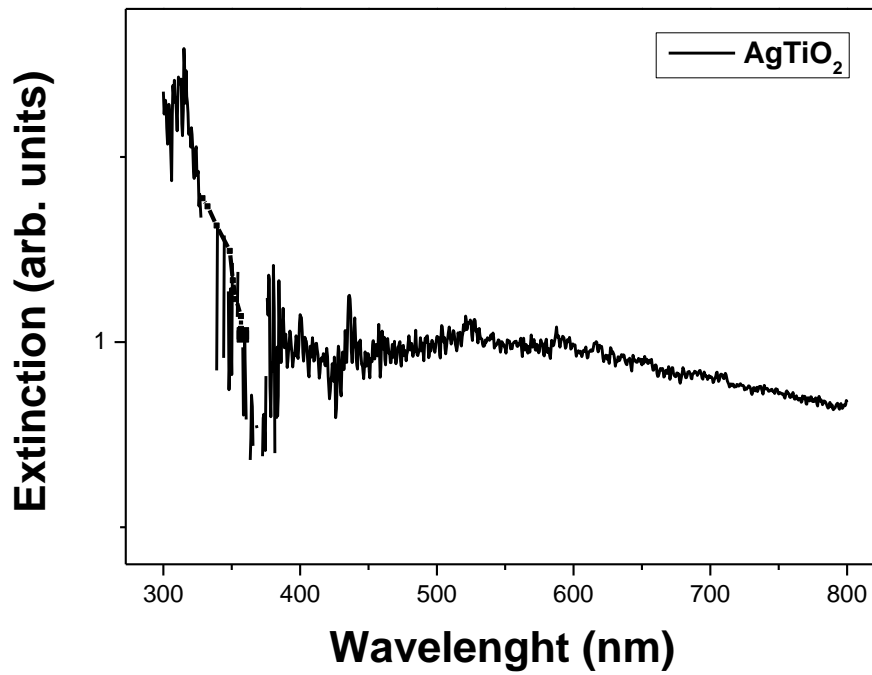
Figure 3.9: *AgTiO$_2$ spectrum of 0.3M and 1000s deposition time.*

For AgTiO$_2$ UV-VIS spectra wasn't supporting us useful information as TiO$_2$ has an 3.2eV bandgap and UV-Vis had a flat like shape (**Figure 3.9:**).

3.2.3 Raman Spectroscopy Results

As far as Raman Measurements are considered, the two kind of substrates were measured without the addition of any SERS probe.

Firstly, the $AgSiO_2$ measurements are shown in **Figure 3.10**. A highly distorted silica formation is observed in the Raman spectrum. A baseline subtraction was needed for further peak identification. Normally, the Raman spectrum of SiO_2

substances exhibit distinctive patterns within the range of 400-600 cm^{-1}. These patterns are associated with various arrangements of the siloxane rings. The 491 cm^{-1} correspond to δ(Si−O−Si) asymmetry. 4MR, 5MR, and 6MR breathing modes[95] . Additional peaks emerge at lower frequencies, approximately below 400 cm^{-1}, and they are attributed to siloxane rings that are larger than four members in size. Additionally, multiple downshifts of peaks are noticed, indicative of less strained lattices and high lattice amorphisity[95], potentially due to incomplete flame combustion or due to the presence of Ag NPs. The 1060 cm^{-1} peak is referring to vibrational mode of ν(Si−O−(Si)) asymmetry of nonbridging O atoms and the 935 cm^{-1} peak is indicating
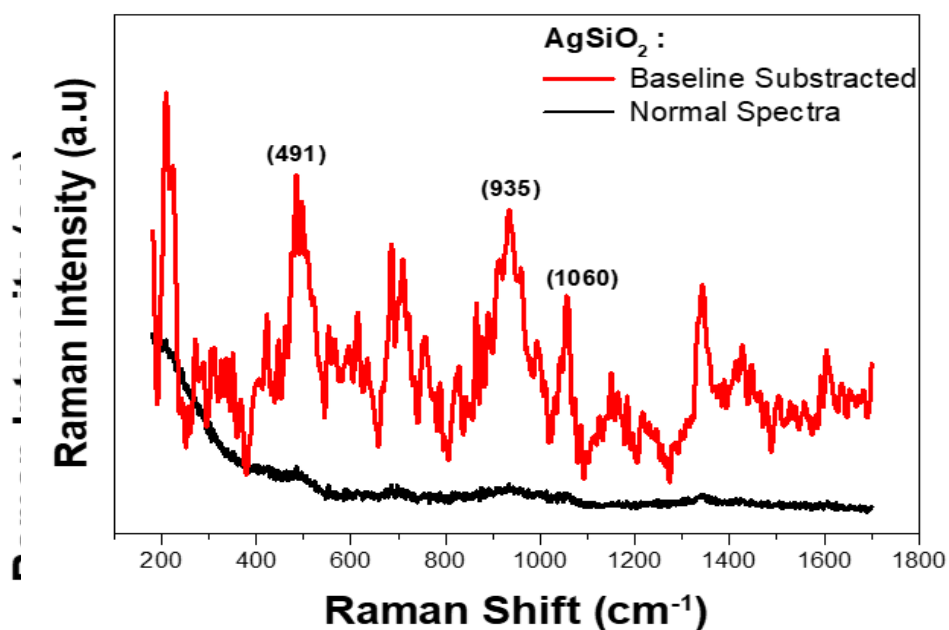

Figure 3.10: AgSiO₂ Raman Spectrum of 10% wt SiO₂ and 100s deposition time. With red color is the Raman spectrum with the baseline subtracted and with black the original spectrum. There is notation in the main Raman peaks.

Figure 3.11: AgTiO₂ Raman Spectrum of 0.6M TiO₂ and 100s deposition time. The main peaks of the vibrational modes are marked.

the isolated ν(Si−O(H)).

Next measurement was taken for AgTiO$_2$ substrate, as shown in **Figure 3.11**. Highly distorted anatase peaks are observed, broadened and shifted, revealing Ti-O bond stretching, indicative of the distorted interface and the presence of suboxide phases[96] Also, β-phase TiO$_2$ is observed in 231 and 272 cm^{-1} peaks[97,98], the identification of this phase is means the TiO$_2$ isn't fully formed something that agrees with the XRD patterns.

Subsequently, Raman measurements were taken for the Raman Reporters that will be used thoroughly in the SERS analysis.

Firstly, the 4-Mercaptobenzoic Acid was mostly used for SERS calibration as it is
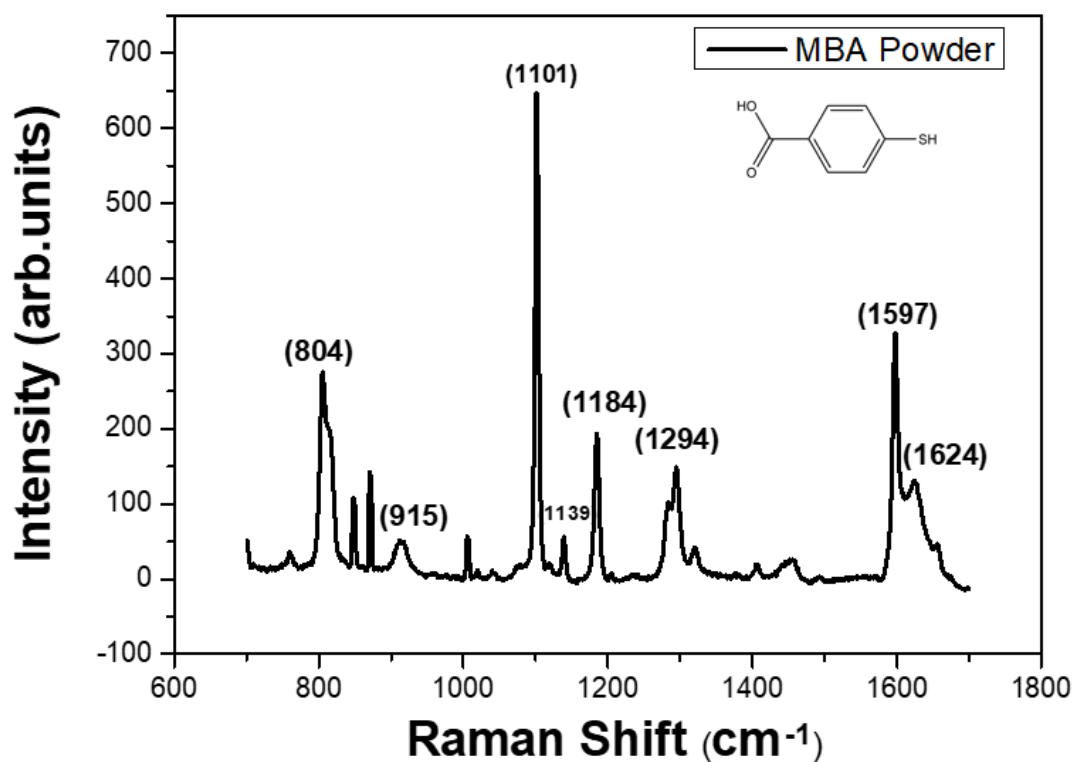
Figure 3.12: 4-Mercaptobenzoic Acid powder Raman Spectrum and its corresponding peaks.

Raman Shift (cm^{-1})	Vibrational modes
804	γ (CCC), out of plane ring vibration
915	bending CS
1101	Aromatic ring breathing
1101	Symmetric C-H in-plane bending
1101	C-S stretching
1139	Stretching g_a
1184	Bending CH
1294	Stretching v_3
1597	Ring C-C stretch
1597	Asymmetric C-H in plane bending
1624	Stretching C=O

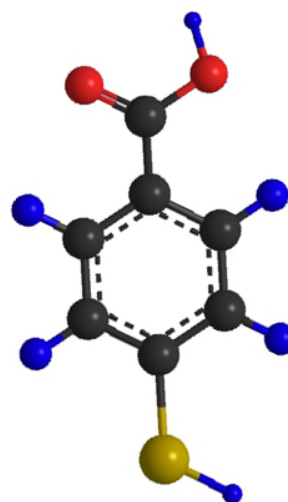*Table 3.5: Raman peaks of 4-MBA with it's corresponding Vibrational modes.*

Figure 3.13: The molecular representation of 4-MBA.

known for its adsorption prowess. With its sulfur-containing aromatic ring, it eagerly binds to various surfaces, Harnessing its remarkable affinity for metals and solid substrates.

4-MBA, as we will refer it from now on, was purchased from Sigma-Aldrich and used without further purification. In **Figure 3.12** the Raman Spectrum of 4-MBA is displayed. There are 3 main peaks[99] are located in (804) cm^{-1}, (1101) cm^{-1} and the (1597) cm^{-1} peak. All vibrational modes are concluded in **Σφάλμα! Το αρχείο π ροέλευσης της αναφοράς δεν βρέθηκε.**.

The other Raman reporter that was used is Rhodamine 6G ,due to its high fluorescent thought it wasn't as practical for SERS as it was the 4-MBA reporter. The R6G, as we will refer it from now on has the Raman spectrum of **Figure 3.14** and the corresponding vibrational modes[100] are summarized in **Table 3.6**. The strong fluorescence is a property that all dyes have and the more benzoic rings contribute to enchantment of the forementioned phenomenon. The structure of R6G is displayed in **Figure 3.15**
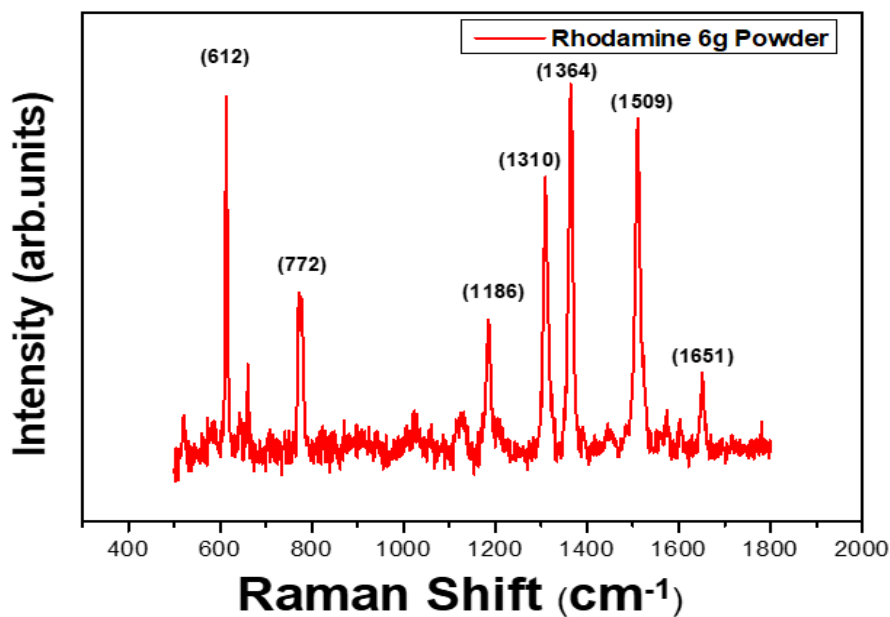
Figure 3.14: Rhodamine 6-G powder Raman Spectrum and its corresponding peaks.

Raman Shift (cm⁻¹)	Vibrational modes
612	C–C ring in-plane bending in xanthene/phenyl rings
772	C–H out-of-plane bending
1186	C–H in-plane bending in xanthene ring
1310	hybrid mode (xanthene/phenyl rings and NHC2H5 group)
1364	C–C stretching in xanthene ring
1509	C–C stretching in xanthene ring
1651	C–C stretching in xanthene ring

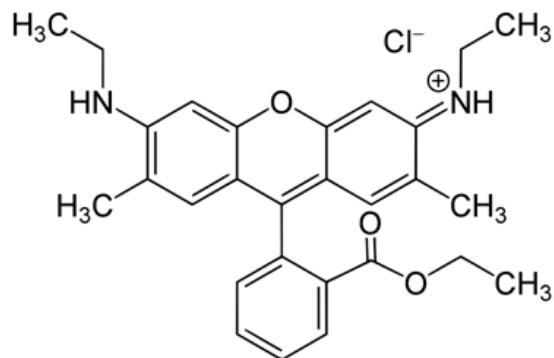*Table 3.6: Raman peaks of R6G with it's corresponding Vibrational modes.*

Figure 3.15: The molecular representation of R6G.

72

3.3   SERS   Results

In this subchapter, the fabricated substrates will be analyzed via Raman Spectroscopy after the addition of the Raman Reporter which in our case is 4-mercaptobenzoic Acid (4-MBA) or Rhodamine 6G (R6G). In all samples the same quantity of the Raman Reporter (150μl) was added, but in different concentrations. In this thesis two kind of substrates were fabricated as already mentioned, $AgSiO_2$ and $AgTiO_2$, further from that other parameters were changed in each nanofilm such as SiO_2 wt%, deposition time and TiO_2 molarity. For notation purposes before the kind of substrate we are referring the other parameters and will be displayed in the

Figure 3.16: *Hot spot illustration between tho Ag NPs via Matlab software.*

following form: 60s-10% $AgSiO_2$, meaning deposition time 60s, SiO_2 wt% 10% of AgSiO2 nanofilm. On the other hand, 40s-0.3M $AgTiO_2$ is interpreted as deposition time 40s, TiO_2 molarity 0.3M of $AgTO_2$ nanofilm. In **Figure 3.16** and **Figure 3.17** hot spot illustration and SERS basic principle is displayed.
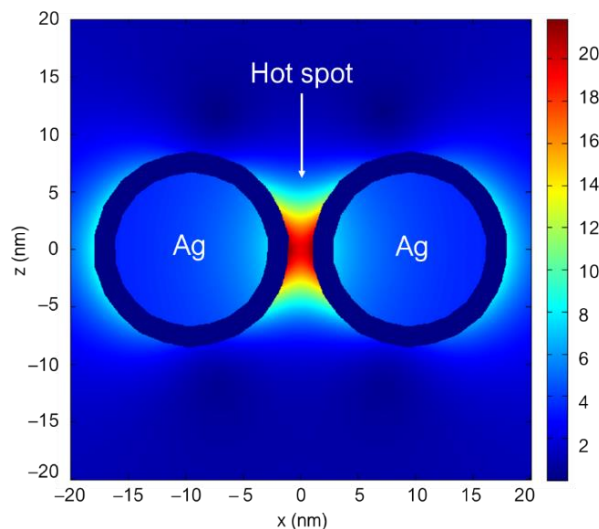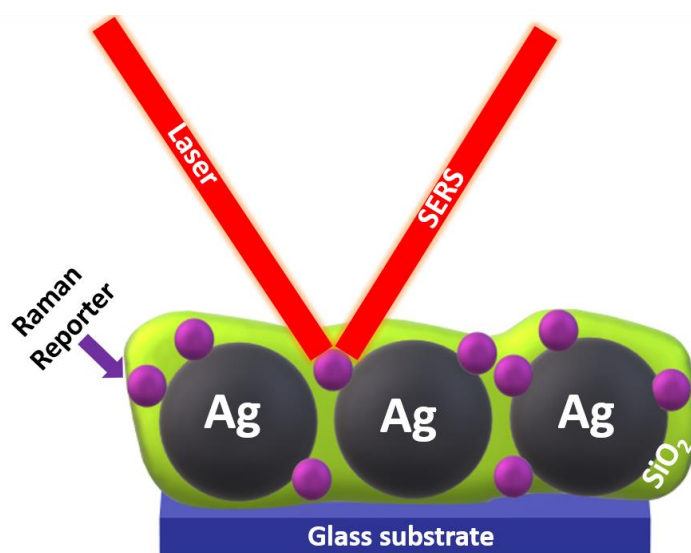

Figure 3.17: *Illustration of SERS mechanism in the $AgSiO_2$ substrate.*

3.2.3 Raman Spectroscopy Results

Before moving on with the separate analysis of each substrate and the goal of finding the optimum nanofilm with the highest SERS Enhancement factor, there will be displayed some general results of SERS that apply in both of the substrates. In **Figure 3.19** the SERS spectrum of 4MBA-AgSiO$_2$ NPs exhibits two strong peaks at 1.075 and 1,582 cm^{-1}. These peaks correspond to the vibrations of the aromatic ring in the
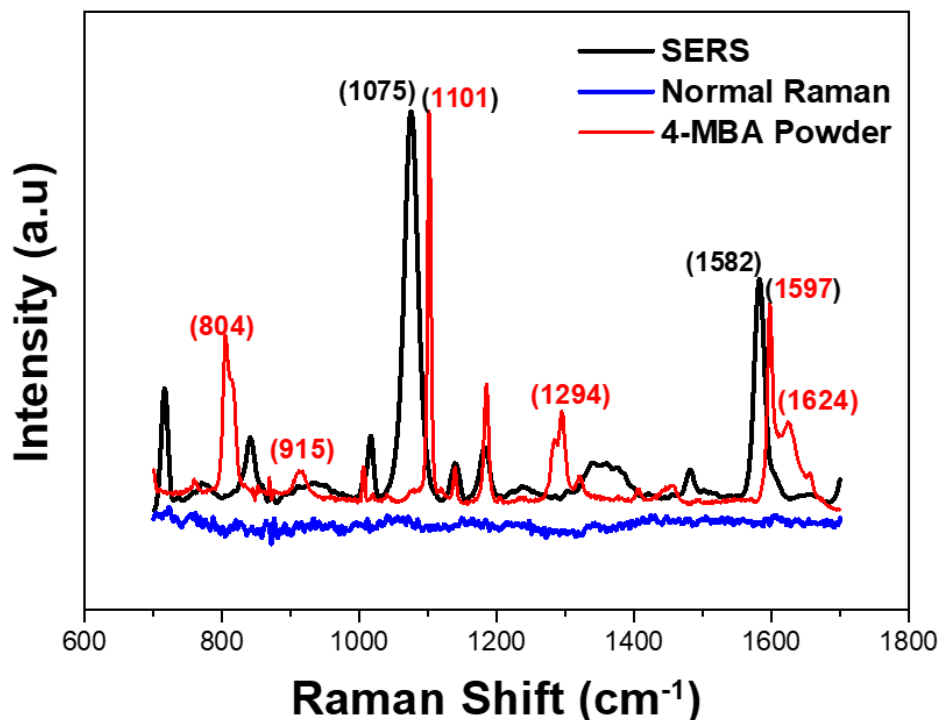

Figure 3.19: With black color is represented the SERS spectrum of 4-MBA in a AgSiO$_2$ substrate, with red color is the Raman spectrum of powder 4-MBA and with blue is the spectrum of the 4-MBA at low concentration without the presence of AgSiO$_2$ NPs.

molecule. It is worth noting that both peaks are shifted towards longer wavelengths compared to their Raman counterparts[101]. Under near-field illumination and in the presence of a metal surface, molecules experience a relaxation of Raman selection rules. Various factors influence the adsorption of molecules on a metal surface, and these factors
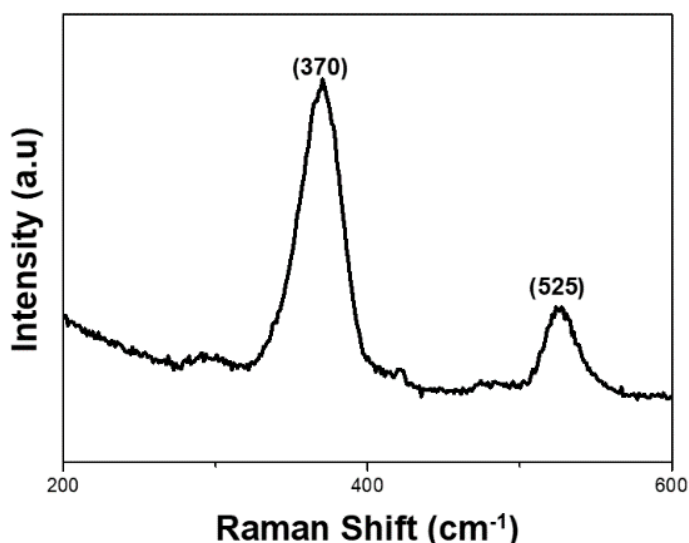

Figure 3.18: SERS signal of 4-MBA in lower wavenumbers.

74

encompass interactions between the substrate and the molecules, such as electrostatic forces, van der Waals forces, and $\pi - \pi$ stacking forces. As a result, certain bands that are typically restricted or hindered in conventional Raman spectra can appear in the SERS spectra. Similarly, molecule-metal charge transfer phenomena can lead to frequency shifts, as observed in the case of successful functionalization through S-Ag covalent binding. The presence of a band at 370 cm^{-1} in **Figure 3.18** signifies the Silver-sulfur vibration, serving as evidence for the successful functionalization[102]. Also, by the concomitant vanishing of the band at 915 cm^{-1}, showed in the insets of **Figure 3.19**, corresponding to the thiol S-H stretching vibration. Moreover, the absence of the latter
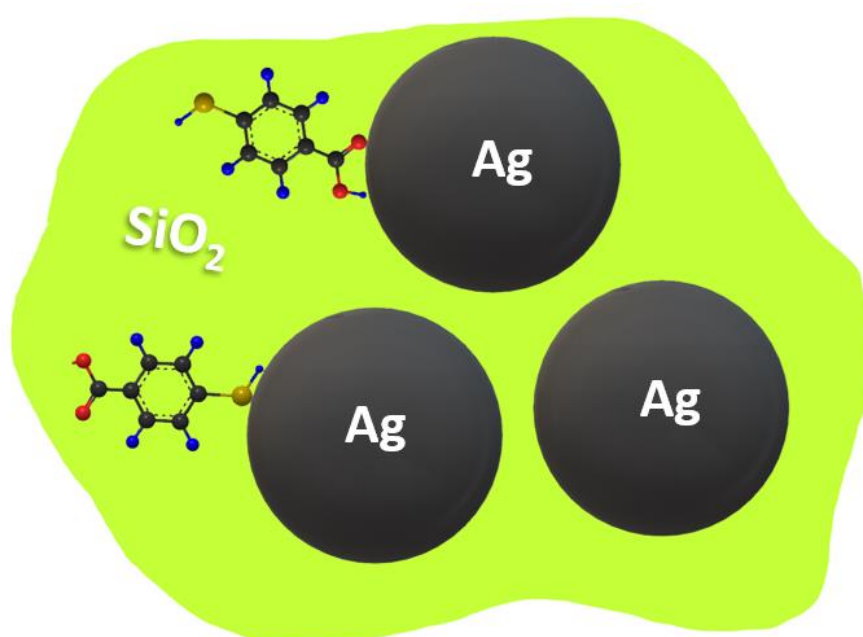

Figure 3.20: Illustration of the two ways that 4-MBA is connected with the Ag NPs . In the upper case the COOH is connected and in the lower the S atom is connected.

peak confirms that all the molecules contributing to the SERS signal are securely attached to the AgNPs through covalent bonds.

There are two main binding scenarios for the connection of 4-MBA with Ag NPs in this context, an illustration is provided in Figure 3.20. First, the COOH can interact with neighboring 4-MBA, leading to the formation of a chain on the Ag surface. Alternatively, the absorption of 4-MBA can occur through via absorption of the S atom, while the COOH forms hydrogen bonds with adjacent 4-MBA molecules, resulting in a zigzag pattern of dimers on the surface[103]. Another approach is pH dependent. Under

acidic conditions, 4-MBA adsorbs via the S atom, while under neutral to basic conditions, adsorption occurs through both the COO- terminal and S atom.

3.3.1 AgSiO$_2$ Nanofilm

Moving on, in the AgSiO$_2$ substrates the aim was to find the optimum parameters in the fabrication process in order to have the highest Enhancement Factor.
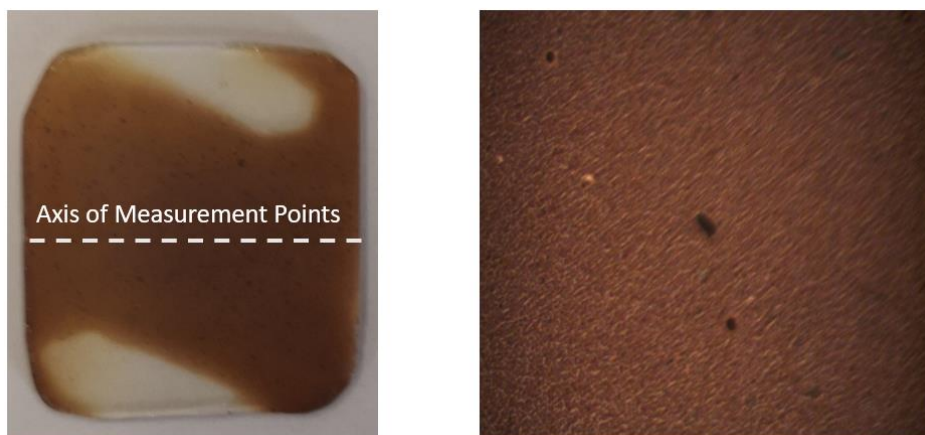

Figure 3.21: On the left is a Ag-SiO$_2$ nanofilm with marked the axis in which the data were collected. On the right is a photograph of Raman Microscope lens.

In every nanofilm 10 detection points were selected from one boundary of the substrate to the other, with that procedure we minimize the factor of . A typical photo with Raman microscope is presented in **Figure 3.21**. While SERS effect is not easy to have consistent spectrum intensity, we have managed to produce a substrate with high uniformity and controllable Ag-Ag interparticle distance. In **Figure 3.22** left the Raman spectra from the 10 Points on a 60s-10%-AgSiO$_2$ nanofilm and in **Figure 3.22** right the Average Spectrum of the forementioned points.
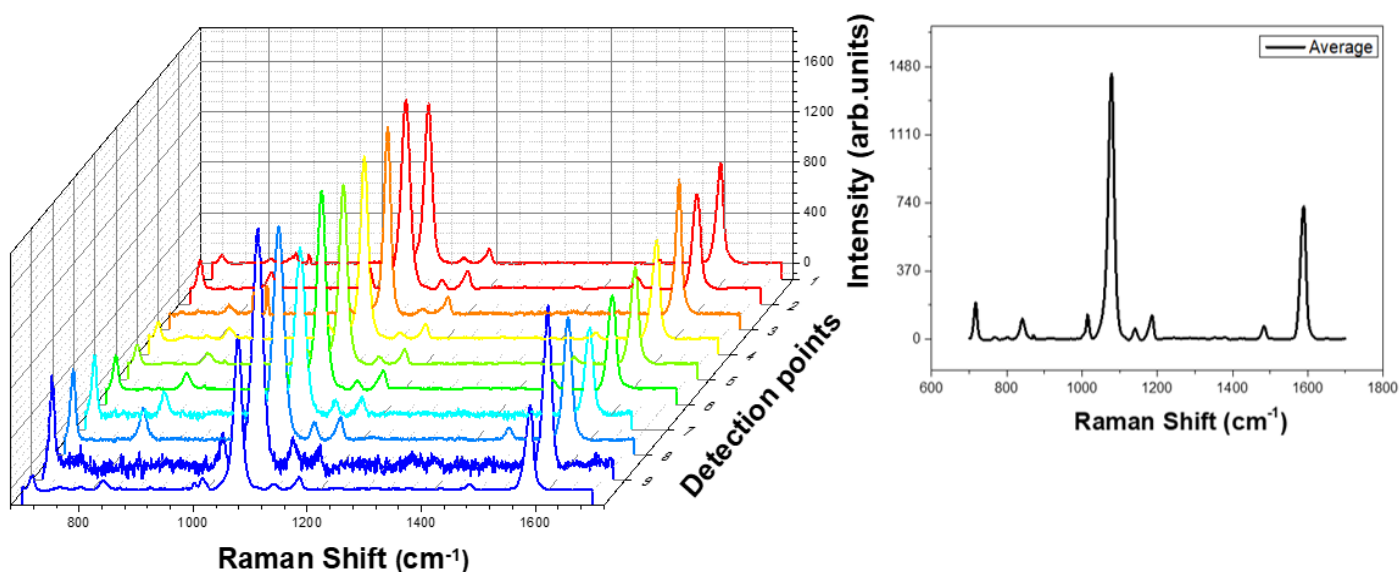
Figure 3.22: *On the left the spectra from the detected points of 60s-10%-AgSiO₂ nanofilm with 4-MBA aw Raman probe. On the right the average spectrum of the forementioned points.*

It is obvious that the intensity in all of the peaks varies from spot to spot and that is something that can explained through mainly 3 reasons:

- The near field doesn't have the same intensity everywhere in the nanofilm.
- The adsorption of the 4-MBA isn't a trivial process and the charge transfer phenomena that we have already mentioned influence the vibrational modes of the Raman reporter.
- The 4-MBA aren't equally distributed in the surface of the nanofilm and in some spots higher concentrations of molecules lead to higher signals.

The Raman peak with the biggest intensity, in 1075 cm⁻¹, will be used for further investigation of the SERS phenomenon. The **Figure 3.23** is presenting the variation of the forementioned peak and corresponds to the detection points of **Figure 3.22**. While there is a notable deviation about 600 counts between the highest and lowest intensity in the 10 measured points, the deviation from average spectrum isn't more than 20%.

Investigating a bit further the connection between concentration of the Raman reporter and peak intensity, four different concentrations of 4-MBA were drop-casted into a
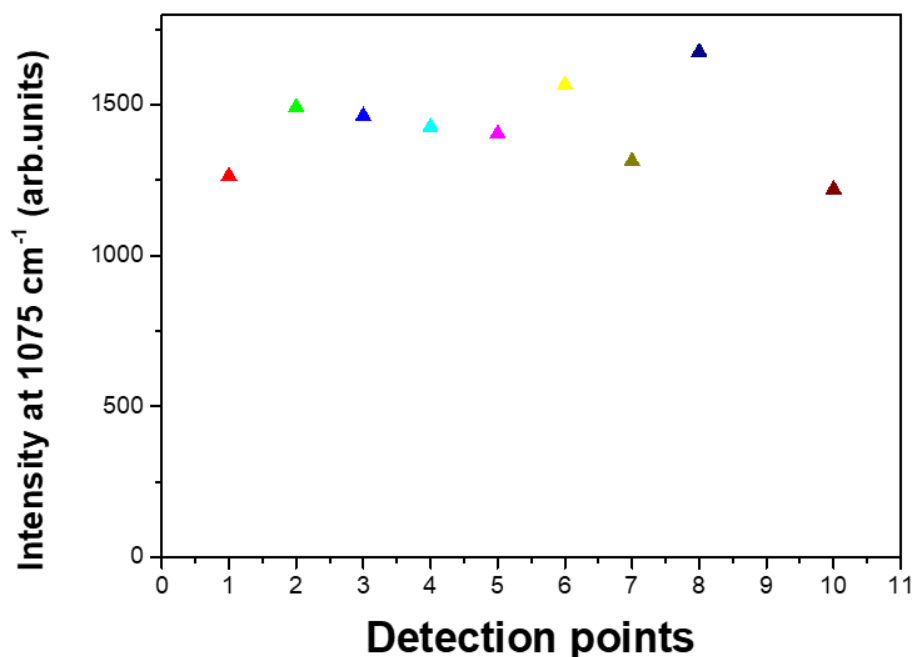

Figure 3.23: Deviation of the peak intensity at 1075cm⁻¹.

nanofilm, starting with the smallest and finishing with the biggest one. As it is illustrated in the **Figure 3.24**. the increase of the concentration has an almost linear increase in the intensity of the Raman peaks. Additionally, the Limit of Detection in our best substrate was 1pM of molar concentration of 4-MBA.
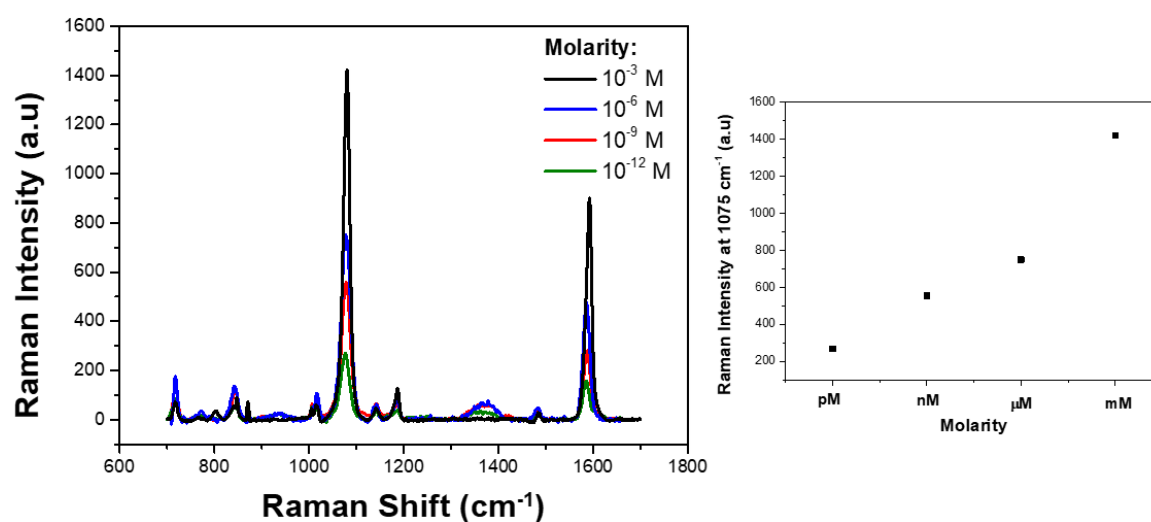

Figure 3.24: On the left the SERS spectra for different 4-MBA concentrations and on the right the Raman intensity at 1075cm⁻¹ plotted with Molarity of 4-MBA.

For the rest of the analysis the previous model will be followed, in every nanofilm 10 points will be measured throughout its surface and only the average spectra will be presented due to reasons of space economy.

Starting with the 6% wt SiO_2 nanofilm (**Figure 3.25:**), its limit o detection (LOD) was the region of micro moles 4-MBA per liter. That gave rise to an EF of 10^4 (the calculation of EF has been analyzed in the 2.2 subchapter). In first glance it would be expected that when the interparticle distance between Ag NPs is the smallest the SERS phenomenon would be at its maximum. In contrast, the small interparticle distance that correspond to SiO_2 wt 6% can not result in strong hot-spot formation that generate high
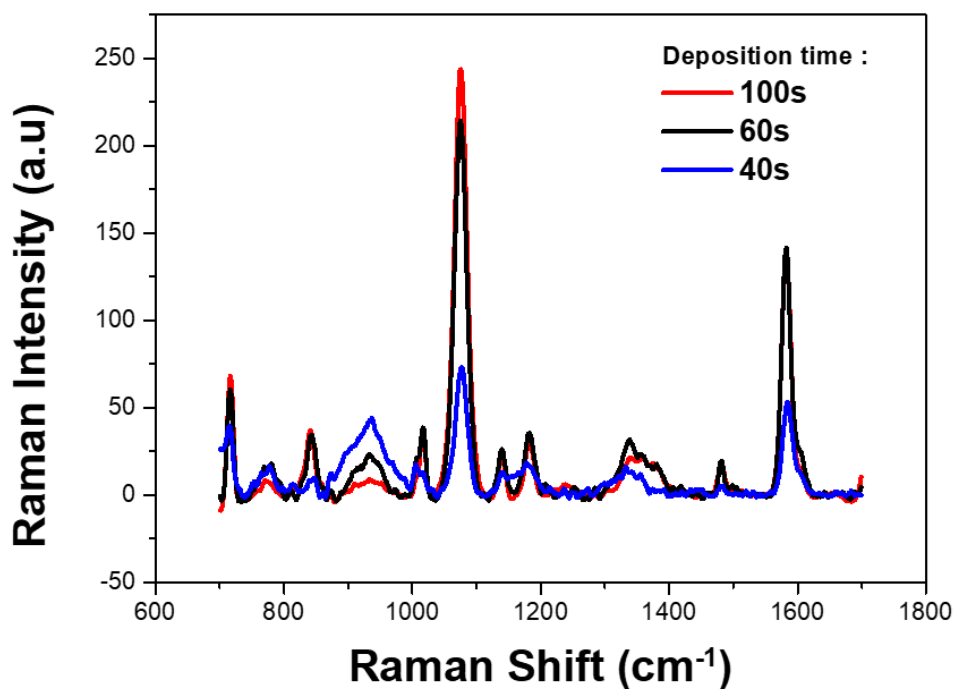

Figure 3.25: The average Raman spectra of 6% - $AgSiO_2$ are displayed, with red color t_D 100s, with black color t_D 60s and with blue color t_D 40s.

SERS intensity.

Additionally, the substrate with deposition time of 40s has the lowest intensity due to lack of sufficient quantity of NPs deposited in the glass substrate, as it has the lowest thickness. Also, the absence of the 849cm^{-1} raman peak only in the 40s spectra justifies the absence of COO$^-$ bending mode. The substrates with 100s and 60s deposition times were significantly higher in spectrum intensities, up to 3 times more than the 40s t_d nanofilm, that meant higher film thickness is needed for sufficient hot-spot formation.

Figure 3.26: *The average Raman spectra of 10% - AgSiO$_2$ are displayed, with red color t_D 100s, with black color t_D 60s and with blue color t_D 40s*

Moving on to the next batch of nanofilms, the 10% wt SiO$_2$ (**Figure 3.27**) were the ones with the highest LOD, the detected concentration was 1pico mole of 4-MBA per liter
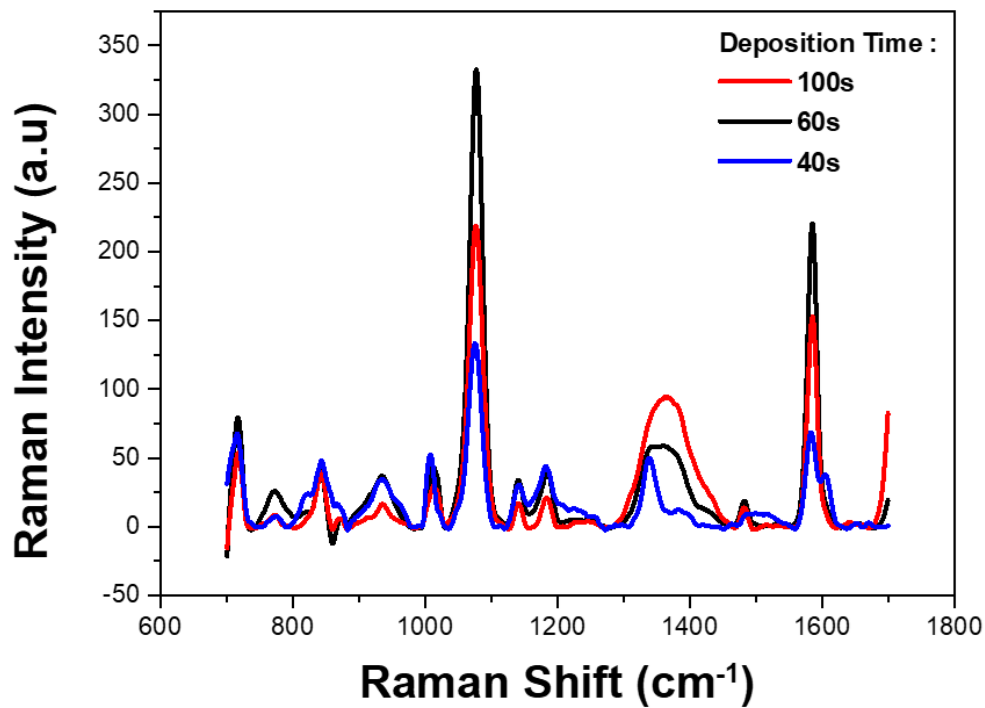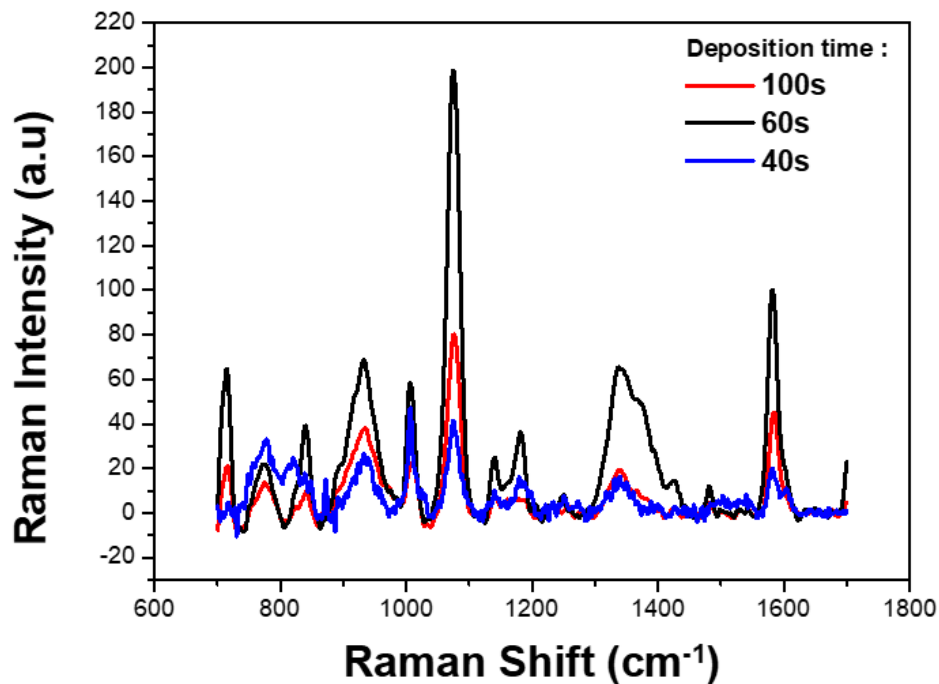

Figure 3.27: *The average Raman spectra of 20% - AgSiO$_2$ are displayed, with red color t_D 100s, with black color t_D 60s and with blue color t_D 40s*

giving rise to an Enhancement Factor of almost 10^{11}. Such a low concentration reaches the limits of single molecule detection, meaning that it is about one molecule per Raman Spot Area. As far as thickness of the film is concerned the optimum isn't the 100s but the 60s of deposited nanoparticles, that can interpreted with the fact that to thick films are packed with Ag NPs and the SERS intensity can be harnessed with burning in that way quantity of the 4-MBA.

Deposition time(s)	6%	10%	20%	SiO$_2$ wt. %
100	6.E+04	6.E+10	2.E+10	
60	5.E+04	8.E+10	5.E+10	
40	2.E+04	3.E+10	1.E+10	

Table 3.7: Enhancement Factors for AgSiO$_2$ nanofilms.

Finally the 20% wt SiO$_2$ nanofilm had similar results with the 10% AgSiO$_2$ but with lower intensities, EF $\sim 10^{10}$. Again, it is obvious that the 60s is preferable as far as thickness is concerned.

Summarizing all the Enhancement Factors are displayed in **Table 3.7** and plotted in **Figure 3.28**.
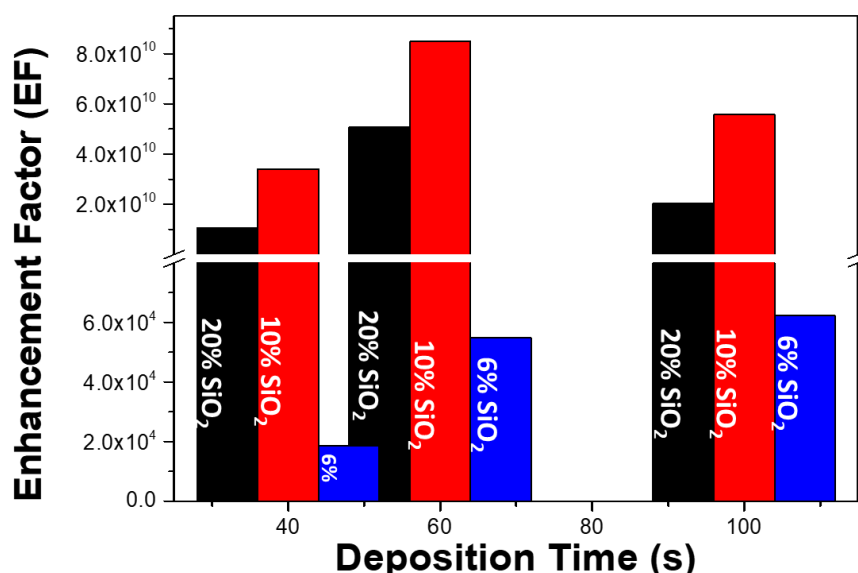

Figure 3.28: Enhancement Factors plotted with x-axis being the deposition time.

It is noted that a "bell" shape curve tend to form in **Figure 3.28** with the t_d of 60s being the optimum deposition time in both 10 and 20 % wt SiO$_2$ and 10% SiO$_2$ is the most effective substrate from FSP fabrication.

For further investigation another Raman Reporter was used, Rhodamine 6G. Its SERS

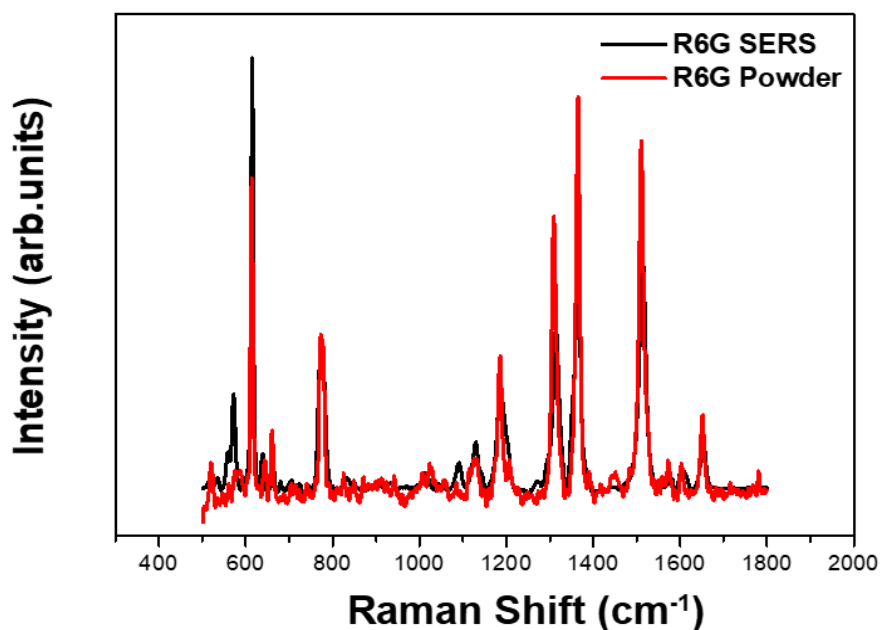*Figure 3.29: With black color is represented the SERS spectrum of R6G in a AgSiO$_2$ substrate and with red color is the Raman spectrum of powder 4-MBA*
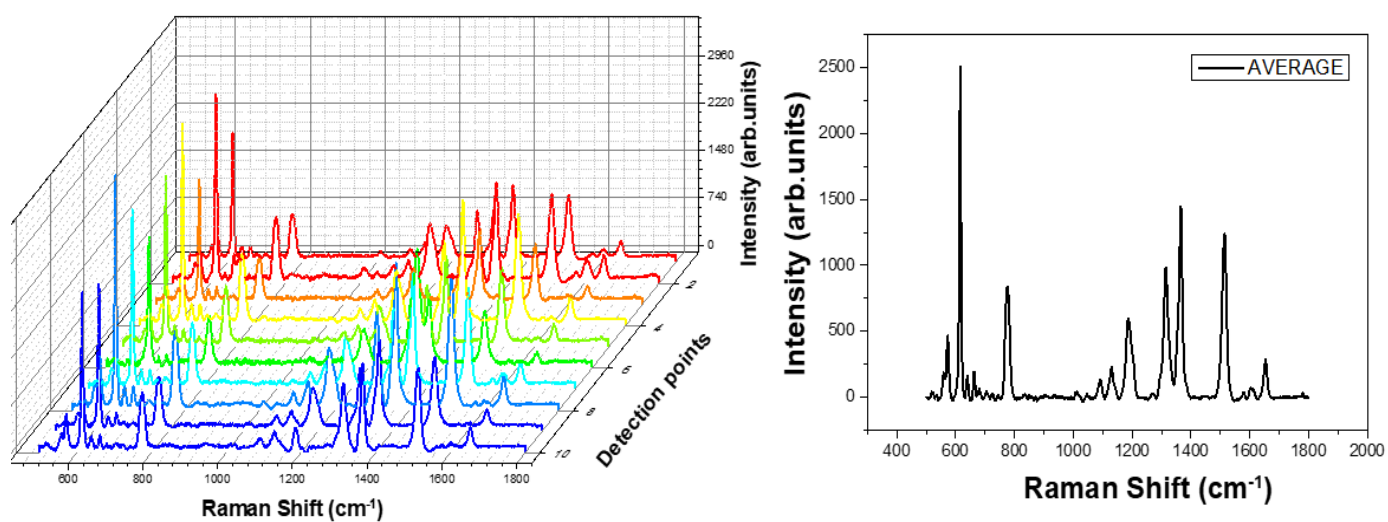

Figure 3.30: On the left the spectra from the detected points of 60s-10%-AgSiO$_2$ nanofilm with R6G as Raman probe and on the right the average spectrum of the forementioned points.

spectra compared to the powder Raman measurement is displayed in **Figure 3.29** .No

deviation is observed between the position of the SERS peaks and the powder spectra of Rhodamine 6G (**Table 3.6**). The 10% wt SiO_2 nanofilms were used in the following analysis. Again, the same pattern was followed in the analysis, 10 point across the nanofilm were measured and the results are presented in **Figure 3.30**.

The concentration of R6G that was drop casted into the nanofilms was 1 micro mole per liter. That detection limit gave rise to an EF of 10^6. Again, the 10% 60s $AgSiO_2$ substrate was the most efficient making it clear that for best hotspot distribution and

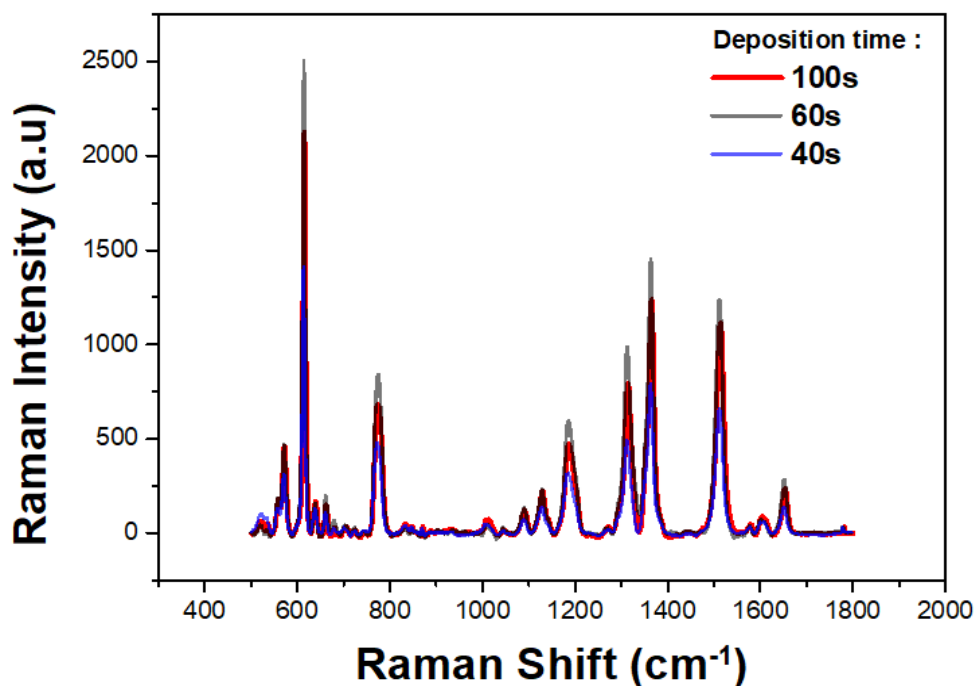*Figure 3.31: The average Raman spectra of 10% - AgSiO$_2$, with R6G as Raman reporter, are displayed. With red color t_D of 100s, with gray color t_D of 60s and with blue color t_D of 40s.*

optimum film thickness the 10% wt SiO_2 and t_d 60s is preferable. The average Raman spectra of the three different deposition times is displayed in **Figure 3.31**.

3.3.2 AgTiO$_2$ Nanofilm

Moving on, the next for analysis substrate is $AgTiO_2$. While, SiO_2 acted as a dielectric spacer among the Ag NPs in this case we cannot assume that the TiO_2 acts the same. The main reason for that claim is because the TiO_2 is a semiconductor with a 3.2eV
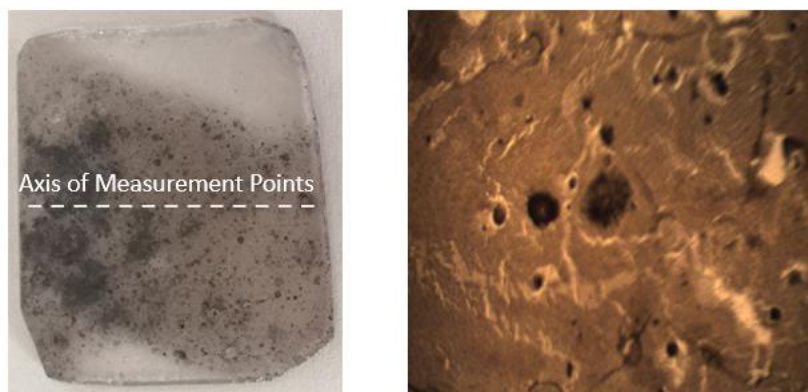
Figure 3.32: On the left is a AgTiO₂ nanofilm with marked the axis in which the data were collected. On the right is a photograph of Raman Microscope lens.

bandgap and its electronic bands interfere with the adsorption process.

The procedure again that was followed remained the same, in a nanofilm 10 point were measured by Raman spectrometer starting from one edge of the substrate and finishing to the other (**Figure 3.32**).

In big contrast with the $AgSiO_2$ substrates the $AgTiO_2$ weren't as consistent in the Raman intensity, as it is observed in **Figure 3.33** there is a plethora of values starting from 4132counts to 312 counts. The adsorption process is influenced by TiO_2
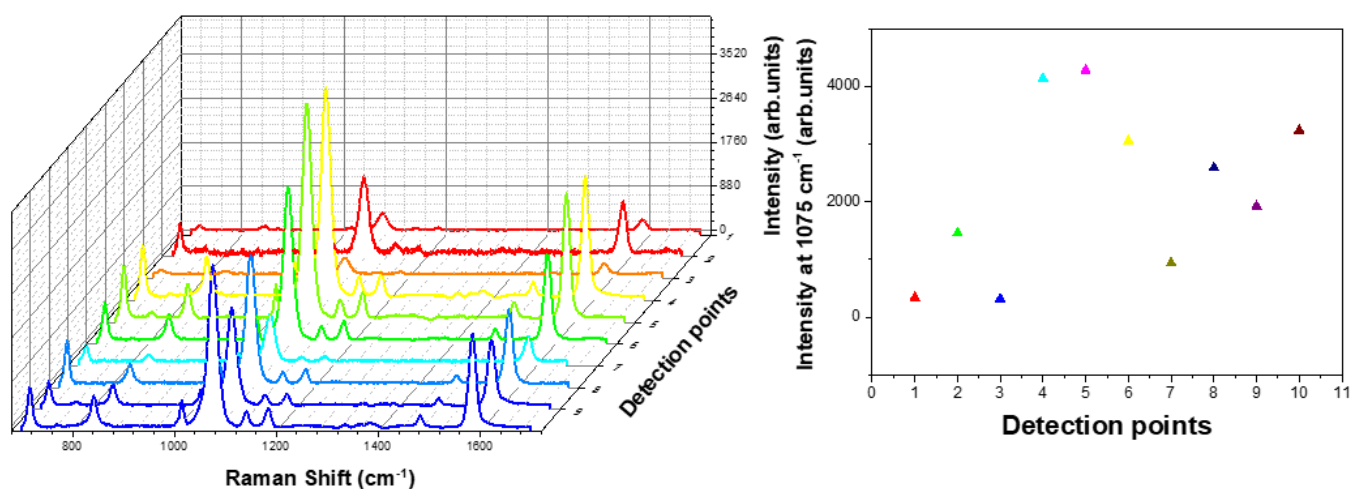
Figure 3.33: On the left the spectra from the detected points of 60s-10%-AgTiO₂ nanofilm with 4-MBA as Raman probe and on the right the deviation of the peak intensity at 1075cm⁻¹.

electronic zones making the chemical factor of SERS contributing more in some
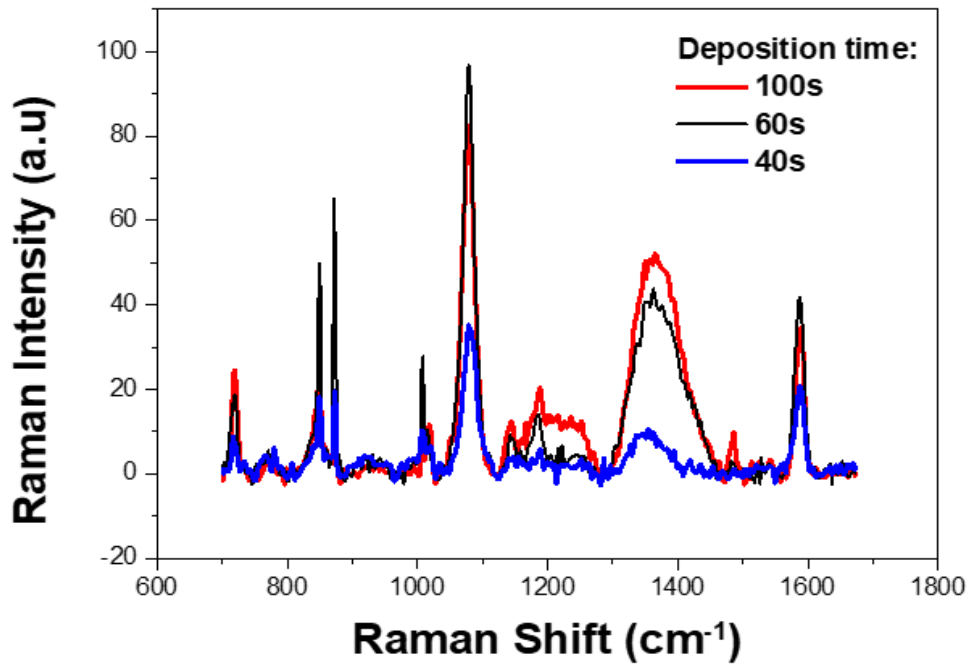
Figure 3.35: The average Raman spectra of 0.6M - AgTiO₂ , with 4-MBA as Raman reporter, are displayed. With red color t_D of 100s, with black color t_D of 60s and with blue color t_D of 40s.
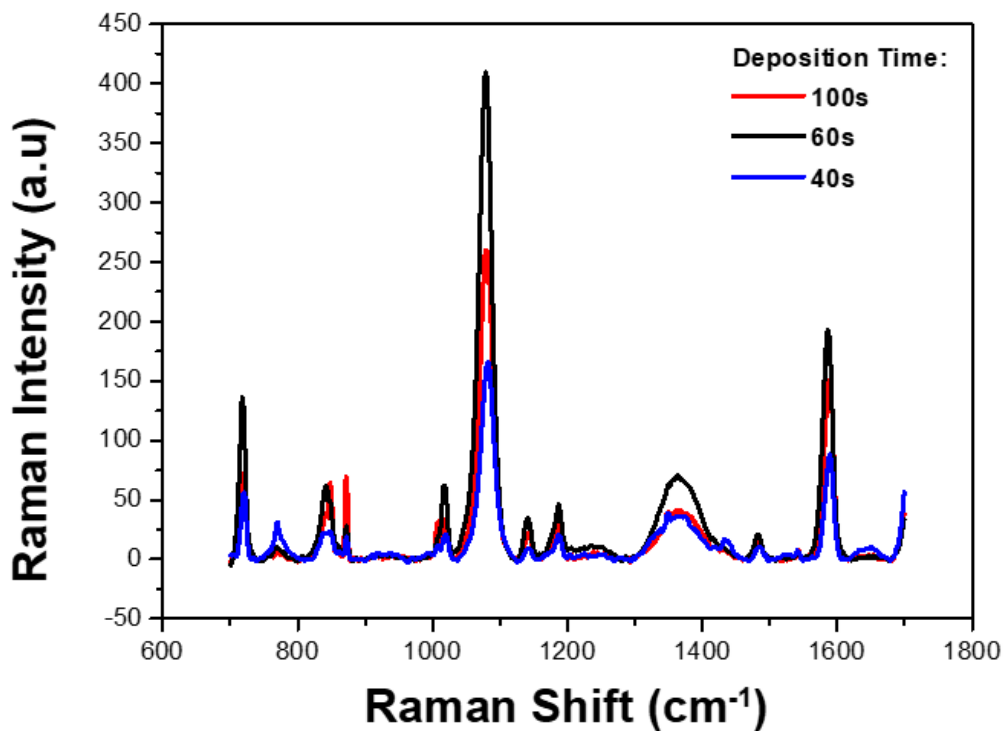
Figure 3.34: The average Raman spectra of 0.3M - AgTiO₂ , with 4-MBA as Raman reporter, are displayed. With red color t_D of 100s, with black color t_D of 60s and with blue color t_D of 40s.

spots. The SERS spectra of the 0.6M AgTiO₂ nanofilms in **Figure 3.35** follows the

same pattern as the AgSiO$_2$ substrates, meaning that 60s deposition time gives the highest EF and 0.3M TiO$_2$ concentration is preferable, as is shown in **Figure 3.34**. The 0.6M concentration as we observe in **Figure 3.35** is 3times less intense in SERS signal. The plotted Enhancement Factrors (**Figure 3.36**) are in the region of 10^5 and are forming a bell shape distribution, with the most preferable area near 60s t$_d$ and 0.3M concentration of precursor. In all cases Ag was 50% wt compared to TiO$_2$.
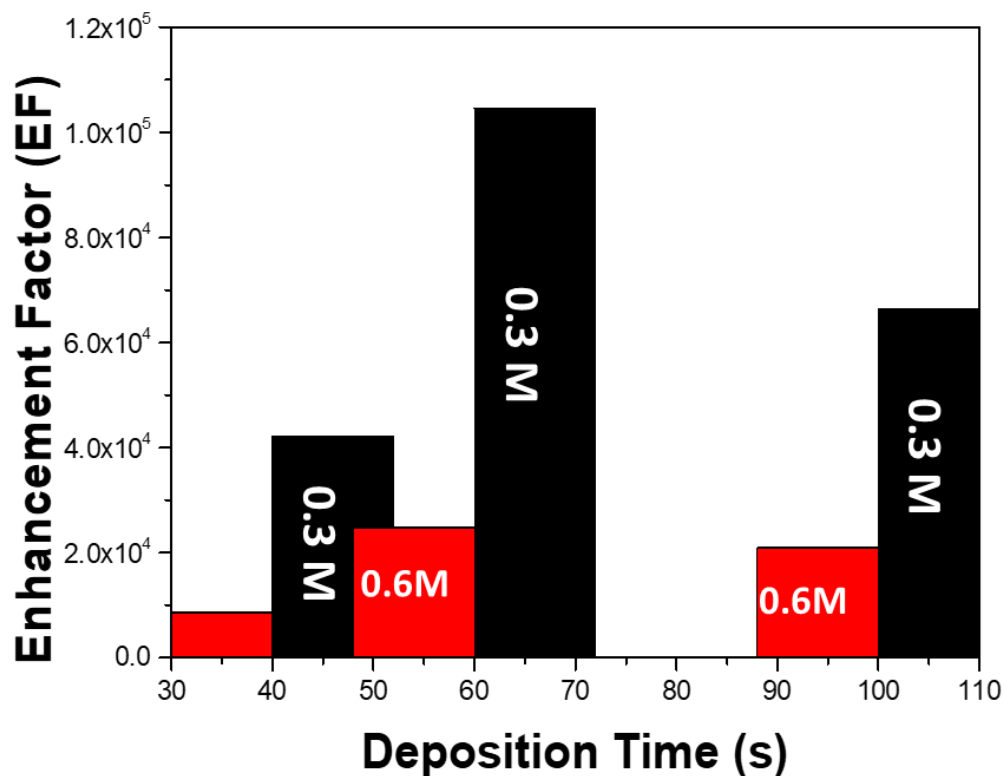
Figure 3.36: Enhancement Factors plotted with x-axis being the deposition time.

3.4   SERS Detection on Pesticide Thiram

Thiram[104] is a chemical compound that exists in a powdered form. Thiram is commonly used as a pesticide in agricultural practices. It is primarily used as a fungicide to protect crops from various fungal diseases. It is important to note that thiram is intended for use as a pesticide and should not come into direct contact with humans. SERS-active substrates that can detect Thiram in concentrations below 10^5 M is a helpful analytical tool for food analysis and combined with the low cost of plasmonic nanofilms has.

Initially, we gathered the Raman spectra of a large quantity of Thiram. Within this spectrum, we observed a Raman peak at 565 cm^{-1}, which indicates the stretching of S-S bond, a peak at 444 cm^{-1} which corresponds to bending CH$_3$NC and stretching C=S,
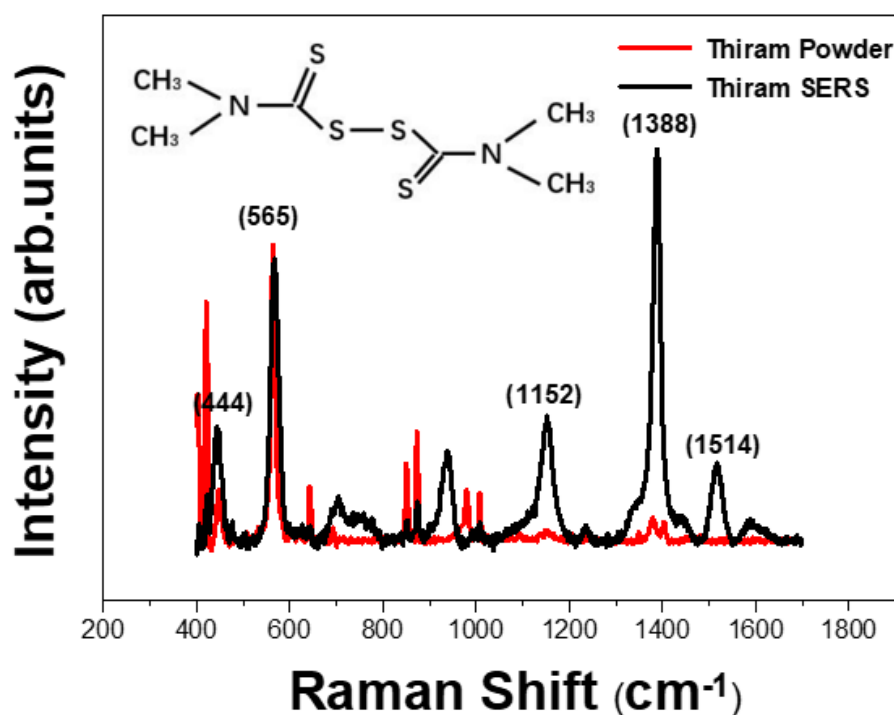
Figure 3.37: With black color is represented the SERS spectrum of Thiram in a AgSiO$_2$ substrate and with red color is the Raman spectrum of powder Thiram..

and a weaker peak at   1388 cm^{-1} which corresponded to CH$_3$ bending and C-N stretching. In **Figure 3.37** the Powder thiram spectra is presented compared to it's SERS spectra.

While powder Thiram is easy to measure, when its concentration is in the order of >10^{-5} M it is impossible and no significant spectra can be observed. Subsequently, we used our best SERS-active substrate which is 10% -60s-AgSiO$_2$ in trying to enhance

the Thiram signal. **Figure 3.39** illustrates the detection of SERS spectra for Thiram concentrations 10^{-9} M. The SERS signal has more peaks and more significantly the peak in 1388 cm^{-1} now is the stronger one. Additionally, appear 2 new peaks at 1152 and 1514 cm^{-1} something that makes the identification of Thiram even easier. The peaks and the

Raman Shift (cm^{-1})	Vibrational modes
444	Bending CH$_3$NC, stretching C=S
565	stretching S-S
1152	rocking CH$_3$, stretching C-N
1388	Bending CH$_3$, stretching C-N
1514	stretching C-N

Table 3.8: Raman peaks of Thiram with it's corresponding Vibrational modes.

vibrational modes are summarized in **Table 3.8**. As far as the way Thiram connects to the Ag NPs, again the Sulfur atom is the one that is connected in the Ag surface, an illustration of that is presented in **Figure 3.38**

Consequently, 150μl of dissolved in ethanol Thiram was dropcasted into the nanofilm while its concentration was 10^{-8}M. The 10points that were measured by
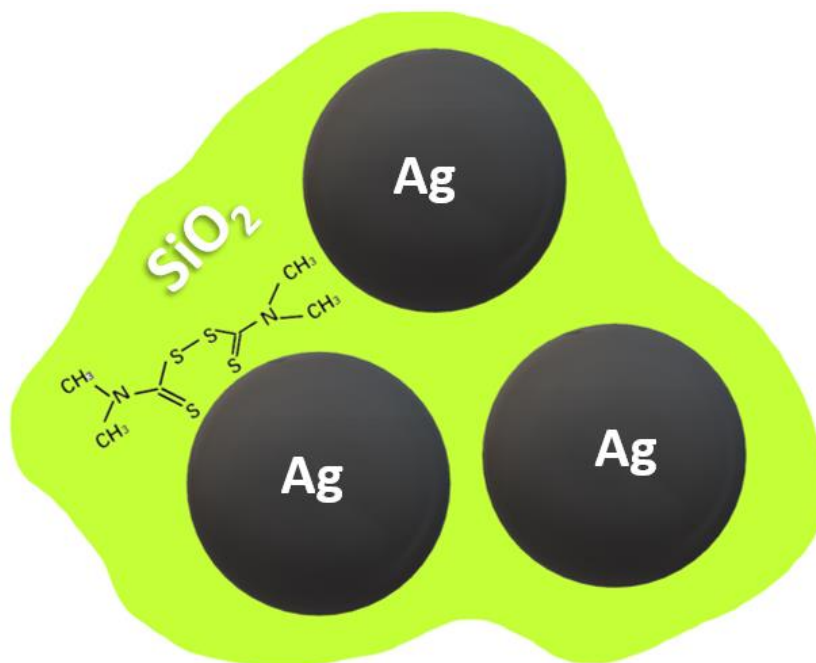
Figure 3.38: : Illustration of the ways that Thiram is connected with the Ag NPs , which is through S atoms.

Raman spectrometer and the average spectra are presented on the **Figure 3.39**.
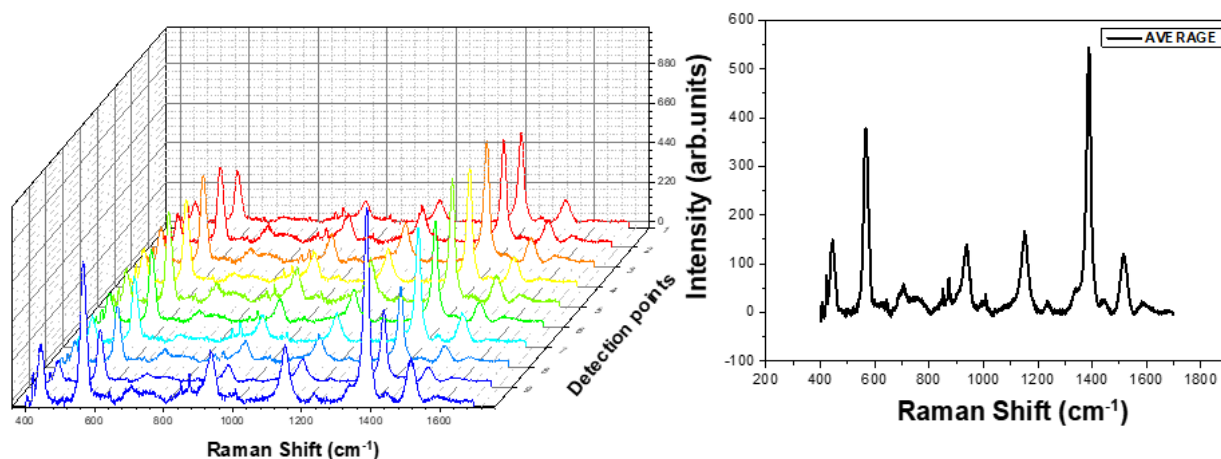
Figure 3.39: On the left the spectra from the detected points of 60s-10%-AgSiO$_2$ nanofilm with Thiram as Raman Reporter and on the right the average spectrum of the forementioned points.

Calculating the EF for the 566 cm^{-1} peak the result is 10^7 while for the 1388 was 10^{10}.

Summarizing, the AgSiO$_2$ substrate we constructed is capable for measuring low concentrations of organic molecules producing high EF. Additionally, the limit of detection can be further exceeded in lower concentrations if the organic molecule stays more time in the nanofilm before the measurement and the percentage of the adsorption process is increased.

3.5 PIERS Effect on AgTiO$_2$ Nanofilm

In this Chapter, we will focus on the AgTiO$_2$ substrates. It is already obvious from the previous chapters that AgTiO$_2$ isn't as efficient as AgSiO$_2$ resulting in the thought that titanium oxide isn't the appropriate partner for silver in the nanofilm heterostructure. However, with the addition of the step of illumination oxygen vacancies are created in the TiO$_2$ grid enabling photo-induced charge-transfer processes[105].

3.5.1 Oxygen Vacancies as the main mechanism

The approach investigating PIERS had similar first steps with SERS. In the beginning 150μl of 4-MBA were drop-casted into the single nozzle nanofilm. The concentration of 4-MBA was 10^{-6} M and normal SERS spectra were gathered as is presented in **Figure 3.40** with red color. In the next step a UV lamb was placed above

Figure 3.40: 4-MBA Raman Spectra, with black color the PIERS signal and with red color the SERS signal.

the nanofilm for 2.5 hours. After the end of illumination the Raman Spectra that was gathered and presented with black color in **Figure 3.40**. It should be noted that due to
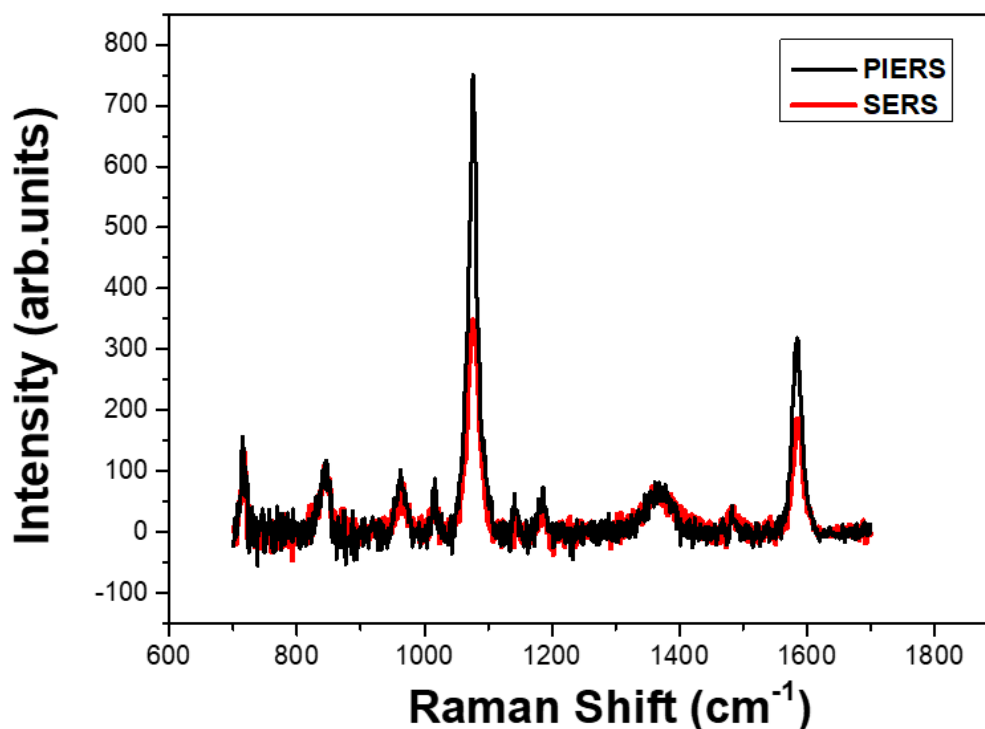
the different location of the lamb and the Raman Spectrometer critical time, and possibly even greater PIERS signal, was lost from the moment the UV radiation was shutted down until the raman spectra was gathered.

Figure 3.41: With black color the decrease in Intensity of peak at 1075cm^{-1} with respect to time after the UV illumination, with red color is the deviation of the same peak without the UV pre-illumination

Raman spectra were collected from the same spot every 3 minutes in the beginning and then every 10 minutes until the intensity in the 1075 cm^{-1} peak was fully retracted to the SERS original intensity. The decrease in peak intensity is presented in **Figure 3.41**. Also the Raman response of the substrate without UV radiation (**Figure 3.41** red color) was measured in order to ensure that the photo enhancement was due to PIERS effect ant not due to laser induced photo-bleaching. As it is observed, maximum intensity was 750 counts in the strongest peak of 4-MBA and after UV irradiation, the signal decayed back to the baseline SERS signal of 350 counts within almost 30min.

The mechanism behind than enhancement, which was 215% greater than original SERS, is the surface of the material undergoes a process where high-energy photons (specifically UVC) are utilized to remove oxygen atoms. This expulsion of oxygen atoms is potentially facilitated by a photoreaction involving adsorbed H_2O and O_2. As a result, the concentration of Vo (vacancy-type defects) increases. The formation

of these defects at the atomic level allows for improved Raman transitions due to resonant conditions, an illustration of the V_0 formation is presented in **Figure 3.42**.

When the UV irradiation ends, the PIERS signal decayed back to the baseline SERS signal as a result of healing of the surface upon exposure to air. Summarizing, the observed changes over time in the PIERS enhancement (P) are mainly influenced by
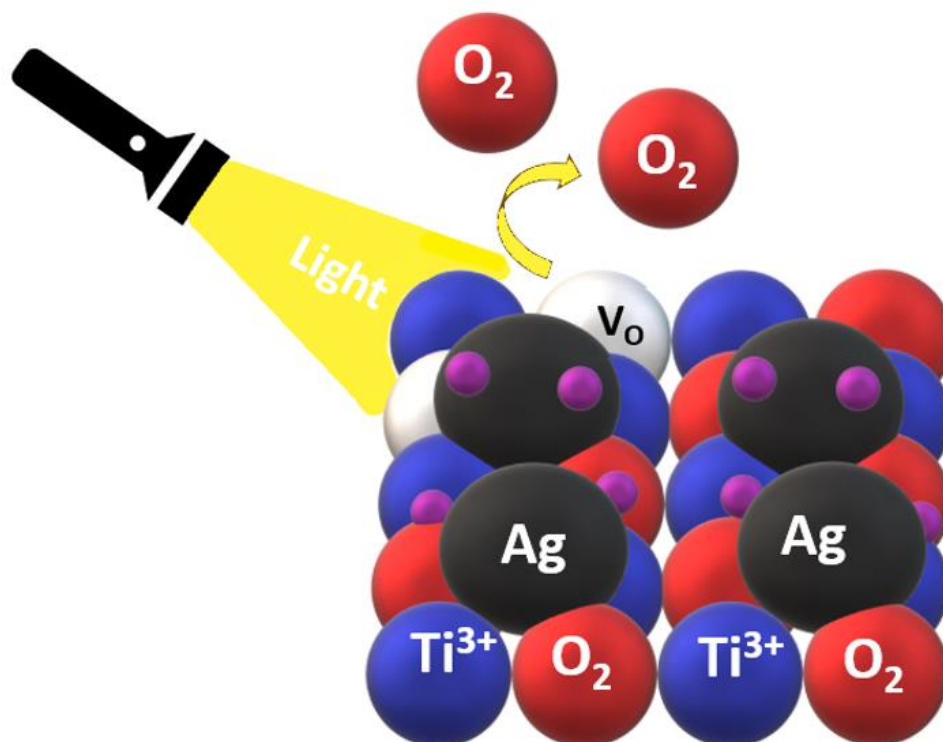
Figure 3.42: Illustration of PIERS mechanism.

three factors: the formation (Vo+) and healing (Vo-) dynamics of vacancies (Vo), as well as the laser-induced bleaching (L) of MBA molecules. The alterations in vacancy concentration are determined by the properties of the substrate and its photocatalytic activity. Therefore, the two factors, Vo^+ and Vo^-, are considered to be unrelated to the probe molecule. In our case, after the UV radiation there is not any further VO_2 formation, so the corresponding term isn't contributing and equation 1 is describing our system.

$$P = V_O^- + L \qquad (3.1)$$

The AgTiO$_2$ nanofilm that was analyzed for PIERS effect was single flame made, meaning precursors of TTIP and Silver acetate were burned in the same time creating distortions in the TiO$_2$ grid as is is already noted in substrate analysis. In a second step,
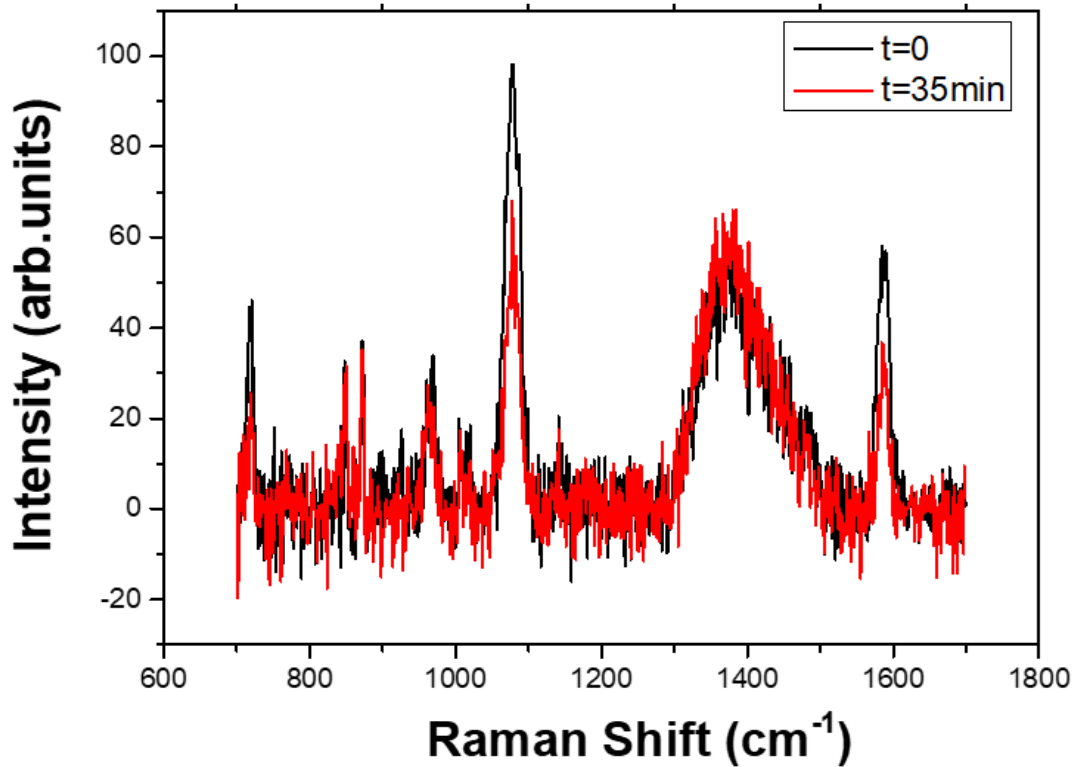
Figure 3.44: *4-MBA Raman Spectra in a AgTiO$_2$ nanofilm made sequentially, with black color the PIERS signal and with red color the same signal after 35minutes.*
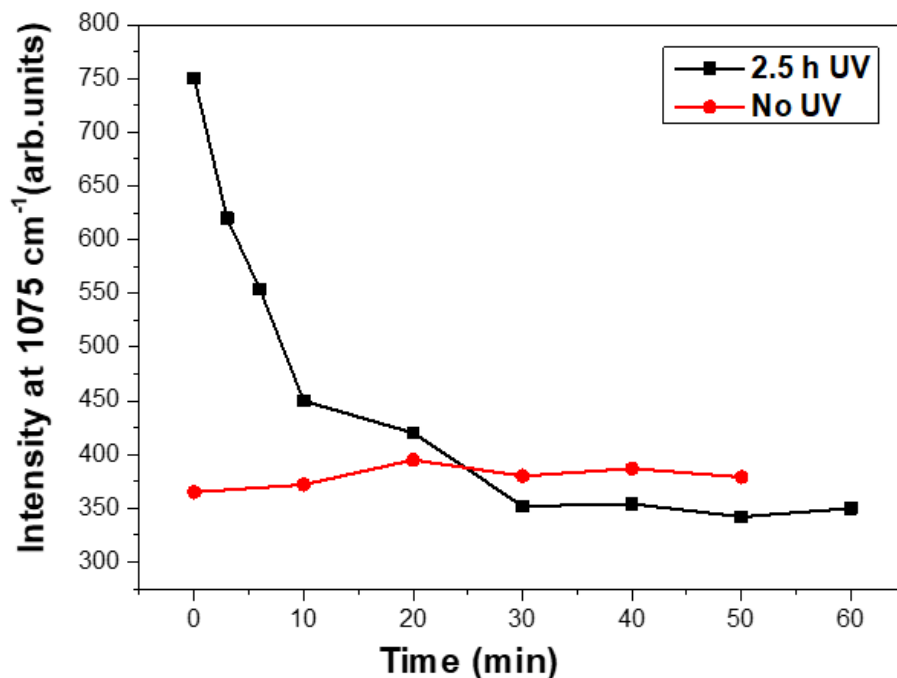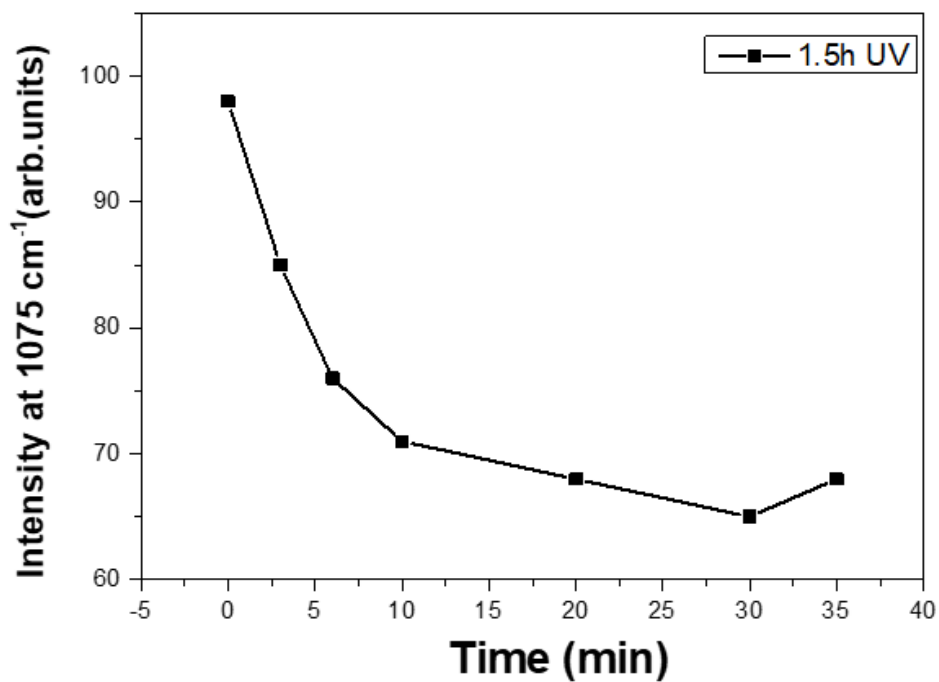

Figure 3.43: *With black color the decrease in Intensity of peak at 1075cm^{-1} with respect to time after the UV illumination.*

a sequential nanoparticle film was fabricated meaning the TiO$_2$ was formatted first in

the glass substrate and then the Ag NPs were deposited afterwards.

In the Sequential nanofilm we placed the UV lamp for 90 minutes but the PIERS enhancement was significantly low, in the region of 110% from the original SERS intensity. After 35 minutes from the illumination several Raman spectra were collectred and the variation in 1075cm $^{-1}$ peak are presented in **Figure 3.44**. While the decrease in signal is observed the PIERS effect is blocked from two main reasons:

- The sequential deposition blocked the TiO^{3+} centers as the Ag NPs were deposited after TiO_2 on the glass substrate, the high-energy photons couldn't form enough V_O 's in the TiO_2 grid so it is obvious the PIERS efficiency wasn't as high as it was expected.

- The other reason is in the amorphisity and the distortions which are made in the single nozzle FSP that work as a boost as the electrons that can be stored in those states help in the charge-transfer processes.

3.5.2 Enhancing Limit of Detection
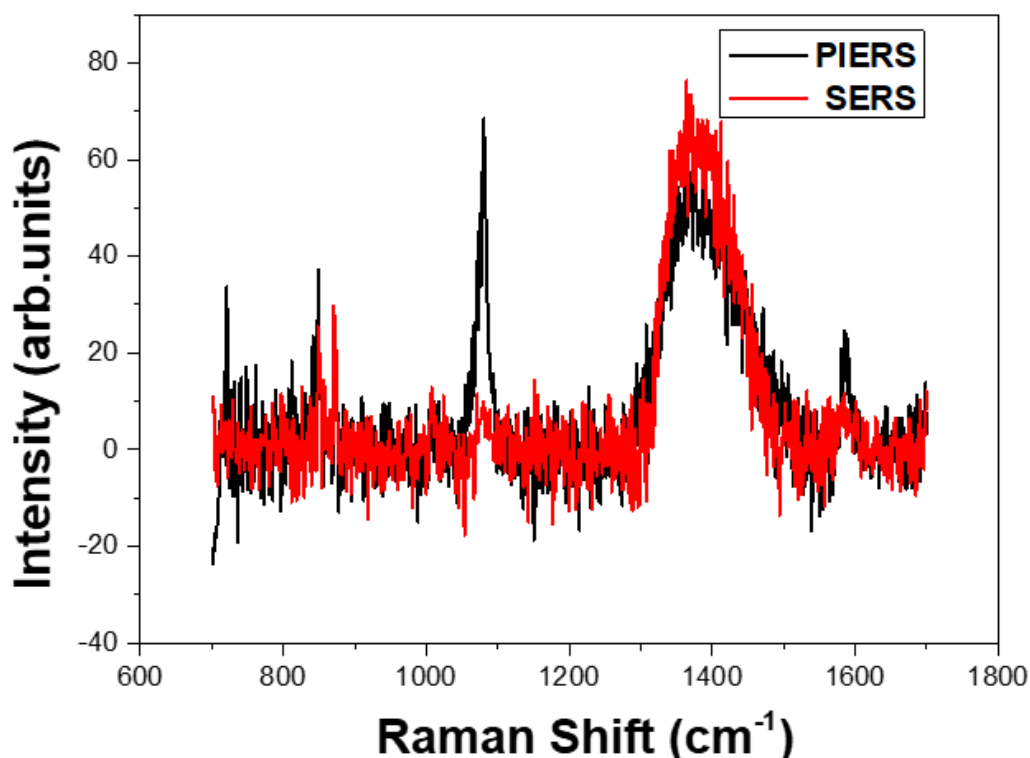
Figure 3.45: 4-MBA Raman Spectra, with black color the PIERS signal and with red color the SERS signal.

In the 60s-0.3M AgTiO$_2$ nanofilm that was used in PIERS experiments another approach was followed in order to unveil the more applicable side of the effect.

In the nanofilm 150μl of 4-MBA were dropcasted while the concentration the Raman reporter was 1nM, meaning that no SERS signal could be obtained from measurement (**Figure 3.45** red colour). The next step was to illuminate the nanofilm for 1.5h. After that raman measurement was gathered from the same spot and 4-MBA peaks were observed, as it is shown in **Figure 3.45** with black color. It is a significant expansion in the Limin of detection for AgTiO$_2$ substrate as only 1μM could be detected without the addition of the light.

In the **Figure 3.46** that follows, measurements were made in short periods of time and again the intensity of the 1075cm^{-1} peak dropped to the before UV counts as a result of healing of the surface upon exposure to air (relaxation time).

For further explanation, in the spot that the measurements were conducted the near field (electromagnetic factor) from the plasmonic NPs wasn't strong enough in order to give rise to the analogous SERS spectra. However, with the UV radiation the V$_o$ formation enhanced the chemical factor of SERS and the needed spectra could be
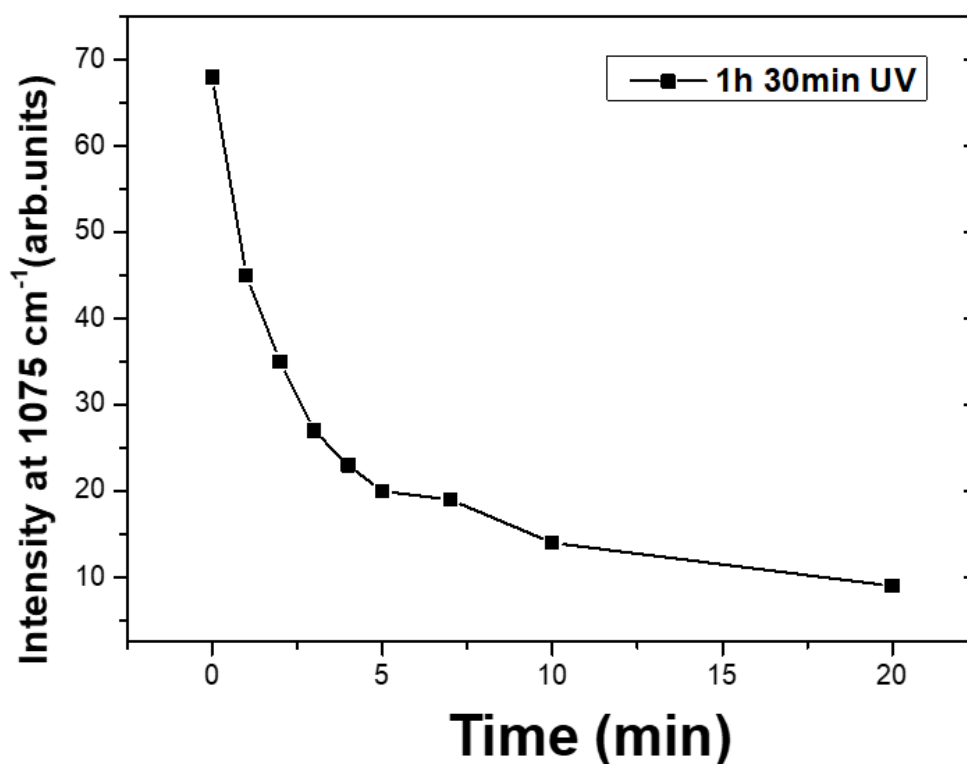
Figure 3.46: *The decrease in Intensity of peak at 1075cm^{-1} with respect to time after the UV illumination.*

obtained. This expansion of the LOD opens up the possibility of really high EF and the detection Single molecule SERS spectra which is the ultimate goal for every SERS active substrate.

Chapter 4

Conclusions

Summarizing the experimental results, in this M.Sc thesis:

[i]   Successful assembly of nanoparticle films by Flame Spray Pyrolysis (FSP) technology and deposition on glass substrates. The two nanofilms that were fabricated were $AgSiO_2$ and $AgTiO_2$ with different variables changing in each case, such as deposition time, SiO_2 wt% and TiO_2 molarity.

[ii]   By changing the deposition time of the NPs in the substrate, controllable film thickness was achieved. Also, with different SiO_2 wt% controllable Ag-Ag distance was attained.

[iii] Surface-enhanced Raman scattering (SERS) study of $AgSiO_2$ and $AgTiO_2$ nanosensors with MBA and Rhodamine 6G as Raman reporters, all the nanofilms were SERS active with the optimum deposition time to be 60s for both substrate categories. Additionally, the optimum Ag-Ag distance is given from 10% wt SiO_2 .

[iv]   SERS detection of the pesticide Thiram was achieves with a EF of is 10^7 for 566 cm^{-1} peak and 10^{10} for the 1388 cm^{-1} Raman peak.

[v]   Photo-induced enhanced Raman spectroscopy (PIERS) study, of AgTiO2 as substrate, was conducted and an enhancement of factor 2 between PIERS and SERS spectra was observed.

[vi]   After the interaction of the illuminated nanofilm with ambient air the PIERS signal subtracted to the SERS one. Confirming in that way that the observed enhancement was due to that surface-active Vo that are formed from UV illumination.

[vii] Comparison of PIERS effect on single nozzle made nanoparticle films versus sequential deposition, showed that single nozzle $AgTiO_2$ was preferable. The interface distortions that are created by FSP in the single nozzle case tent to create more V_O. Additionally, in the sequential deposition

firstly the TiO_2 were deposited and after than the Ag NPs, as a result the UV illumination wasn't absorbed from titania but was blocked via metallic NPs.

[viii]   Expansion of Limit of Detection in 4-MBA. An $AgTiO_2$ nanofilm which had a limit of detection 10^{-6}M, was able to detect 10^{-9}M of 4-MBA after Uv illumination of 90 minutes. Also, after 10minutes almost all the signal was lost due to V_O interaction with air.

Perspectives

In this section, we will discuss the final perspectives and potential advancements in this master thesis. Firstly, while it was proven that FSP is able to fabricate successfully nanofilms in one step development, it remains an open question how the particle formation process is developed. By using the glass substrate certain differences exist compared to the deposition on the glass-fiber filter. Subsequently, a more detailed screening experiments about deposition time, height above the burner and P/D (pump rate/ Dispersion rate) will provide us more details about the particle development.

Secondly, the scalability of FSP gives us the opportunity to fabricate nanofilms not only in glass substrates. One case is the use of FTO (Fluorine-doped Tin Oxide) as a substrate material. FTO possesses excellent electrical conductivity, transparency, and stability, making it an ideal candidate for applications in optoelectronics, solar cells, and sensors. By utilizing FTO as a substrate in conjunction with flame spray pyrolysis, we will demonstrate the feasibility of fabricating high-quality nanofilms, showcasing the potential for enhanced device performance and improved functionality.

Thirdly, the SERS effect could be explored in bigger depth. A "hot" research topic in SERS is detection of small quantities of hydrogen. Alternative energy resources are used more and more nowadays with H_2 to have the first place. As a result, detection of hydrogen in case of leaks is vital. Combining the FSP scaled up production with the portability of Raman measurements a new need for specific Nanosensors is important.

Finally, we didn't observe the expected enhancement in PIERS phenomena so certain changes are on the next steps. To begin with the addition of new UV lambs that can be adapted in the Raman set-up will reveal the full prospects of PIERS. Additionally, the size of TiO_2 could be altered inn order for UV illumination to be more effective.

Bibliography

(1) *Nanoplasmonics - Fundamentals and Applications*; Barbillon, G., Ed.; InTech, 2017. https://doi.org/10.5772/65150.

(2) Roduner, E. Size Matters: Why Nanomaterials Are Different. *Chem. Soc. Rev.* **2006**, *35* (7), 583. https://doi.org/10.1039/b502142c.

(3) Hornyak, G. L.; Tibbals, H. F.; Dutta, J.; Moore, J. J. *Introduction to Nanoscience and Nanotechnology*, 0 ed.; CRC Press, 2008. https://doi.org/10.1201/9781420047806.

(4) Stockman, M. I. Nanoplasmonics: Past, Present, and Glimpse into Future. *Opt. Express* **2011**, *19* (22), 22029. https://doi.org/10.1364/OE.19.022029.

(5) Brongersma, M. L.; Shalaev, V. M. The Case for Plasmonics. *Science* **2010**, *328* (5977), 440–441. https://doi.org/10.1126/science.1186905.

(6) Karlsson, R. SPR for Molecular Interaction Analysis: A Review of Emerging Application Areas. *J. Mol. Recognit.* **2004**, *17* (3), 151–161. https://doi.org/10.1002/jmr.660.

(7) *Handbook of Surface Plasmon Resonance*, 2nd edition.; Schasfoort, R. B. M., Ed.; Royal Society of Chemistry: London, 2017.

(8) Willets, K. A.; Van Duyne, R. P. Localized Surface Plasmon Resonance Spectroscopy and Sensing. *Annu. Rev. Phys. Chem.* **2007**, *58* (1), 267–297. https://doi.org/10.1146/annurev.physchem.58.032806.104607.

(9) Evanoff, D. D.; Chumanov, G. Synthesis and Optical Properties of Silver Nanoparticles and Arrays. *ChemPhysChem* **2005**, *6* (7), 1221–1231. https://doi.org/10.1002/cphc.200500113.

(10) Quinten, M. *Optical Properties of Nanoparticle Systems: Mie and Beyond*; 2011.

(11) Link, S.; Mohamed, M. B.; El-Sayed, M. A. Simulation of the Optical Absorption Spectra of Gold Nanorods as a Function of Their Aspect Ratio and the Effect of the Medium Dielectric Constant. *J. Phys. Chem. B* **1999**, *103* (16), 3073–3077. https://doi.org/10.1021/jp990183f.

(12) Jain, P. K.; Lee, K. S.; El-Sayed, I. H.; El-Sayed, M. A. Calculated Absorption and Scattering Properties of Gold Nanoparticles of Different Size, Shape, and Composition: Applications in Biological Imaging and Biomedicine. *J. Phys. Chem. B* **2006**, *110* (14), 7238–7248. https://doi.org/10.1021/jp057170o.

(13) Bastús, N. G.; Piella, J.; Puntes, V. Quantifying the Sensitivity of Multipolar (Dipolar, Quadrupolar, and Octapolar) Surface Plasmon Resonances in Silver Nanoparticles: The Effect of Size, Composition, and Surface Coating. *Langmuir* **2016**, *32* (1), 290–300. https://doi.org/10.1021/acs.langmuir.5b03859.

(14) Linic, S.; Christopher, P.; Ingram, D. B. Plasmonic-Metal Nanostructures for Efficient Conversion of Solar to Chemical Energy. *Nat. Mater.* **2011**, *10* (12), 911–921. https://doi.org/10.1038/nmat3151.

(15) Brongersma, M. L.; Halas, N. J.; Nordlander, P. Plasmon-Induced Hot Carrier Science and Technology. *Nat. Nanotechnol.* **2015**, *10* (1), 25–34. https://doi.org/10.1038/nnano.2014.311.

(16) Hartland, G. V.; Besteiro, L. V.; Johns, P.; Govorov, A. O. What's so Hot about Electrons in Metal Nanoparticles? *ACS Energy Lett.* **2017**, *2* (7), 1641–1653. https://doi.org/10.1021/acsenergylett.7b00333.

(17) Govorov, A. O.; Zhang, H.; Gun'ko, Y. K. Theory of Photoinjection of Hot Plasmonic Carriers from Metal Nanostructures into Semiconductors and Surface

Molecules. *J. Phys. Chem. C* **2013**, *117* (32), 16616–16631. https://doi.org/10.1021/jp405430m.

(18)   Govorov, A. O.; Zhang, H.; Demir, H. V.; Gun'ko, Y. K. Photogeneration of Hot Plasmonic Electrons with Metal Nanocrystals: Quantum Description and Potential Applications. *Nano Today* **2014**, *9* (1), 85–101. https://doi.org/10.1016/j.nantod.2014.02.006.

(19)   Li, X.; Xiao, D.; Zhang, Z. Landau Damping of Quantum Plasmons in Metal Nanostructures. *New J. Phys.* **2013**, *15* (2), 023011. https://doi.org/10.1088/1367-2630/15/2/023011.

(20)   Uskov, A. V.; Khurgin, J. B.; Smetanin, I. V.; Protsenko, I. E.; Nikonorov, N. V. Landau Damping in Hybrid Plasmonics. *J. Phys. Chem. Lett.* **2022**, *13* (4), 997–1001. https://doi.org/10.1021/acs.jpclett.1c04031.

(21)   Santiago, E. Y.; Besteiro, L. V.; Kong, X.-T.; Correa-Duarte, M. A.; Wang, Z.; Govorov, A. O. Efficiency of Hot-Electron Generation in Plasmonic Nanocrystals with Complex Shapes: Surface-Induced Scattering, Hot Spots, and Interband Transitions. *ACS Photonics* **2020**, *7* (10), 2807–2824. https://doi.org/10.1021/acsphotonics.0c01065.

(22)   Maurice, M. S.; Barros, N.; Kachkachi, H. Orientational Selectivity of Hot Electrons Generated by a Dimer of Plasmonic Nanoparticles. *J. Phys. Chem. C* **2021**, *125* (43), 23991–24000. https://doi.org/10.1021/acs.jpcc.1c04172.

(23)   Besteiro, L. V.; Kong, X.-T.; Wang, Z.; Hartland, G.; Govorov, A. O. Understanding Hot-Electron Generation and Plasmon Relaxation in Metal Nanocrystals: Quantum and Classical Mechanisms. *ACS Photonics* **2017**, *4* (11), 2759–2781. https://doi.org/10.1021/acsphotonics.7b00751.

(24)   Harutyunyan, H.; Martinson, A. B. F.; Rosenmann, D.; Khorashad, L. K.; Besteiro, L. V.; Govorov, A. O.; Wiederrecht, G. P. Anomalous Ultrafast Dynamics of Hot Plasmonic Electrons in Nanostructures with Hot Spots. *Nat. Nanotechnol.* **2015**, *10* (9), 770–774. https://doi.org/10.1038/nnano.2015.165.

(25)   Hong, Y.; Ku, M.; Lee, E.; Suh, J.-S.; Huh, Y.-M.; Yoon, D. S.; Yang, J. Localized Surface Plasmon Resonance Based Nanobiosensor for Biomarker Detection of Invasive Cancer Cells. *J. Biomed. Opt.* **2013**, *19* (5), 051202. https://doi.org/10.1117/1.JBO.19.5.051202.

(26)   Moskovits, M. Surface Roughness and the Enhanced Intensity of Raman Scattering by Molecules Adsorbed on Metals. *J. Chem. Phys.* **1978**, *69* (9), 4159–4161. https://doi.org/10.1063/1.437095.

(27)   Solís, D. M.; Taboada, J. M.; Obelleiro, F.; Liz-Marzán, L. M.; García De Abajo, F. J. Optimization of Nanoparticle-Based SERS Substrates through Large-Scale Realistic Simulations. *ACS Photonics* **2017**, *4* (2), 329–337. https://doi.org/10.1021/acsphotonics.6b00786.

(28)   Hirsch, L. R.; Stafford, R. J.; Bankson, J. A.; Sershen, S. R.; Rivera, B.; Price, R. E.; Hazle, J. D.; Halas, N. J.; West, J. L. Nanoshell-Mediated near-Infrared Thermal Therapy of Tumors under Magnetic Resonance Guidance. *Proc. Natl. Acad. Sci.* **2003**, *100* (23), 13549–13554. https://doi.org/10.1073/pnas.2232479100.

(29)   O'Neal, D. P.; Hirsch, L. R.; Halas, N. J.; Payne, J. D.; West, J. L. Photo-Thermal Tumor Ablation in Mice Using near Infrared-Absorbing Nanoparticles. *Cancer Lett.* **2004**, *209* (2), 171–176. https://doi.org/10.1016/j.canlet.2004.02.004.

(30)   Baffou, G.; Quidant, R.; García De Abajo, F. J. Nanoscale Control of Optical Heating in Complex Plasmonic Systems. *ACS Nano* **2010**, *4* (2), 709–716. https://doi.org/10.1021/nn901144d.

(31)   *Principles of Surface-Enhanced Raman Spectroscopy*; Elsevier, 2009. https://doi.org/10.1016/B978-0-444-52779-0.X0001-3.

(32)   Aroca, R. *Surface-Enhanced Vibrational Spectroscopy*, 1st ed.; Wiley, 2006. https://doi.org/10.1002/9780470035641.

(33)   Otto, A. Surface Enhanced Raman Scattering. *Vacuum* **1983**, *33* (10–12), 797–802. https://doi.org/10.1016/0042-207X(83)90613-9.

(34)   Han, X. X.; Rodriguez, R. S.; Haynes, C. L.; Ozaki, Y.; Zhao, B. Surface-Enhanced Raman Spectroscopy. *Nat. Rev. Methods Primer* **2022**, *1* (1), 87. https://doi.org/10.1038/s43586-021-00083-6.

(35)   Smith, W. E. Practical Understanding and Use of Surface Enhanced Raman Scattering/Surface Enhanced Resonance Raman Scattering in Chemical and Biological Analysis. *Chem. Soc. Rev.* **2008**, *37* (5), 955. https://doi.org/10.1039/b708841h.

(36)   Stiles, P. L.; Dieringer, J. A.; Shah, N. C.; Van Duyne, R. P. Surface-Enhanced Raman Spectroscopy. *Annu. Rev. Anal. Chem.* **2008**, *1* (1), 601–626. https://doi.org/10.1146/annurev.anchem.1.031207.112814.

(37)   Le Ru, E. C.; Etchegoin, P. G. *Principles of Surface-Enhanced Raman Spectroscopy and Related Plasmon Effects*, 1st ed.; Elsevier: Amsterdam, 2009.

(38)   Otto, A.; Mrozek, I.; Grabhorn, H.; Akemann, W. Surface-Enhanced Raman Scattering. *J. Phys. Condens. Matter* **1992**, *4* (5), 1143–1212. https://doi.org/10.1088/0953-8984/4/5/001.

(39)   Orendorff, C. J.; Gole, A.; Sau, T. K.; Murphy, C. J. Surface-Enhanced Raman Spectroscopy of Self-Assembled Monolayers: Sandwich Architecture and Nanoparticle Shape Dependence. *Anal. Chem.* **2005**, *77* (10), 3261–3266. https://doi.org/10.1021/ac048176x.

(40)   Kleinman, S. L.; Frontiera, R. R.; Henry, A.-I.; Dieringer, J. A.; Van Duyne, R. P. Creating, Characterizing, and Controlling Chemistry with SERS Hot Spots. *Phys Chem Chem Phys* **2013**, *15* (1), 21–36. https://doi.org/10.1039/C2CP42598J.

(41)   Otto, A. The 'Chemical' (Electronic) Contribution to Surface-Enhanced Raman Scattering. *J. Raman Spectrosc.* **2005**, *36* (6–7), 497–509. https://doi.org/10.1002/jrs.1355.

(42)   *Surface Enhanced Raman Spectroscopy: Analytical, Biophysical and Life Science Applications*; Schlücker, S., Ed.; Wiley-VCH Verlag: Weinheim, Germany, 2011.

(43)   Cong, S.; Liu, X.; Jiang, Y.; Zhang, W.; Zhao, Z. Surface Enhanced Raman Scattering Revealed by Interfacial Charge-Transfer Transitions. *The Innovation* **2020**, *1* (3), 100051. https://doi.org/10.1016/j.xinn.2020.100051.

(44)   Yang, B.; Chen, G.; Ghafoor, A.; Zhang, Y.; Zhang, X.; Li, H.; Dong, X.; Wang, R.; Zhang, Y.; Zhang, Y.; Dong, Z. Chemical Enhancement and Quenching in Single-Molecule Tip-Enhanced Raman Spectroscopy. *Angew. Chem. Int. Ed.* **2023**, *62* (13). https://doi.org/10.1002/anie.202218799.

(45)   Li, H.; Merkl, P.; Sommertune, J.; Thersleff, T.; Sotiriou, G. A. SERS Hotspot Engineering by Aerosol Self-Assembly of Plasmonic Ag Nanoaggregates with Tunable Interparticle Distance. *Adv. Sci.* **2022**, *9* (22), 2201133. https://doi.org/10.1002/advs.202201133.

(46)   Kim, J.; Jang, Y.; Kim, N.-J.; Kim, H.; Yi, G.-C.; Shin, Y.; Kim, M. H.; Yoon, S. Study of Chemical Enhancement Mechanism in Non-Plasmonic Surface Enhanced Raman Spectroscopy (SERS). *Front. Chem.* **2019**, *7*, 582. https://doi.org/10.3389/fchem.2019.00582.

(47)   Pieczonka, N. P. W.; Aroca, R. F. Single Molecule Analysis by Surfaced-Enhanced Raman Scattering. *Chem. Soc. Rev.* **2008**, *37* (5), 946. https://doi.org/10.1039/b709739p.

(48)   Setnikar, G.; Samson, J.; Méasson, M.-A. Raman Selection Rules Calculator: A Simplified Selection Rules Calculator for Raman Spectroscopy Experiment. *SoftwareX* **2022**, *19*, 101152. https://doi.org/10.1016/j.softx.2022.101152.

(49)   Hoang, L. T.; Pham, H. V.; Nguyen, M. T. T. Investigation of the Factors Influencing the Surface-Enhanced Raman Scattering Activity of Silver Nanoparticles. *J. Electron. Mater.* **2020**, *49* (3), 1864–1871. https://doi.org/10.1007/s11664-019-07870-8.

(50)   Ben-Jaber, S.; Peveler, W. J.; Quesada-Cabrera, R.; Cortés, E.; Sotelo-Vazquez, C.; Abdul-Karim, N.; Maier, S. A.; Parkin, I. P. Photo-Induced Enhanced Raman Spectroscopy for Universal Ultra-Trace Detection of Explosives, Pollutants and Biomolecules. *Nat. Commun.* **2016**, *7* (1), 12189. https://doi.org/10.1038/ncomms12189.

(51)   Zhang, M.; Sun, H.; Chen, X.; Yang, J.; Shi, L.; Chen, T.; Bao, Z.; Liu, J.; Wu, Y. Highly Efficient Photoinduced Enhanced Raman Spectroscopy (PIERS) from Plasmonic Nanoparticles Decorated 3D Semiconductor Arrays for Ultrasensitive, Portable, and Recyclable Detection of Organic Pollutants. *ACS Sens.* **2019**, *4* (6), 1670–1681. https://doi.org/10.1021/acssensors.9b00562.

(52)   Glass, D.; Cortés, E.; Ben-Jaber, S.; Brick, T.; Peveler, W. J.; Blackman, C. S.; Howle, C. R.; Quesada-Cabrera, R.; Parkin, I. P.; Maier, S. A. Dynamics of Photo-Induced Surface Oxygen Vacancies in Metal-Oxide Semiconductors Studied Under Ambient Conditions. *Adv. Sci.* **2019**, *6* (22), 1901841. https://doi.org/10.1002/advs.201901841.

(53)   Glass, D.; Cortés, E.; Ben-Jaber, S.; Brick, T.; Quesada-Cabrera, R.; Peveler, W. J.; Zhu, Y.; Blackman, C. S.; Howle, C. R.; Parkin, I. P.; Maier, S. A. Photo-Induced Enhanced Raman Spectroscopy (PIERS): Sensing Atomic-Defects, Explosives and Biomolecules. In *Chemical, Biological, Radiological, Nuclear, and Explosives (CBRNE) Sensing XX*; Guicheteau, J. A., Howle, C. R., Eds.; SPIE: Baltimore, United States, 2019; p 13. https://doi.org/10.1117/12.2518948.

(54)   Glass, D.; Cortés, E.; Peveler, W. J.; Howle, C. R.; Quesada-Cabrera, R.; Parkin, I. P.; Maier, S. A. Enhancing Hybrid Metal-Semiconductor Systems beyond SERS with PIERS (Photo-Induced Enhanced Raman Scattering) for Trace Analyte Detection. In *Chemical, Biological, Radiological, Nuclear, and Explosives (CBRNE) Sensing XXI*; Guicheteau, J. A., Howle, C. R., Eds.; SPIE: Online Only, United States, 2020; p 2. https://doi.org/10.1117/12.2557517.

(55)   Almohammed, S.; Zhang, F.; Rodriguez, B. J.; Rice, J. H. Photo-Induced Surface-Enhanced Raman Spectroscopy from a Diphenylalanine Peptide Nanotube-Metal Nanoparticle Template. *Sci. Rep.* **2018**, *8* (1), 3880. https://doi.org/10.1038/s41598-018-22269-x.

(56)   Ke, Z.-Y.; Tsai, C.-J.; Liao, P.-H.; Kong, K. V. Photoinduced Enhanced Raman Probe for Use in Highly Specific and Sensitive Imaging for Tyrosine Dimerization in Inflammatory Cells. *J. Phys. Chem. Lett.* **2020**, *11* (17), 7443–7448. https://doi.org/10.1021/acs.jpclett.0c01938.

(57)   Rahimi, N.; Pax, R. A.; Gray, E. MacA. Review of Functional Titanium Oxides. I: TiO2 and Its Modifications. *Prog. Solid State Chem.* **2016**, *44* (3), 86–105. https://doi.org/10.1016/j.progsolidstchem.2016.07.002.

(58)   Vo-Dinh, T. SERS Chemical Sensors and Biosensors: New Tools for Environmental and Biological Analysis. *Sens. Actuators B Chem.* **1995**, *29* (1–3), 183–189. https://doi.org/10.1016/0925-4005(95)01681-3.

(59)   Liang, X.; Li, N.; Zhang, R.; Yin, P.; Zhang, C.; Yang, N.; Liang, K.; Kong, B. Carbon-Based SERS Biosensor: From Substrate Design to Sensing and Bioapplication. *NPG Asia Mater.* **2021**, *13* (1), 8. https://doi.org/10.1038/s41427-020-00278-5.

(60)   Kruss, S.; Hilmer, A. J.; Zhang, J.; Reuel, N. F.; Mu, B.; Strano, M. S. Carbon Nanotubes as Optical Biomedical Sensors. *Adv. Drug Deliv. Rev.* **2013**, *65* (15), 1933–1950. https://doi.org/10.1016/j.addr.2013.07.015.

(61)   Koh, E. H.; Lee, W.-C.; Choi, Y.-J.; Moon, J.-I.; Jang, J.; Park, S.-G.; Choo, J.; Kim, D.-H.; Jung, H. S. A Wearable Surface-Enhanced Raman Scattering Sensor for Label-Free Molecular Detection. *ACS Appl. Mater. Interfaces* **2021**, *13* (2), 3024–3032. https://doi.org/10.1021/acsami.0c18892.

(62)   Nocerino, V.; Miranda, B.; Tramontano, C.; Chianese, G.; Dardano, P.; Rea, I.; De Stefano, L. Plasmonic Nanosensors: Design, Fabrication, and Applications in Biomedicine. *Chemosensors* **2022**, *10* (5), 150. https://doi.org/10.3390/chemosensors10050150.

(63)   Strobel, R.; Pratsinis, S. E. Flame Aerosol Synthesis of Smart Nanostructured Materials. *J. Mater. Chem.* **2007**, *17* (45), 4743. https://doi.org/10.1039/b711652g.

(64)   Ensor, D. *Aerosol Science and Technology: History and Reviews. Technical Report, RTI Press, Research Triangle Park, NC*; 2011.

(65)   Ulrich, G. D. Flame Synthesis of Fine Particles. Chem. Eng. News, 1984, 62, 22.

(66)   Busca, G. *Heterogeneous Catalytic Materials: Solid State Chemistry, Surface Chemistry and Catalytic Behaviour*, 1. ed.; Elsevier: Amsterdam Heidelberg, 2014.

(67)   Sotiriou, G. A.; Sannomiya, T.; Teleki, A.; Krumeich, F.; Vörös, J.; Pratsinis, S. E. Non-Toxic Dry-Coated Nanosilver for Plasmonic Biosensors. *Adv. Funct. Mater.* **2010**, *20* (24), 4250–4257. https://doi.org/10.1002/adfm.201000985.

(68)   Lee, H.; Kim, T. J.; Li, C.; Choi, I. D.; Kim, Y. T.; Coker, Z.; Choi, T.-Y.; Lee, D. Flame Aerosol Synthesis of Carbon-Supported Pt–Ru Catalysts for a Fuel Cell Electrode. *Int. J. Hydrog. Energy* **2014**, *39* (26), 14416–14420. https://doi.org/10.1016/j.ijhydene.2014.02.080.

(69)   Yoon, Y.; Im, J.; You, H.; Shin, D. Fabrication of NiO/YSZ Anode for Solid Oxide Fuel Cells by Aerosol Flame Deposition. *J. Eur. Ceram. Soc.* **2007**, *27* (13–15), 4257–4260. https://doi.org/10.1016/j.jeurceramsoc.2007.02.139.

(70)   Singh, P.; Pandit, S.; Mokkapati, V. R. S. S.; Garg, A.; Ravikumar, V.; Mijakovic, I. Gold Nanoparticles in Diagnostics and Therapeutics for Human Cancer. *Int. J. Mol. Sci.* **2018**, *19* (7), 1979. https://doi.org/10.3390/ijms19071979.

(71)   Starsich, F. H. L.; Herrmann, I. K.; Pratsinis, S. E. Nanoparticles for Biomedicine: Coagulation During Synthesis and Applications. *Annu. Rev. Chem. Biomol. Eng.* **2019**, *10* (1), 155–174. https://doi.org/10.1146/annurev-chembioeng-060718-030203.

(72)   *Handbook of Atomization and Sprays: Theory and Applications*; Ashgriz, N., Ed.; Springer: New York Heidelberg, 2011.

(73)   Koirala, R.; Pratsinis, S. E.; Baiker, A. Synthesis of Catalytic Materials in Flames: Opportunities and Challenges. *Chem. Soc. Rev.* **2016**, *45* (11), 3053–3068. https://doi.org/10.1039/C5CS00011D.

(74)   Jossen, R.; Pratsinis, S. E.; Stark, W. J.; Madler, L. Criteria for Flame-Spray Synthesis of Hollow, Shell-Like, or Inhomogeneous Oxides. *J. Am. Ceram. Soc.* **2005**, *88* (6), 1388–1393. https://doi.org/10.1111/j.1551-2916.2005.00249.x.

(75)   Mädler, L.; Kammler, H. K.; Mueller, R.; Pratsinis, S. E. Controlled Synthesis of Nanostructured Particles by Flame Spray Pyrolysis. *J. Aerosol Sci.* **2002**, *33* (2), 369–389. https://doi.org/10.1016/S0021-8502(01)00159-8.

(76)   Teoh, W. Y.; Amal, R.; Mädler, L. Flame Spray Pyrolysis: An Enabling Technology for Nanoparticles Design and Fabrication. *Nanoscale* **2010**, *2* (8), 1324. https://doi.org/10.1039/c0nr00017e.

(77)   Tricoli, A.; Nasiri, N.; Chen, H.; Wallerand, A. S.; Righettoni, M. Ultra-Rapid Synthesis of Highly Porous and Robust Hierarchical ZnO Films for Dye Sensitized Solar Cells. *Sol. Energy* **2016**, *136*, 553–559. https://doi.org/10.1016/j.solener.2016.07.024.

(78)   Tricoli, A.; Righettoni, M.; Teleki, A. Semiconductor Gas Sensors: Dry Synthesis and Application. *Angew. Chem. Int. Ed.* **2010**, *49* (42), 7632–7659. https://doi.org/10.1002/anie.200903801.

(79)   Nasiri, N.; Bo, R.; Wang, F.; Fu, L.; Tricoli, A. Ultraporous Electron-Depleted ZnO Nanoparticle Networks for Highly Sensitive Portable Visible-Blind UV Photodetectors. *Adv. Mater.* **2015**, *27* (29), 4336–4343. https://doi.org/10.1002/adma.201501517.

(80)   Tricoli, A.; Elmøe, T. D. Flame Spray Pyrolysis Synthesis and Aerosol Deposition of Nanoparticle Films. *AIChE J.* **2012**, *58* (11), 3578–3588. https://doi.org/10.1002/aic.13739.

(81)   Tricoli, A.; Righettoni, M.; Teleki, A. Semiconductor Gas Sensors: Dry Synthesis and Application. *Angew. Chem. Int. Ed.* **2010**, *49* (42), 7632–7659. https://doi.org/10.1002/anie.200903801.

(82)   Kühne, S.; Graf, M.; Tricoli, A.; Mayer, F.; Pratsinis, S. E.; Hierlemann, A. Wafer-Level Flame-Spray-Pyrolysis Deposition of Gas-Sensitive Layers on Microsensors. *J. Micromechanics Microengineering* **2008**, *18* (3), 035040. https://doi.org/10.1088/0960-1317/18/3/035040.

(83)   Chen, H.; Mulmudi, H. K.; Tricoli, A. Flame Spray Pyrolysis for the One-Step Fabrication of Transition Metal Oxide Films: Recent Progress in Electrochemical and Photoelectrochemical Water Splitting. *Chin. Chem. Lett.* **2020**, *31* (3), 601–604. https://doi.org/10.1016/j.cclet.2019.05.016.

(84)   Tricoli, A.; Graf, M.; Mayer, F.; Kuühne, S.; Hierlemann, A.; Pratsinis, S. E. Micropatterning Layers by Flame Aerosol Deposition-Annealing. *Adv. Mater.* **2008**, *20* (16), 3005–3010. https://doi.org/10.1002/adma.200701844.

(85)   Raman, C. V.; Krishnan, K. S. A New Type of Secondary Radiation. *Nature* **1928**, *121* (3048), 501–502. https://doi.org/10.1038/121501c0.

(86)   Barańska, H.; Łabudzińska, A.; Terpiński, J. *Laser Raman Spectrometry: Analytical Applications*; Ellis Horwood series in analytical chemistry; PWN--Polish Scientific Publishers ; E. Horwood ; Distributors, Halsted Press: Warszawa : Chichester : New York, N.Y., U.S.A, 1987.

(87)   Colomban, P.; Gouadec, G. Raman Scattering Theory and Elements of Raman Instrumentation. In *Raman Spectroscopy for Soft Matter Applications*; Amer, M. S., Ed.; John Wiley & Sons, Inc.: Hoboken, NJ, USA, 2008; pp 11–29. https://doi.org/10.1002/9780470475997.ch2.

(88)   Goulet, P. J. G.; Aroca, R. F. Distinguishing Individual Vibrational Fingerprints: Single-Molecule Surface-Enhanced Resonance Raman Scattering

from One-to-One Binary Mixtures in Langmuir−Blodgett Monolayers. *Anal. Chem.* **2007**, *79* (7), 2728–2734. https://doi.org/10.1021/ac062059f.

(89) Luck, W. A. P. D. J. Gardiner, P. R. Graves (Eds.): Practical Raman Spectroscopy, Mit Beiträgen von H. J. Bowley, D. J. Gardiner, D. L. Gerrard, P. R. Graves, J. D. Louden, and G. Turrell, Springer-Verlag, Berlin, Heidelberg, New York 1989. 157 Seiten, Brosch., Preis: D. *Berichte Bunsenges. Für Phys. Chem.* **1990**, *94* (9), 1047–1047. https://doi.org/10.1002/bbpc.19900940938.

(90) Smith, E.; Dent, G. *Modern Raman Spectroscopy – A Practical Approach*, 1st ed.; Wiley, 2004. https://doi.org/10.1002/0470011831.

(91) Liang, L.; Zhao, X.; Wen, J.; Liu, J.; Zhang, F.; Guo, X.; Zhang, K.; Wang, A.; Gao, R.; Wang, Y.; Zhang, Y. Flexible SERS Substrate with a Ag–SiO$_2$ Cosputtered Film for the Rapid and Convenient Detection of Thiram. *Langmuir* **2022**, *38* (45), 13753–13762. https://doi.org/10.1021/acs.langmuir.2c01853.

(92) Bunaciu, A. A.; Udriştioiu, E. G.; Aboul-Enein, H. Y. X-Ray Diffraction: Instrumentation and Applications. *Crit. Rev. Anal. Chem.* **2015**, *45* (4), 289–299. https://doi.org/10.1080/10408347.2014.949616.

(93) Yadav, L. D. S. Ultraviolet (UV) and Visible Spectroscopy. In *Organic Spectroscopy*; Springer Netherlands: Dordrecht, 2005; pp 7–51. https://doi.org/10.1007/978-1-4020-2575-4_2.

(94) Swinehart, D. F. The Beer-Lambert Law. *J. Chem. Educ.* **1962**, *39* (7), 333. https://doi.org/10.1021/ed039p333.

(95) Fragou, F.; Stathi, P.; Deligiannakis, Y.; Louloudi, M. Safe-by-Design Flame Spray Pyrolysis of SiO$_2$ Nanostructures for Minimizing Acute Toxicity. *ACS Appl. Nano Mater.* **2022**, *5* (6), 8184–8195. https://doi.org/10.1021/acsanm.2c01273.

(96) Fujiwara, K.; Deligiannakis, Y.; Skoutelis, C. G.; Pratsinis, S. E. Visible-Light Active Black TiO2-Ag/TiOx Particles. *Appl. Catal. B Environ.* **2014**, *154–155*, 9–15. https://doi.org/10.1016/j.apcatb.2014.01.060.

(97) Ben Yahia, M.; Lemoigno, F.; Beuvier, T.; Filhol, J.-S.; Richard-Plouet, M.; Brohan, L.; Doublet, M.-L. Updated References for the Structural, Electronic, and Vibrational Properties of TiO2(B) Bulk Using First-Principles Density Functional Theory Calculations. *J. Chem. Phys.* **2009**, *130* (20), 204501. https://doi.org/10.1063/1.3130674.

(98) Voepel, P.; Weiss, M.; Smarsly, B. M.; Marschall, R. Photocatalytic Activity of Multiphase TiO2(B)/Anatase Nanoparticle Heterojunctions Prepared from Ionic Liquids. *J. Photochem. Photobiol. Chem.* **2018**, *366*, 34–40. https://doi.org/10.1016/j.jphotochem.2018.03.019.

(99) Li, R.; Lv, H.; Zhang, X.; Liu, P.; Chen, L.; Cheng, J.; Zhao, B. Vibrational Spectroscopy and Density Functional Theory Study of 4-Mercaptobenzoic Acid. *Spectrochim. Acta. A. Mol. Biomol. Spectrosc.* **2015**, *148*, 369–374. https://doi.org/10.1016/j.saa.2015.03.132.

(100) Zhong, F.; Wu, Z.; Guo, J.; Jia, D. Porous Silicon Photonic Crystals Coated with Ag Nanoparticles as Efficient Substrates for Detecting Trace Explosives Using SERS. *Nanomaterials* **2018**, *8* (11), 872. https://doi.org/10.3390/nano8110872.

(101) Capocefalo, A.; Mammucari, D.; Brasili, F.; Fasolato, C.; Bordi, F.; Postorino, P.; Domenici, F. Exploring the Potentiality of a SERS-Active PH Nano-Biosensor. *Front. Chem.* **2019**, *7*, 413. https://doi.org/10.3389/fchem.2019.00413.

(102) Fasolato, C.; Domenici, F.; Sennato, S.; Mura, F.; De Angelis, L.; Luongo, F.; Costantini, F.; Bordi, F.; Postorino, P. Dimensional Scale Effects on Surface Enhanced Raman Scattering Efficiency of Self-Assembled Silver Nanoparticle

Clusters. *Appl. Phys. Lett.* **2014**, *105* (7), 073105. https://doi.org/10.1063/1.4893373.

(103)   Mhlanga, N.; Ntho, T. A. A Theoretical Study of 4-Mercaptobenzoic Acid Assembled on Ag for Surface-Enhanced Raman Scattering Applications. *Mater. Today Commun.* **2021**, *26*, 101698. https://doi.org/10.1016/j.mtcomm.2020.101698.

(104)   Silva De Almeida, F.; Bussler, L.; Marcio Lima, S.; Fiorucci, A. R.; Da Cunha Andrade, L. H. High Surface-Enhanced Raman Scattering (SERS) Amplification Factor Obtained with Silver Printed Circuit Boards and the Influence of Phenolic Resins for the Characterization of the Pesticide Thiram. *Appl. Spectrosc.* **2016**, *70* (7), 1157–1164. https://doi.org/10.1177/0003702816652356.

(105)   Ye, J.; Arul, R.; Nieuwoudt, M. K.; Dong, J.; Zhang, T.; Dai, L.; Greenham, N. C.; Rao, A.; Hoye, R. L. Z.; Gao, W.; Simpson, M. C. Understanding the Chemical Mechanism behind Photoinduced Enhanced Raman Spectroscopy. *J. Phys. Chem. Lett.* **2023**, *14* (19), 4607–4616. https://doi.org/10.1021/acs.jpclett.3c00478.